Friction and Elastohydrodynamic Measurements using Atomic Force Microscope

Muhammad Arshad

To cite this version:

Muhammad Arshad. Friction and Elastohydrodynamic Measurements using Atomic Force Microscope. Physics [physics]. Université de Bordeaux, 2021. English. NNT : 2021BORD0244 . tel-03525315

HAL Id: tel-03525315
https://theses.hal.science/tel-03525315

Submitted on 13 Jan 2022

THÈSE PRÉSENTÉE

POUR OBTENIR LE GRADE DE

DOCTEUR DE L'UNIVERSITÉ DE BORDEAUX

ÉCOLE DOCTORALE DES SCIENCES PHYSIQUES ET DE L'INGÉNIEUR
SPÉCIALITÉ : LASERS, MATIÈRE ET NANOSCIENCES

par Muhammad Arshad

Friction and Elastohydrodynamic Measurements using Atomic Force Microscope

Sous la direction de : Abdelhamid Maali

Soutenue le 26/10/2021

Membres du jury:

Mme. Elise LORENCEAU	Directeur de recherche, Université Grenoble , Rapporteur
M. Pascal PANIZZA	Professeur, Université Rennes, Rapporteur
Mme Elisabeth LEMAIRE	Directeur de recherche, Université Cote d'Azur, Examinateur
M. Hamid KELLAY	Professeur, Université de Bordeaux, Examinateur
M. Abdelhamid MAALI	Directeur de recherche, Université de Bordeaux, Directeur de thèse

Acknowledgement

The successful completion of this thesis required lot of guidance and support from many people and I am privileged to have them around me.

First and formost, I wish to express my sincere gratitude to my adviser Dr. Abdelhamid Maali, for his constant guidance, encouragement, inspiration and intense supervision during my PhD studies. It was an immense pleasure to work under his supervision. His reliable and fast responses to any of my problems and his availability in the case of difficulties greatly facilitated my course through this audacious task. Thank you Sir.

I would like to thank the members of the jury for accepting and evaluating my thesis. The members of the jury including Mme. Elise Lorenceau and M. Pascal Panizza make the report for my manuscript, while Mme. Elisabeth Lemaire and M. Hamid Kellay examine the defense.

I would like to thank Dr. Thomas Salez, Prof. Elie Raphael, Prof Elisabeth Lemaire and Prof. Eric Drokenmuller. I got much support and inspiration from them during all projects. I learnt a lot during those collaborations and discussions.

I would like to thank Fabio Pistolesi, Sophie Grandet and Josiane Parzych for their help and administrative support in LOMA. I would like to thank Fabien Morote for providing experimental materials and help to perform atomic force microscope imaging. I would thank the staffs of informatics service for their help to resolve the problems related to computer. The Electronic service and Mechanical service helped and provided electronic devices and experimental pieces, respectively.

I would like to thank my colleagues and friends Zaicheng Zhang, Vincent Bertin, Yoanh Moratille, Muhammad Ghawas for their help during the course of my PhD work. I would especially thank to Zaicheng for initial support in basic learnings of atomic force microscope and experimental prodedures. The life outside LOMA would have been boring and tough without friends Ashique Hussain, Shujaat Ali, Lutfurehman, Saeed Khan, Dr Ghulam Murtaza and Hasaan. Thank you all.

I am indebt to the unconditional support and trust of my parents and wife. I would thank my children for understanding the reason of my absence during this time. My wife dedicated all her time and energy to take care of our children and i really appreciate it.

Lastly, I would like to extend my gratitude to Higher Education Commission of Pakistan for the financial support. I really appreciate their understanding of situation related to pandemic and extension of my scholarship. In all, this task would not be materialized without their support.

Contents

General Introduction 1

1 Instruments and Techniques used in this Thesis 5
- 1.1 Atomic Force Microscope . . . 5
  - 1.1.1 Operating Modes of an AFM . . . 7
  - 1.1.2 Force Distance curve . . . 8
- 1.2 Experimental Techniques and Instruments . . . 9
  - 1.2.1 Colloidal Probes . . . 9
  - 1.2.2 Roughness Measurement . . . 12
  - 1.2.3 Piezoelectric Actuator . . . 13
  - 1.2.4 Lock in Amplifier . . . 16
- 1.3 The characteristics of the probes . . . 18
- 1.4 Conclusion . . . 20

2 Calibrations 21
- 2.1 Introduction . . . 21
- 2.2 Normal Spring Constant Calibration . . . 22
  - 2.2.1 Geometry of Cantilever . . . 22
  - 2.2.2 Added Mass Method . . . 26
  - 2.2.3 Normal Sader Method . . . 27
  - 2.2.4 Thermal Noise Method . . . 28
  - 2.2.5 Hydrodynamic Drag Method . . . 31
- 2.3 Lateral Force Calibration . . . 36
  - 2.3.1 Geometry of Cantilever . . . 36
  - 2.3.2 Torsional Sader Method . . . 37
  - 2.3.3 Torsional Cleveland Method . . . 38
  - 2.3.4 Thermal Noise Method . . . 38
  - 2.3.5 Hydrodynamic Drag Method . . . 39
- 2.4 Conclusion . . . 43

3 Viscoelastic Properties of PDMS **44**
3.1 Introduction 44
3.2 Experimental Details 45
  3.2.1 PDMS sample preparation 45
  3.2.2 Dynamic AFM Method 46
3.3 Analytical Solution for Viscoelastic Response: A Simple Model 52
3.4 Hydrodynamic Model for Viscoelastic Response 54
3.5 Contact Mechanics 59
3.6 Conclusion and Perspective 60

4 Friction between Polystyrene Microspheres **62**
4.1 Introduction 62
4.2 Mono Asperity Contact Model 64
4.3 Materials and Method 67
4.4 Experimental Measurements 69
  4.4.1 Roughness Characterization of Polystyrene Microspheres 69
  4.4.2 Static Friction Measurement 70
  4.4.3 Dynamic Friction Measurement 73
  4.4.4 Viscosity Measurement of Suspension 79
4.5 Conclusion and Perspective 82

General Conclusion **84**

General Introduction

The studies of fluid flow at the nanoscale has shown significant rise due to its potential applicability in different field of studies including soft matter, medical science, mechanics and engineering. At nanometric length scales, the solid-liquid interaction at the interface is one of the dominant factor, which governs the fluid behaviors [1,2]. These behaviours are evident in the science of interfaces and mechanics where the continuum concept of mechanics break down at the nanoscale [3] and the granularity of the matter at the molecular size becomes important [4–6]. Many of the macroscale mechanical phenomena, such as, lubricated friction, take their origin at the nanoscale and thus they can best be explained by the experiments at those scales. This quest has led to the use of experimental tools such as Surface Force Apparatus (SFA) and Atomic Force Microscope (AFM) that allow measurements at nanometric length scale.

In this work, we have used the colloidal AFM in dynamic mode to study the rheological properties of thin soft polymeric film and the friction between polystyrene microspheres at the nanoscale. Ducker and Butt [7] had developed the colloidal probe technique back in 1991 where a probe of known geometry is attached to the tip of an AFM cantilever. This technique allows to measure the interaction force between the two colloidal particles or between the colloidal particle and a plane substrate. For each specific application, the geometry of the probe is chosen to optimise the spatial resolution and the force sensitivity. In addition to the flexibility in the choice of the material and the geometry of the probe, the well-defined geometry of the probe provides an easier and accurate interpretation of data in term of the theoretical model [8,9].

Mechanical characterization of soft surfaces

For the successful development and wide use of nano-devices, an accurate and well-understood mechanical characterization of the materials at nanoscale is prerequisite [10]. The characterization techniques such as nanoindentation, optical tweezers and AFM-based methods are used to investigate the mechanical properties of materials. The knowledge of nano-mechanical traits has been utilized to develop new materials and structures. For instance, study of the mechanics of cells and tissues has led to the development of the biomimetic materials, structures for the tissue engineering and artificial implantation [11,12].

Among the characterization techniques, AFM is one of an effective and reliable tool, which can be used to characterize the chemical [13], electrical [14, 15] and mechanical [10, 12, 16–18] properties of the materials with nanometric resolution. In standard operation, an AFM tip, which acts as an indenter, is used to probe mechanical properties of the sample surface. The interaction of the probe and sample is recorded to extract the mechanical traits such as hardness, viscoelasticity etc. However, there are limitations in indentation experiment for soft materials due to the vulnerability, fragility and contribution of the surface energy [18]. Non-contact measuring technique in a liquid was developed with SFA where the contactless interaction allows to measure the surface elasticity [19–21]. However, in SFA the choice of sample thickness and frequency range due to the macroscopic size of the probe are a few of constraint in the wide use of the technique. On the other hand, in an AFM smaller probes are used and it allows working in the large frequency range.

In contactless technique using an AFM, the mechanical properties of the soft sample are studied by measuring the nano-hydrodynamic interaction between a probing oscillating sphere and the substrate in liquid environment [22, 23]. The fluid flow in micro-confinement along with the soft surfaces induces the elastohydrodynamic (EHD) coupling [24]. This scenario is very common in biological systems [25] and the tribology of lubricated contacts [26]. In the former case, the flow of red blood cells in veins and arteries, lubrication of the eye in ocular cavity and synovial joints are a few example of EHD coupling. During the lubricated contact, the friction, wears and tears are significantly reduced due to deformation under the influence of the viscous force of the fluid. The EHD force during the lubricated contact generates the lift force in the approaching surfaces. The induced lift force is highlighted in many research woks, including the rolling cylinder near a soft wall [27], sphere near a soft wall [28] and a colloidal probe in proximity to the PDMS substrates [29]. In short, the drainage of fluid at the confined gap generate hydrodynamic stress to induce the deformation of the soft surface and based on this coupling, the mechanical traits of the soft interfaces are extracted without solid-solid contact.

Using an AFM, the technique based on the vibrating probe offer an additional advantage to study the mechanical properties at different vibration frequencies. Usually, the frequency dependent rheology of soft solids are probed at macroscale with conventional shear rheometers where the sample is fixed between the two rotating parallel plates [30–32]. Imposing a rotating displacement on one plate and measurement of the applied torque on the other one, allows to extract the mechanical traits such as, the complex shear modulus of the system. This method requires a perfect contact between the sample and the plates of the rheometer. The dynamic colloidal AFM method is a good candidate to probe the EHD interaction at nanoscale for different vibration frequencies without such constraint. It allows working in large frequency range from $20Hz$ up to few kHz, depending on the resonance frequency of the cantilever [33–35].

Friction at nanoscale

Friction may be one of the physical phenomena that is ubiquitous in nature but still less understood. It is the science of interacting surfaces in relative motion. Leonardo D. Vinci recorded first systematic study of the friction, but Amonton is highly accredited due to formulation of the friction laws. With development and advancement of tools and technology, the access to the nanometric length scale has revealed that the smooth looking surfaces are rough at smaller scale and the real contact between two solids is a fraction of the apparent contact [36, 37]. Based on these facts, it was proposed that the contact between two surfaces occurs at some microscopic points, which are named as asperities in the literature. Hence, Friction between two sliding surfaces is the outcome of interdependent mechanical behaviors of asperities, which are regularly being formed, deformed and ruptured [38].

The study of nanotribology aims to characterize, understand and control the friction, wears and adhesion in a system. It is primarily accomplished by performing the lateral force measurement in an AFM-based characterization technique, where the torque produced in the cantilever is monitored during the contact-mode scanning perpendicular to the long-axis of the cantilever [39]. Mate *et al.* [40] has credit of introducing the technique for the first time in the experimental field. They built a scanning force microscope and studied lateral deflection of tungsten wire through optical interferometry. In AFM-based friction measurements, the interaction between the cantilever tip and the sample surface enlarge imitates the interaction of the asperities. The classical contact problems are commonly interpreted using famous Hertz contact model where the stress-strain relation between the elastic curved bodies is described with-in elastic limit [41], but, the mono-asperity contact model is largely used to describe the contact between the asperities [42, 43].

Several studies have highlighted the role of nanoscale repulsive and the frictional forces in the suspensions. The rheology of solid particles suspensions strongly depends on the nature of interaction between the particles. It was not much before when the hydrodynamic interaction between the solid particles was assumed to be the dominant factor in the rheology of suspensions. However, recent findings have revealed the pivotal role of the frictional contact between the solid particles in the rheology of the suspensions [44–49]. Several rheological phenomena, such as shear-thinning, shear-thickening, anisotropic normal stress, are exhibited by the suspension depending on the concentration and the applied shear rate. For instance, shear-thinning phenomenon is a typical non-Newtonian behavior of suspensions, which is attributed to the interparticle and the fluid-particle interaction [49]. The discontinuous shear-thickening in highly concentrated non-Brownian suspension is another important phenomenon, which is also explained by the frictional contact between the particles [47, 50, 51].

In all, the dominant role of frictional contact in the rheology of the suspensions indicates a close link between the microscopic (friction) and macroscopic (viscosity) phenomena. Using an AFM, the interaction between the colloidal probe and the microsphere provides direct insight to the microscopic origin of friction, whereas, the rheometer is a better alternative for the macroscopic studies of the suspension. The viscosity of suspension can be measured in rotating parallel plate geometry by imposing the stress steps whose duration varies depending upon the intensity of the stress. To summarize the fact that the correlation between the viscosity of the suspension and the friction may allows to predict the rheology of moderately concentrated suspension from the microscopic contact law [52].

For the friction studies, we were part of a multidisciplinary collaborating project. The project partners include: polymer chemistry team of Eric Drokenmuller in IMP (Lyon University) who was responsible for synthesis of functional microparticles with controlled diameter, stiffness and surface properties; the numerical rheology team of François Peters in InPhyNi (Nice Sophia-Antipolis University) who had worked on the numerical simulation of the microscopic contact laws; the experimental rheology team of Elisabeth Lemaire in InPhyNi (Nice Sophia-Antipolis University) had performed the rheological experiments for validation of the numerical results; and finally, we were responsible for the roughness characterization and friction measurement between the contacting microspheres.

The manuscript is organized as follows:

- In chapter 1 we will present the tools and techniques used during this experimental work. We will introduce the experimental setup and the process in the preparation of the colloidal probe. A brief discussion will also cover the working principle of the piezoelectric actuation stage and lock-in amplifier.

- In chapter 2 we will present different methods for the calibration of an AFM cantilever. Different methods, such as calibration using the geometry of the cantilever, added mass method, Sader method, thermal noise and hydrodynamic drag method, will be part of the discussion for both vertical and lateral calibrations of the cantilever. For the vertical force calibration, we will use the hydrodynamic drag method to measure the normal spring constant of the cantilever. This method has been chosen over the other because of the simplicity of the operation and higher accuracy for the calibration of the colloidal probe. Similarly, for the lateral force calibration, we will perform a hydrodynamic drag experiment where the viscous drag force and the torque on the AFM probe close to a laterally moving substrate will be measured. The hydrodynamic drag induces a twist of the cantilever, and subsequently changes the lateral deflection signals. The linear fit of the plot between the torque produced in the cantilever and the change in lateral deflection signal will give the lateral conversion factor.

- In chapter 3 we will discuss the viscoelastic properties of soft and thin Poly DiMethyl Siloxane (PDMS) films. The measurements will be performed by oscillating a colloidal probe normal to the film. We will be interested in contactless hydrodynamic interaction resulting from the nanoscale flows between the probe and sample at different excitation frequencies. To examine the interaction at a very small distance, we perform numerical calculation by solving the Navier-Stokes equation in the framework of lubrication approximation. Using the numerical estimations, we will fit the experimental results and extract the loss and storage moduli at different working frequencies.

- In chapter 4 we will present the measurement of the friction between polystyrene microparticles using the dynamic AFM method. Our measurement will be aiming to validate Lobry's model that links the viscosity to the friction and also links the shear thinning to the load-dependent friction coefficient. The normal and friction forces between two approaching microspheres will be measured by recording the deflection and the twist produced in the colloidal probe, respectively. The friction coefficient and its variation with the normal force will be determined. Our collaborators will perform the rheometric experiments for the measurement of the viscosity of the suspensions (made of same particles that will be used in the AFM experiment) for several particle volume fractions. The measured friction coefficient and viscosity of the suspension will be introduced in Lobry's model to check its validity.

Chapter 1

Instruments and Techniques used in this Thesis

Contents

1.1 Atomic Force Microscope 5
    1.1.1 Operating Modes of an AFM 7
    1.1.2 Force Distance curve 8
1.2 Experimental Techniques and Instruments 9
    1.2.1 Colloidal Probes 9
    1.2.2 Roughness Measurement 12
    1.2.3 Piezoelectric Actuator 13
    1.2.4 Lock in Amplifier 16
1.3 The characteristics of the probes 18
1.4 Conclusion 20

1.1 Atomic Force Microscope

Scanning Tunneling Microscope (STM), which was invented back in 1981, enables the topographic imaging at atomic scale [53, 54]. In STM operations, an extremely sharp conducting tip is used to sense the surface. When the tip is brought very close to the probing surface, a bias voltage applied between the tip and surface allows electrons to tunnel through the vacuum between the tip and the surface. This tunneling current is a function of the applied voltage, the local charge density of the sample and the tip-sample separation. The topographic properties of the surface are acquired by monitoring the current during the scanning of the surface. However, one of the major limitation in STM was the requirement of a conductive surface for the study. This paved way for further research and led to the invention of atomic force microscope [55]. In AFM, the deflection of the cantilever that interacts with the probed surface is measured.

AFM has become one of the empowering technology for high-precision studies of materials and biological samples [56]. It provides valuable information about the material properties such as its elasticity, hardness, adhesion, surface charge density, etc. This technology is not only having higher application aspects than its competitors, but it also enables imaging of both insulator and conductive materials, up to atomic resolution. Moreover, AFM allows the measurement of interaction forces in the liquids [16,57,58].

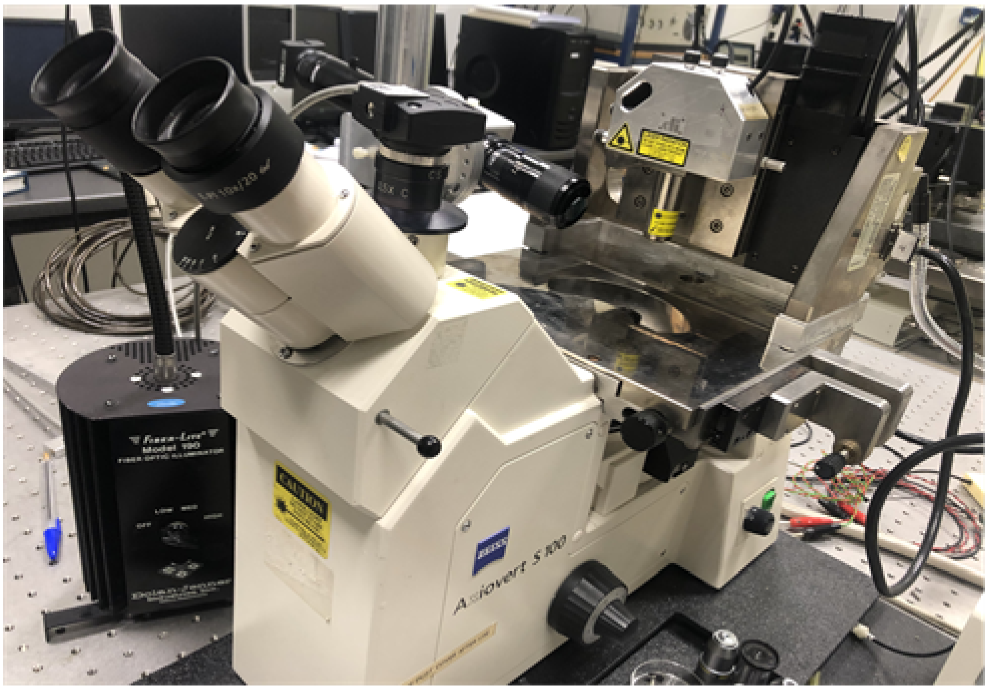

Figure 1.1: Bioscope II AFM used for the experiments.

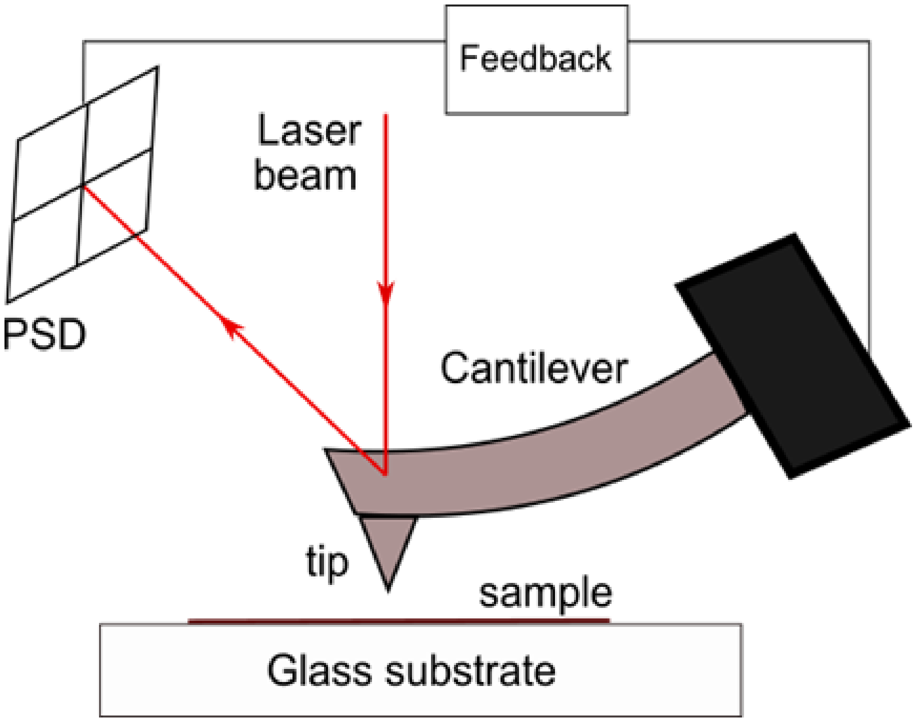

Figure 1.2: Schematic of an AFM.

The Bioscope II AFM (Bruker, USA), shown in figure 1.1, was used for the experimental work presented in this thesis. The schematic of the AFM is shown in figure 1.2. An AFM cantilever with a sharp tip is fixed in the cantilever holder and mounted on the AFM head. The optical lever technique [59] was used to measure the deflection of the cantilever. A laser beam reflects from the back side of the AFM cantilever tip that is usually coated with some reflective material, like gold or aluminum to increase its optical reflectivity. The reflected beam falls on the four quadrants photosensitive detector. When the tip and the surface interact, the cantilever deflects and the position of the reflected beam on the detector changes. This modifies the electrical signal produced by the photo diode. These signals from the detector are used to measure the force between the tip and the sample [16].

1.1.1 Operating Modes of an AFM

An AFM operates in the following two modes: static mode (contact mode) and dynamic mode.

Static Mode

This is the basic mode of operation where the cantilever remains in contact with sample during the scanning. In the course of scanning the topography of the sample induces a vertical deflection of the cantilever. In order to maintain a constant deflection, a feedback loop is set to impose a vertical displacement to the piezo corresponding to the local height of the sample. Thus, the cantilever follows the pattern and the height profile of the sample is recorded. Usually, a soft cantilever is preferably used to avoid sample deformation.

The effect of large lateral force (frictional force) during scanning is one of the greatest challenges in the static mode. This technique can be destructive for both the AFM tip and the sample, especially when probing a fragile biological sample [60]. Moreover, this may also cause instability in the feedback loop [61]. These limitations (in the static mode) were the stimulus for the development of the dynamic mode AFM [62].

Dynamic Mode

In this mode of operation, the cantilever is excited using an external and known value of force. As soon as the cantilever comes in contact with the sample, the amplitude and the phase of the deflection signal changes. The oscillation amplitude and the phase variations are measured to extract the interaction force and atomic scale properties of the sample.

Amplitude Modulation (AM) AFM [55] and Frequency Modulation (FM) AFM [63] are two basic operation modes in dynamic force measurement. In the AM AFM mode, the excitation frequency is fixed at a well-defined value (generally close to the resonance frequency) and the amplitude and the phase of the cantilever oscillation are measured. The frequency close to the resonance ensures maximum response oscillations. In this mode, the amplitude's variation is not instant, but behaves on a timescale $t \sim Q/f$. A better sensitivity is obtained for a high-quality factor, but it is detrimental in time response. During the imaging of topographies, the amplitude is kept constant at a given value via a feedback loop [64]. In addition to the topographic imaging, the phase image (refers to the monitoring of the phase lag between the input and output signal) is recorded that helps to distinguish the regions with different mechanical properties in a heterogeneous sample. The phase shift reflects the changes in the mechanical properties of the sample surface.

In FM AFM mode, the change in the resonance frequency and damping are measured for a cantilever that is excited at its resonance. The resonance frequency of the cantilever depends on the force of interaction between the probe and the substrate. This technique not only gives high dynamic sensitivity along with high-quality factor, but the time response is also not very high [65, 66]. During the imaging, a feedback is used to keep the cantilever oscillating at the resonance frequency. The amplitude of the cantilever oscillation tends to decrease because of dissipation during the interaction with the sample, but feedback monitors the excitation force to keep the constant oscillation of amplitude [63].

The dynamic mode is further classified into two: the intermittent contact mode and the non-contact mode. First, in the intermittent contact mode the AFM tip is oscillated at high amplitudes, thereby, switching in both attractive and repulsive force regions; two, in the non-contact mode the tip is mainly located in attractive force region and the tip is oscillated at smaller amplitudes closer to the substrate. Nevertheless, in both of these dynamic mode cases the applied load will be far less than that of the static mode. That is why, the dynamic mode AFM is considered as a better choice to study the soft samples [67–69].

1.1.2 Force Distance curve

A force–distance curve [16] is a presentation of the force experienced by the AFM cantilever versus the distance between the AFM tip and the sample surface (see figure 1.3). The AFM tip and the sample approach each other till the contact and then get separated by moving the tip or the sample in the z-direction, i.e. perpendicular to the sample surface, using a piezoelectric actuator. Two signals, the deflection of the cantilever Z_c and the displacement of the piezo Z_p are acquired while varying the tip–sample distance. The conversion of the deflection into a force and of the piezo displacement into the tip–sample distance are explained below.

According to the two directions of movement, a force–distance curve is described by the approach (blue curve in figure 1.3) and retraction (red curve in figure 1.3) curves. A force–distance curves is roughly divided into three regions: the zero line, the discontinuity and the contact line.

- We obtain the zero line when the distance between the AFM tip and sample is so large that no measurable force is acting between them.
- The region where the tip snaps abruptly onto the sample surface or detaches from sample surface is defined as the discontinuity region. In the approach curve the tip snaps abruptly to the sample at small distance when the gradient of the attractive force exceeds the spring constant of the cantilever, whereas, in the retract curve it detaches from the sample when the force (the cantilever deflection × stiffness) exceeds the adhesion force.
- The contact line represents the part of curve where the tip is in contact with the sample. The AFM cantilever tip is pushed against the sample and probably indenting it. The deflection sensitivity is also deduced from the contact line.

For the smaller cantilever deflection, the force is given by $F = k_c Z_c$. Where k_c is the spring constant of the cantilever and F is the force applied on the cantilever. Once Z_c

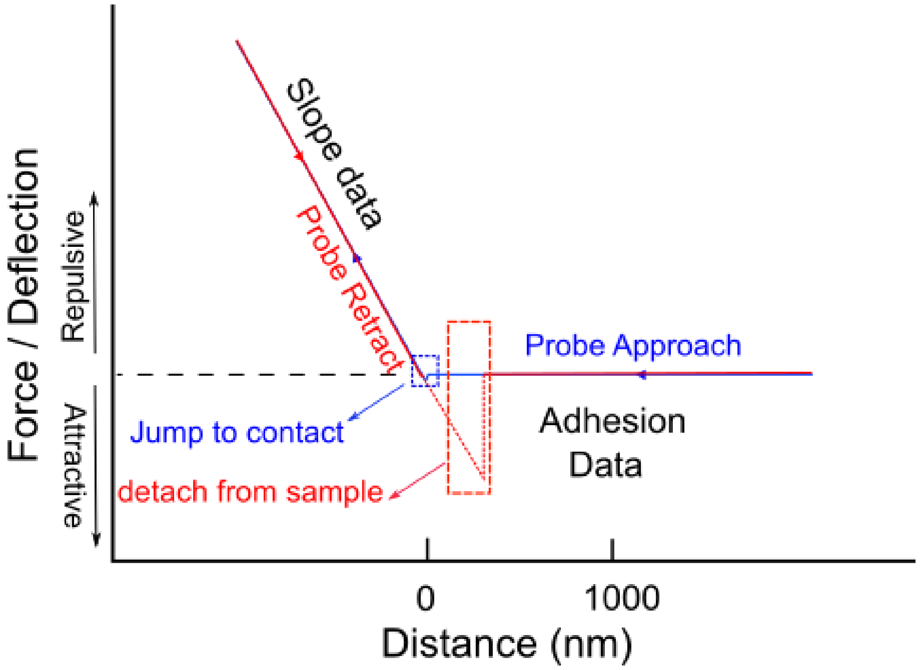

Figure 1.3: Schematic of a typical AFM cantilever deflection/force against the tip-sample separation. The blue line is depicting the approach of the probe to the sample, while the red line is for the retraction of the cantilever. The curve in the attractive region is depicting the force of adhesion during the contact.

and k_c are known (see section 2.2 for the measurement of the deflection and section 2.2.5 for the calibration of the cantilever), the applied force can be calculated by multiplying them.

The tip-sample distance is calculated by adding the cantilever deflection and the piezo position i.e. $D = Z_c + Z_p$ [16, 70].

1.2 Experimental Techniques and Instruments

1.2.1 Colloidal Probes

The AFM probes have distinctive features such as, the shape, length and the tip size of the cantilever and are chosen according to the experimental needs. In the early years, the cantilevers used in an AFM experiment were made from the wires and designed in different shapes, but the development of micro-fabricated techniques completely replaced those initial techniques. Micro-fabricated cantilevers were invented by C. F. Quate [71, 72] and Wolter [73] that are still used in AFM measurements. The cantilevers used in this research work are triangular (V-shaped) and rectangular in shape, as shown in figure 1.4(a) and 1.4(b), respectively. Instead of using these bare cantilevers we glued a sphere to the tip of these cantilevers to obtain a colloidal probe [7, 74].

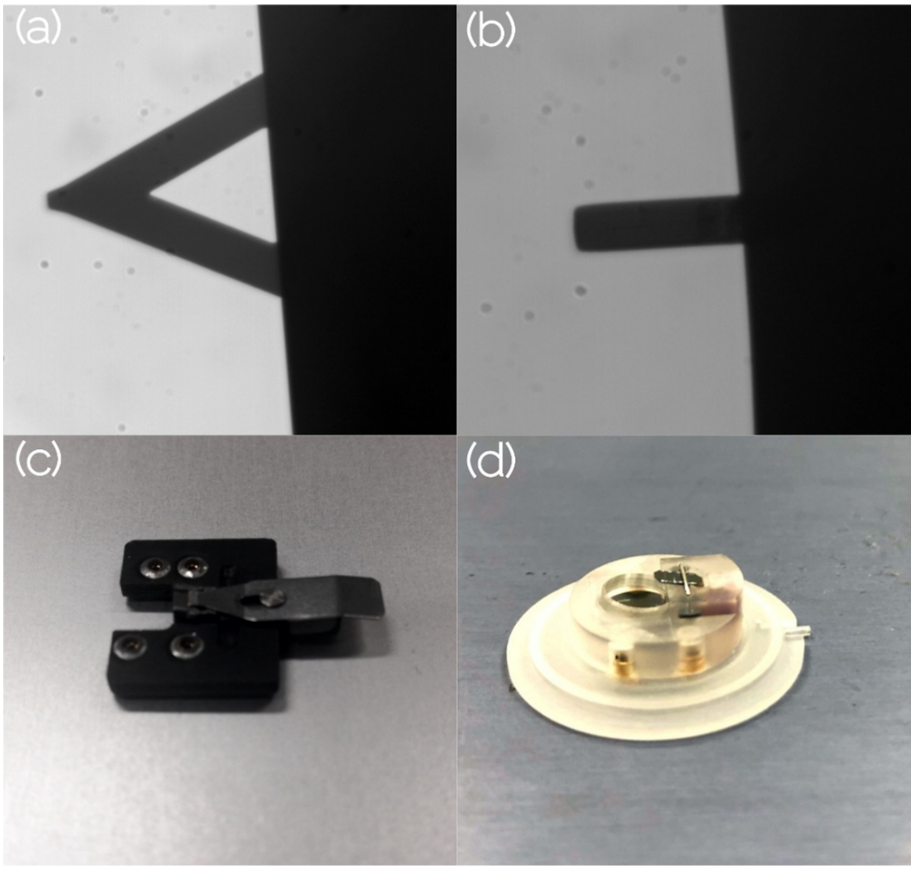

Figure 1.4: The type of cantilevers used in this research work: on the top (a) V-shaped cantilever (SNL -10 wide (B), Bruker) used in viscoelastic experiments (b) Rectangular cantilever (NSG-11 tipless, long 130μm length and width 35 μm, NT-MDT) used in friction experiments (c) and (d) are cantilever holders used in air and liquid, respectively.

Colloidal probes are commonly used in rheological AFM experiments because of their numerous advantages, such as: first, colloidal probes offer a large area of contact that allows quantitative measurement of force at higher sensitivity [16]; second, the colloidal probe has well-defined interaction geometry (usually spheres are used) and provides an easier interpretation of the data in terms of theoretical models [75]; third, colloidal probes give flexibility in choosing the material and its geometry [76]. In this thesis the colloidal probes are used to measure the viscoelastic properties of PDMS substrates and the friction between the polystyrene microspheres.

The cantilever used in experiment is fixed in the holder, before placing the holder on the head of the AFM. The holders used in this research work are shown in figure 1.4(c, d). The holder in figure 1.4(c) is used for the experiments in air while the holder in figure 1.4(d), also mentioned as liquid cell, is used in liquid environment.

How to obtain a Colloidal probe

A locally made three-axis moveable stage is used to attach a sphere to an AFM cantilever tip. The stage is placed on an optical microscope (B2 series, Motic microscope) platform to focus on the cantilever tip. The moveable stage on the microscope platform is shown in figure 1.6(a). The colloidal probes are obtained in the following steps (see figure 1.5) :

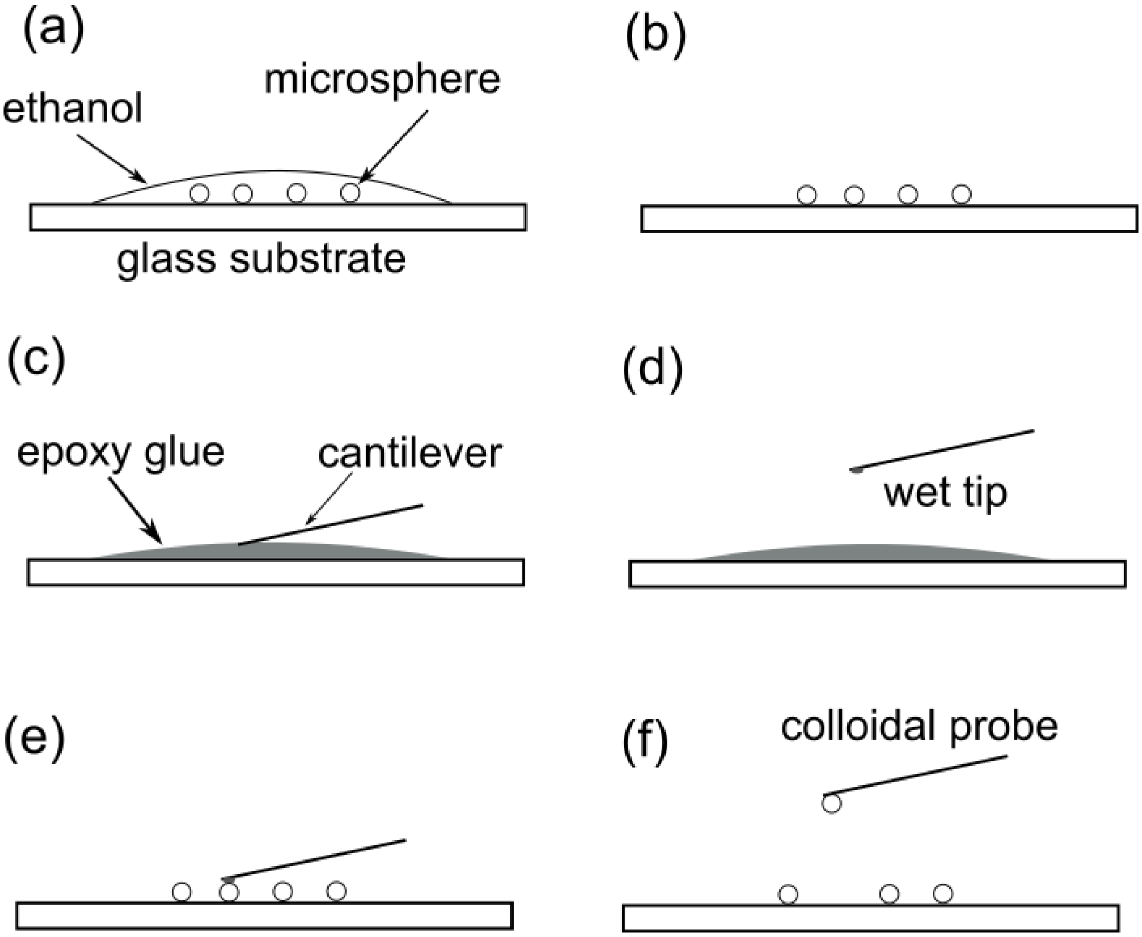

Figure 1.5: In series of figures the process to obtain a colloidal probes is depicted.

- The microparticles are rinsed in pure water and then cleaned in ethanol solution under ultrasonic tratment for a long time.
- We wash and rinse a glass substrate with pure water and repeated the process with ethanol. We use a jet of filtered air to dry the substrate after each washing. A few drops from the well-shaked ethanol solution are spread on this glass substrate. After the evaporation of the ethanol, the clean microspheres are left on the substrate.
- We fix the AFM cantilever on to the leg of the three-axis moveable stage and place under microscope to focus on the tip. The leg is tilted at an angle of 13° with the horizontal direction.
- We prepare and deposit a thin epoxy glue (Araldite) layer on the glass substrate. While observing it in the microscope, the cantilever tip is moved down towards the glue and after a gentle touch we moved back the wet tip.
- Afterwards the glass substrate containing the glue is replaced with the substrate having the spheres on it. We focus on one of the sphere on the substrate and moved down the cantilever with the wet tip to make a contact with the sphere.
- We maintain the wet tip and sphere in contact for several minutes for cross link of epoxy glue. Then we move the cantilever with attached microsphere away from the

substrate to obtain the colloidal probe.

After glueing the sphere, we measured the size of the spherical probe using an optical microscope. We have used the calibrated slide (Motic) having discs of diameter of 70μm and 150μm for the calibration of pixels of the camera (DCC 1545, ThorLabs). As an example, a colloidal probe is shown in figure 1.6(b) and the radius of the attached microsphere is measured as $40\mu m$.

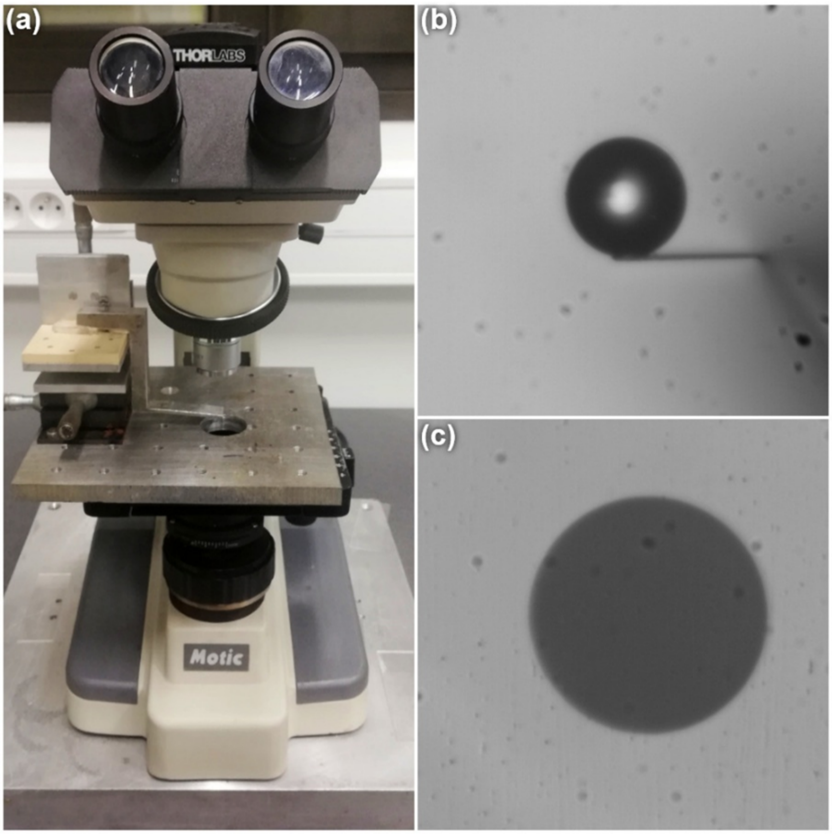

Figure 1.6: (a) The three axis moveable stage on microscope platform that is used to glue sphere to the AFM tip. (b) A colloidal probe image: microsphere with diameter of 80μm is glued to rectangular cantilever (NSG-11/tipless) (c) 150μm disc is shown from calibrated slide (Motic), which is used for the calibration of the optical images.

1.2.2 Roughness Measurement

The roughness of the spheres is obtained from the AFM image of the sphere. The substrate with glued microspheres is fixed on the multi-axis piezo stage, and a standard cantilever (having a sharp tip) is used to perform the roughness measurement. After adjusting the laser on the cantilever, we centered the cantilever tip to one of the sphere on substrate using optical microscope. For precise centering, we engaged the probe with a sphere and by adjusting the x- and y-axis piezo offset, we obtain the exact center of the probed sphere. We perform scanning at 90° scan angle, so each line of the image is obtained by scanning the sphere in direction perpendicular to the long axis of the cantilever. An example is shown in figure 1.7, where the 3D AFM height image and section analysis for a microsphere are presented.

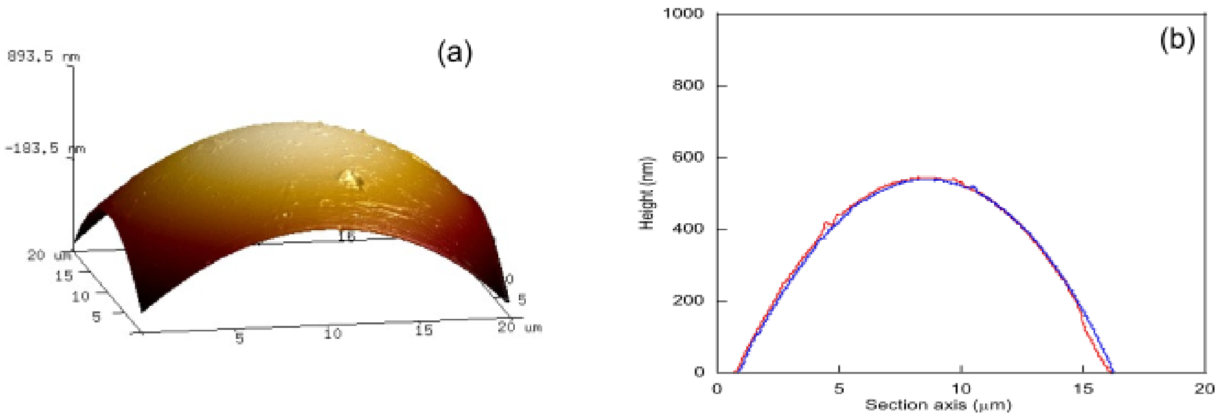

Figure 1.7: (a) The 3D AFM height image and (b) height section analysis for a microsphere are shown.

1.2.3 Piezoelectric Actuator

In our measurements, we required to scan the sample either in vertical or lateral direction depending on the experiment. For this purpose, we have used a multi-axis piezo stage (MAD CITY LABS) with a large travel range to control the position of the sample (see figure 1.8). The device gives high load capacity, fast time response and subnanometer resolution.

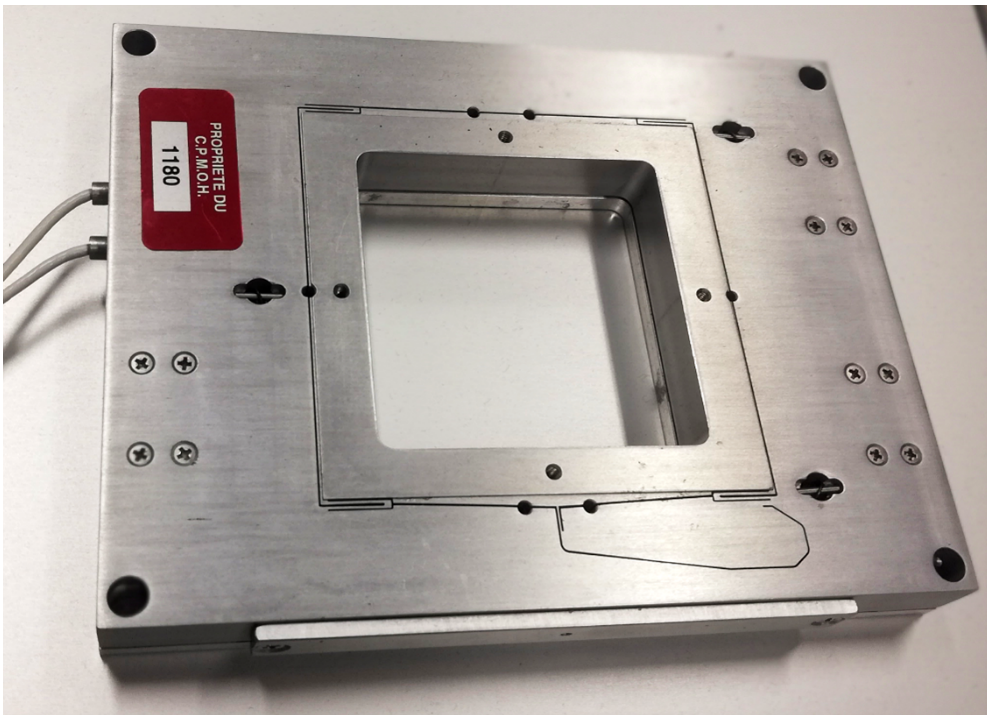

Figure 1.8: Image of the three-axis Piezo stage (NanoT series, Mad City Labs) used in this experimental work.

However, in practical applications there exist hysteresis characteristics in piezoelectric materials, which seriously affects the control accuracy of the piezoelectric stage [77]. The piezo was deriven under closed loop using the controller model (NanoT series, Mad City Labs). In this technology, the resistive strain gauges sensors are mounted on the piezo-electric. These are specifically designed for the closed-loop configurations, which allows to reduce the hysteresis in the displacement of the piezo when the input driving voltage is varied.

An accurate calibration of the piezo for the applied voltages is mandatory to obtain a quantitative information about the piezo displacement.

Vertical Displacement Calibration

The vertical displacement of the piezo is calibrated using an optical camera. This is one of the simple methods. A microscopic calibrated slide (Motic), which is having calibrated grids and the calibrated discs of diameter of $70\mu m$ and $150\mu m$, is fixed on the piezo stage. We track the motion of one of the disc for the given driving voltage and frequency. The piezo displacement is obtained by observing the extreme positions of the disc. The piezo calibration at driving frequency of $0.1 Hz$ and different driving amplitude is presented in figure 1.9. The linear fitting of the data points gives the piezo displacement as $4.88 \pm 0.03 \mu m/V$.

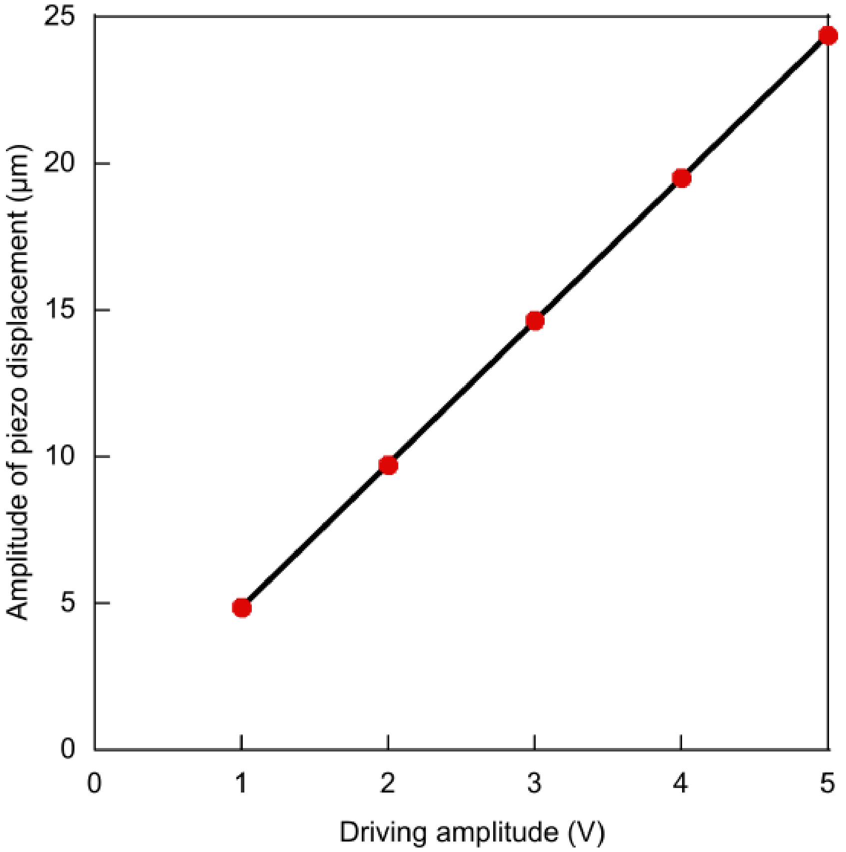

Figure 1.9: The measured amplitude of the piezo displacement is shown versus the driving amplitude. The linear fit (black line) gives piezo displacement per unit driving voltage as $4.88 \pm 0.03 \mu m/V$.

Lateral Displacement Calibration

The lateral displacement of the piezo is calibrated using a calibrated grating having a pitch of $0.9\mu m$. The piezo is imposed to oscillate laterally after the cantilever comes in contact with the grating. We have recorded both the voltage applied to the piezo and the cantilever deflection to count the number of peaks for the given value of the input (applied voltage and frequency). By multiplying the number of peaks to the pitch of the grating, the piezo displacement is obtained. For the case of a driving amplitude of $2V$ and the driving frequency of $25Hz$, we count 20 peaks that corresponds to a piezo displacement of $18\mu m$ (see figure 1.10). However, it is observed that the oscillation amplitude of the piezo decreases for the large driving frequencies at the same driving amplitude, as shown in table 1.1. The piezo displacement reduce to $6.04\mu m$ at driving frequency of $50Hz$ for the same driving amplitude (i.e. $2V$).

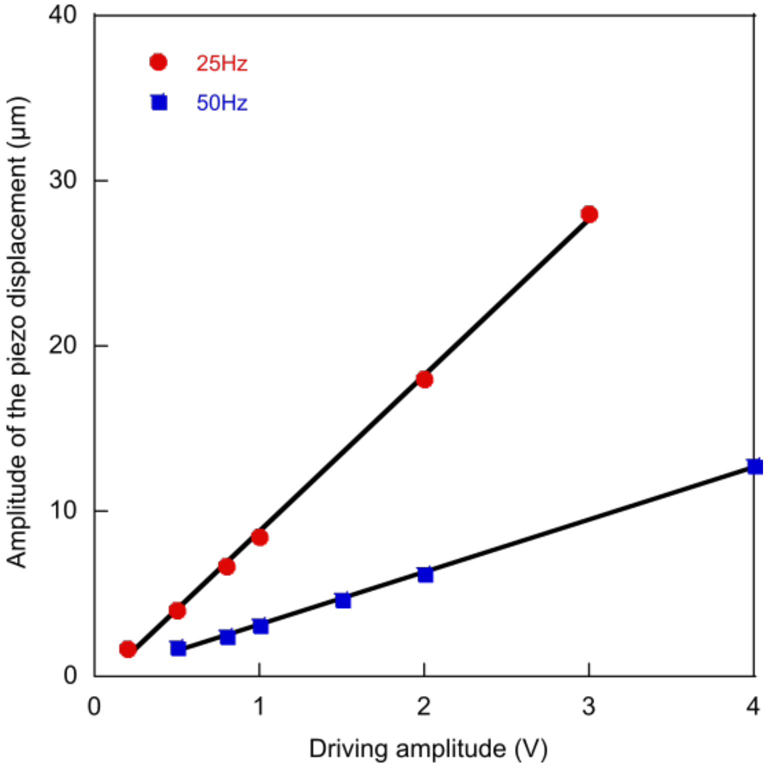

Figure 1.10: The piezo calibration for two driving frequencies at different driving amplitudes is presented. The linear fit (black line) gives the amplitude of the piezo displacement per volt for the respective driving frequency. The values are extracted as $9.46\mu m/V$ and $3.02\mu m/V$ for the driving frequency of $25Hz$ and $50Hz$, respectively.

Table 1.1: The measured lateral displacement values at driving amplitude of 1V are shown at different driving frequencies.

Driving frequency (Hz)	Piezo lateral displacement (μm)
25	9.46
50	3.02
100	1.25

In figure 1.10, the measured amplitude of piezo displacement is plotted against the driving amplitude. We obtain piezo displacement of $9.46\mu m/V$ and $3.02\mu m/V$ for the driving frequency of $25Hz$ and $50Hz$, respectively.

Furthermore, during the experiment, we have also recorded the output of the piezo (in volts) to be sure about the exact value of the vertical and lateral displacements. The measured value is converted to nanometer by multiplying to the standard per volt value for the vertical ($4.9\mu m/V$) and lateral ($20\mu m/V$, at driving frequency of 1Hz) displacement. As an example, the lateral output signal of the piezo at the driving frequency of $100Hz$ and driving amplitude of $1V$ is shown in figure 1.11. We have extracted the value for the amplitude of the output signal by fitting the curve using sine wave equation as $1.25 \pm 0.1\mu m$.

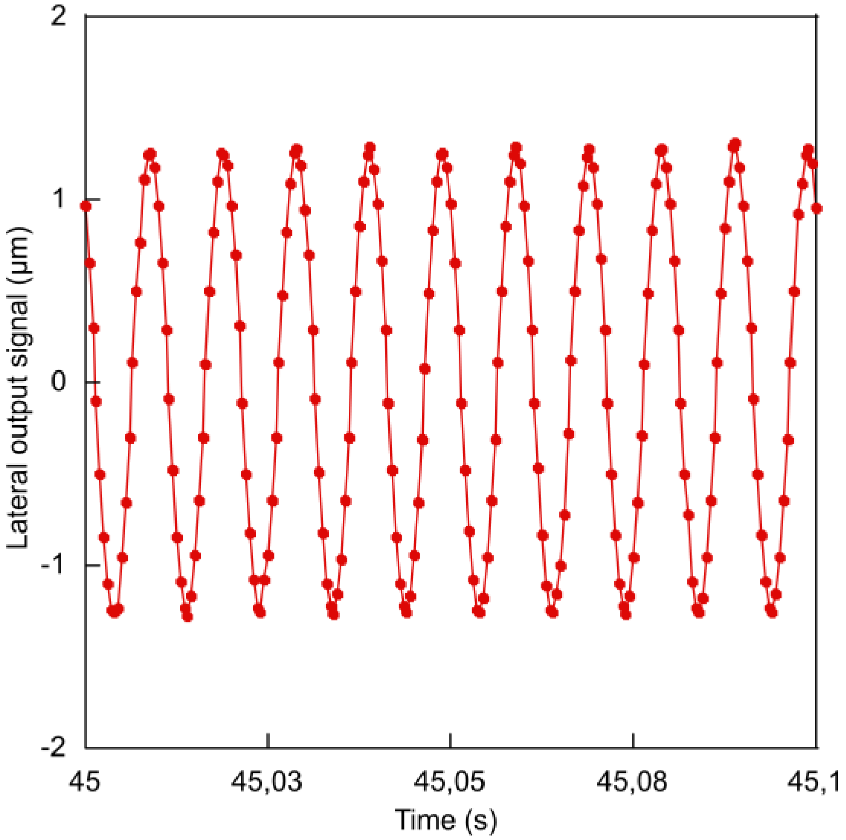

Figure 1.11: The measured lateral output signal of the piezo is shown for the driving frequency of $100Hz$ and the driving amplitude of $1V$. The amplitude of the lateral displacement is extracted as $1272nm$.

1.2.4 Lock in Amplifier

Lock-in amplifiers are used to measure the signal amplitude and the phase in relation to a defined reference signal. It can be thought of as a band pass filter, which is having a small bandwith and high quality factor. It is capable of extracting signals even in noisy environments. It extracts signals in a defined band of frequency around the reference frequency and effectively rejects all the other frequencies. A low pass filter set up is used to measure the amplitude and the phase in relation to the reference. In principle, a lock-in amplifier mixes the input signal with the reference signal (figure 1.12 mixer) and that is followed by passing it through a low pass filter to obtain the output (figure 1.12 low pass filter) [66].

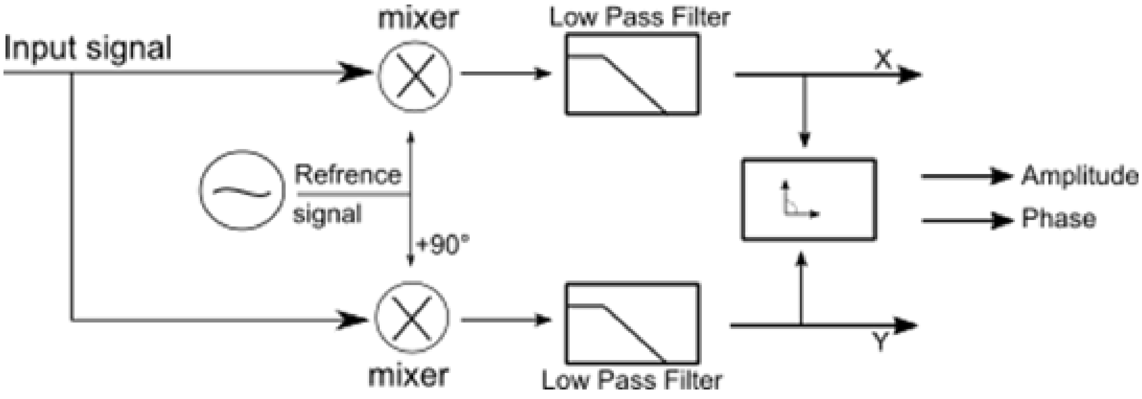

Figure 1.12: Schematic diagram for the working of the lock in amplifier.

The time constant and Dynamic Reserve (DR) play an important role in the standard operation of the lock-in amplifier. The time constant displayed on the front panel of the lock-in amplifier, is the time response of the low-pass filter. The time response is adjusted to provide an optimal balance of the responsiveness and the stability. For instance, when the time constant is very low, the lock-in gives an abrupt voltage response to a change in the input signal, but the voltage reading is hardly stable enough for the precise measurement. On the other hand, when the time constant is high, the voltage reading is stable but the change in the input signal for high frequency responses can not be measured.

The DR is also a controllable parameter and is defined as the largest acceptable noise-to-signal ratio. The actual value of the DR is not displayed on the panel but can be adjusted from high to low. It should be kept as low as possible without overloading the system. For a digital lock-in amplifier, the high DR results in more output noise from the analog to digital converter. The DR is expressed in decibels (dB) and calculated using the following relation:

$$DR = 20 \times \log_{10}\left(\frac{2}{sens}\right) - ACgain \tag{1.1}$$

Where $sens$ is the sensitivity (displayed on the front panel), which can be set to any value between $10nV$ to $1V$ according to the experimental requirement. $ACgain$ is set to $0dB$ i.e. to the input limit of $1.6V$ during the experiments.

For the measurements presented in chapter 3, we have used lock-in amplifier (DSP 7280, Signal Recovery), as shown in figure 1.13, to excite the cantilever. The motion of cantilever is detected at excitation frequency and driving amplitude, while using internal reference signal. The cantilever deflection (vertical or lateral, depending on the experiment) is set as the input of the lock-in amplifier. The output amplitude $A(V)$ and phase ϕ (rad) of the cantilever oscillation are obtained from the output (rear panel) of the lock-in amplifier. These output signals are recorded using an analog to digital (A/D) acquisition board (PCI-4462, National InstrumentUSA).

Figure 1.13: Lock in Amplifier model 7280 DSP used in experimental work.

1.3 The characteristics of the probes

A few of fundamental characteristics of this research work are enumerated as follow:

Spring Constant (Vertical Stiffness) of the cantilever
In order to measure the deflection caused by the interaction forces, the information regarding the vertical stiffness of the cantilever is necessary. In contact, the force F_z (also referred as the normal force F_n) that deflects the cantilever in the vertical direction is given as $F_z = F_n = Z_c k_c$ (figure 1.14(a)).

Torsional or Lateral Spring Constant of the cantilever
The lateral force F_l is typically used in the surface friction measurements where the cantilever is used to scan the surface in the direction perpendicular to the long axis of the cantilever. This results in a twist in the cantilever and subsequently, the lateral output voltage at the detector changes. The measured lateral voltage V_y is then converted to force using the calibration values [78, 79].

If y and k_y are the lateral displacement and the lateral spring constant of the cantilever, the lateral force will be given by: $F_l = y k_l$.

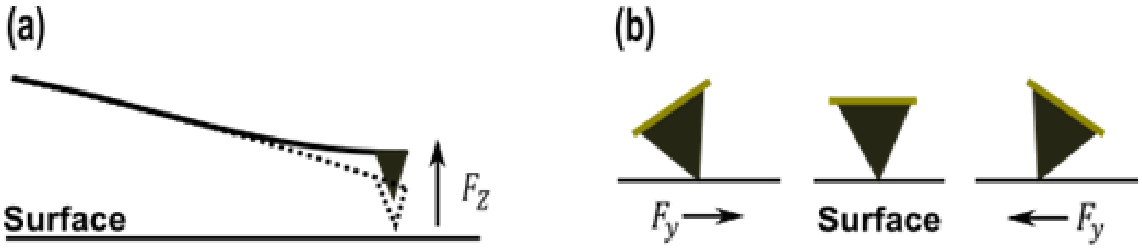

Figure 1.14: (a) the bending of cantilever for the applied force is shown (b) cantilever at normal position in the middle and it twisted for the applied lateral force in opposite direction to lateral displacement.

Effective Mass of the cantilever

In case of one dimensional motion of the cantilever having uniform cross-sectional area A, the effective mass m^* of the cantilever will be defined as: [80]

$$m^* = \rho A \int_0^l (\chi(x))^2 dx, \tag{1.2}$$

and

$$\frac{m^*}{m} = \frac{1}{l} \int_0^l (\chi(x))^2 dx = \frac{1}{4}. \tag{1.3}$$

Where ρ is the density, l is the length and $\chi(x)$ is the beam profile of the cantilever (see section 2.2.1). Equation 1.3 tells us that the ratio m^*/m is mode independent and that the effective mass of the cantilever is constant, which is equal to $1/4$ of geometric mass [81].

Resonant Frequency

The successive peaks of resonance are obtained by exciting the system with the small amplitude oscillation at varying driving frequencies. The resonance is indicated by the peak of the amplitude as the function of the frequency [82]. However, the amplitude shift to a lower value for the succeeding resonances.

The angular frequency ω_0 of the oscillator relates to the cantilever stiffness and its effective mass as:

$$\omega_0 = \sqrt{\frac{k_c}{m^*}}. \tag{1.4}$$

Quality Factor

The quality factor Q of a cantilever specifies the damping present in the system. The bulk quality factor of the cantilever is given by:

$$Q = \frac{m^* \omega}{\gamma_b}, \tag{1.5}$$

where ω is the oscillation of cantilever in the fluid and γ_b is the bulk damping coefficient of the cantilever in the absence of the interaction force. For a cantilever of length l and width w, the resulting damping coefficient is given by following expression [83]:

$$\gamma_b = \rho_f \frac{\pi^2}{4} w^2 l \omega \Gamma_i, \tag{1.6}$$

where Γ_i is the imaginary part of the hydrodynamic function (see section 2.2.3, for details) [84]. An additional force $(-\gamma_{int} V)$ is exerted on the cantilever during the hydrodynamic interaction with the sample and the total force is given as:

$$F = -\gamma_{tot} V = -(\gamma_{int} + \gamma_b) V, \tag{1.7}$$

where V is the velocity of the cantilever and the total damping γ_{tot} is the sum of γ_{int} the damping due to the squeezed fluid and γ_b the bulk damping [85]. Thus the qulity factor is given as:

$$Q = \frac{m^* \omega}{\gamma_b + \gamma_{int}}, \tag{1.8}$$

1.4 Conclusion

AFM is introduced as a valuable tool to perform topographic imaging and interaction force measurements. This is followed by a disscussion about the method to obtain a colloidal probe. A few of the characteristics of the AFM probe are highlighted. The experimental techniques including the roughness characterization of the spheres and the calibration of the piezo are also presented.

Chapter 2

Calibrations

Contents

2.1 Introduction 21

2.2 Normal Spring Constant Calibration 22

2.2.1 Geometry of Cantilever 22

2.2.2 Added Mass Method 26

2.2.3 Normal Sader Method 27

2.2.4 Thermal Noise Method 28

2.2.5 Hydrodynamic Drag Method 31

2.3 Lateral Force Calibration 36

2.3.1 Geometry of Cantilever 36

2.3.2 Torsional Sader Method 37

2.3.3 Torsional Cleveland Method 38

2.3.4 Thermal Noise Method 38

2.3.5 Hydrodynamic Drag Method 39

2.4 Conclusion 43

2.1 Introduction

Atomic force microscopy has found gradual increase in number of applications, but a quantitative and comprehensive measurement cannot be materialized without a calibration of the AFM cantilever. Irrespective of the mode of operation, the signals are measured in volts and that need to be calibrated accurately for the calculation of force. In short, the cantilever calibration is the primary requirement to conduct AFM studies.

Usually manufacturers provide the value of the spring constant of the cantilevers, but those are not highly accurate. In addition, attachment of the sphere to the cantilever, in many experiments, also alters the spring constant because of the length variation. Thus, it is necessary for the handler to conduct proper calibration of the spring constant of the cantilever. Many calibration techniques have been introduced over the years, but no single method can be considered as the ultimate solution to the problem. The sections

2.2 and 2.3 cover different methodologies used to calibrate the vertical and the lateral stiffness, respectively. This will not only provide a thorough comparison between various methods used for the calibration but will also help to analyze different methods suitable for different experiments.

2.2 Normal Spring Constant Calibration

The simplest description for the normal spring constant of the cantilever is that it relates the applied load to the subsequent bend of the cantilever. It is expressed using the following relation [86]:

$$k_c = \frac{F}{Z_c}. \tag{2.1}$$

The bending of the cantilever causes a change in the position of the reflected laser on the photo sensitive detector, and as a result changes the measured signal. If ΔV_n is the change in the signal then the deflection of the cantilever is expressed as:

$$Z_c = \frac{\Delta V_n}{\beta}, \tag{2.2}$$

where β is the deflection calibration factor that is obtained from the slope data.

The deflection Z_c (in volts) is recorded using an acquisition card (see figure 2.1(a)). It is important to note that the deflection sensitivity depends upon the laser intensity and the photo dectector sensitivity. We have used the deflection sensitivity, obtained from the linear fit of the slope data as $\beta = 0.024V/nm$ (as shown in inset of fig 2.1(a)), to convert the measured signal in volts to nanometer (see figure 2.1(b)) [16]. Finally, the distance between the probe and the substrate is obtained by adding the deflection Z_c and the the piezo displacement Z_p as $D = Z_c + Z_p$ (see figure 2.1(c)).

In next section a detailed discussion covers various methods for the vertical calibration of the cantilever.

2.2.1 Geometry of Cantilever

In this work, both, the rectangular and triangular shape cantilevers are used in different set of experiments.

Retangular Cantilever

In static situation, the expression for the deflection of a rectangular cantilever (having length l, width w and thickness e) that is deflected by a constant force (see figure 2.2(a)) is given as:

$$EI\frac{\partial^3 Z(x)}{\partial x^3} = -F. \tag{2.3}$$

Where E is the Young modulus of the cantilever, I is the moment of inertia (for a rectangular beam $I = we^3/12$) and Z is deflection of the cantilever in z direction. Integrating equation 2.3 with boundary conditions $\frac{\partial Z(x=0)}{\partial x} = 0$, $\frac{\partial^2 Z(x=l)}{\partial x^2} = 0$ and $Z(x=0) = 0$ will gives:

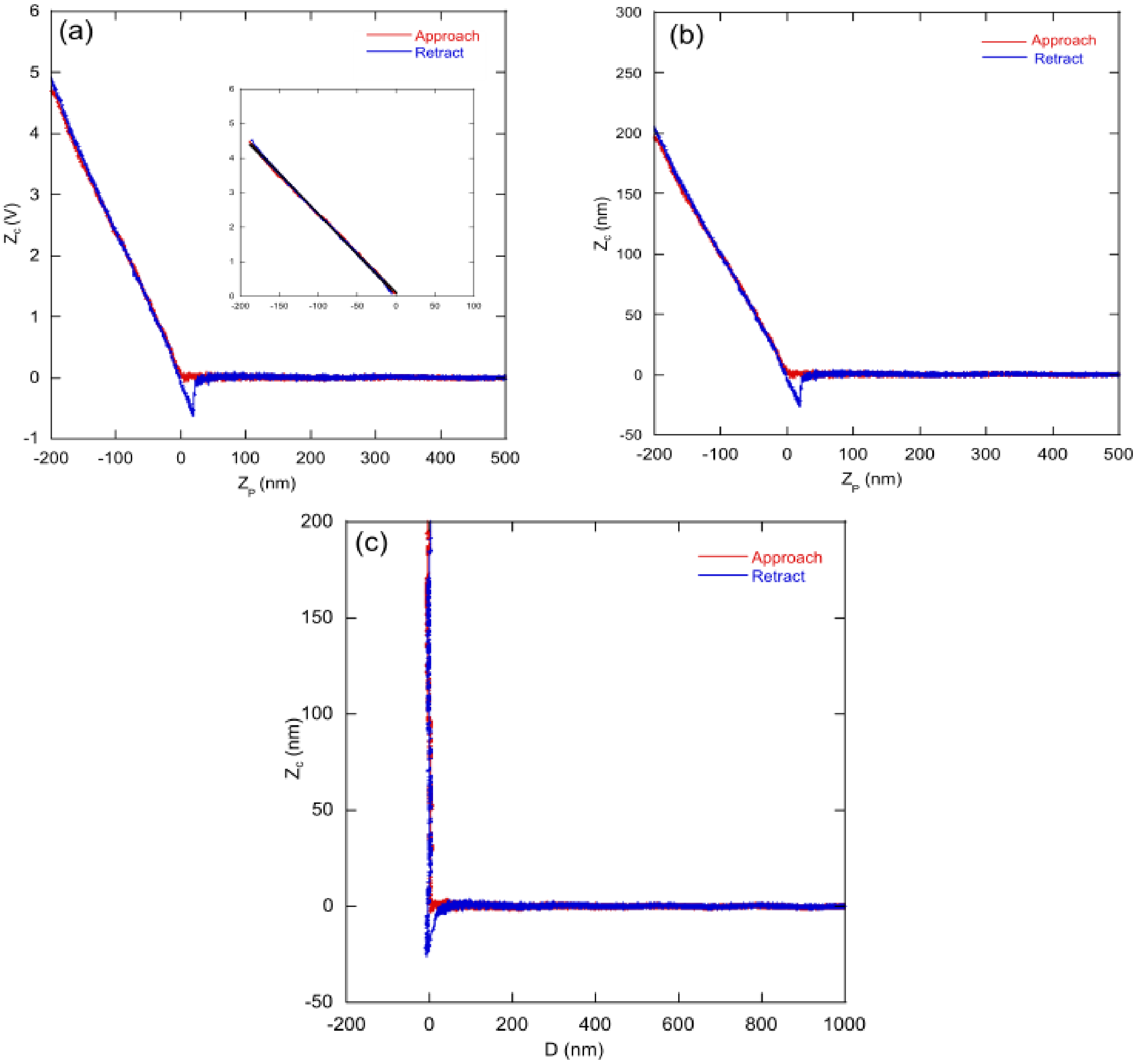

Figure 2.1: Force-distance curve is obtained using the V-shaped cantilever ($SNL-10$) on the mica surface in a liquid (a) the measured cantilever deflection Z_c is shown as function of piezo displacement Z_P. Inset of the figure shows the fit (black solid lines) to obtain the sensitivity ($\beta = 0.024$ V/nm) for the conversion of the measured deflection in volts to nanometer. (b) Z_c in nanometer as function of Z_P. (c) Z_c is shown versus the distance D, with $D = Z_c + Z_P$.

$$\frac{\partial Z(x)}{\partial x} = \frac{F}{EI}\left(lx - \frac{x^2}{2}\right), \tag{2.4}$$

and

$$Z(x) = \frac{F}{EI}\left(\frac{lx^2}{2} - \frac{x^3}{6}\right). \tag{2.5}$$

At the end of the cantilever, equations 2.4 and 2.5 become:

$$\frac{\partial Z(x=l)}{\partial x} = \frac{Fl^2}{2EI} = \frac{F}{k_c}\frac{3}{2l} = \frac{3}{2l}Z(x=l), \tag{2.6}$$

and

$$Z(x=l) = \frac{F}{EI}\frac{l^3}{3}. \tag{2.7}$$

Using the equations 2.1 and 2.7, the spring constant of the cantilever is defined as:

$$k_c = \frac{3EI}{l^3} = \frac{Ewe^3}{4l^3}, \tag{2.8}$$

and this equation is applicable when $w << l$.

Usually optical deflection method is used to measure the cantilever motion. In this method, the inclination at the end of the beam $\frac{\partial Z(x=l)}{\partial x}$ is measured instead of the cantilever deflection $Z(x=l)$ itself. Using equation 2.6, the deflection of the cantilever is related to the inclination at the end of the cantilever as [87]:

$$Z_c = Z(x=l) = \frac{2l}{3}\frac{\partial Z(x=l)}{\partial x}. \tag{2.9}$$

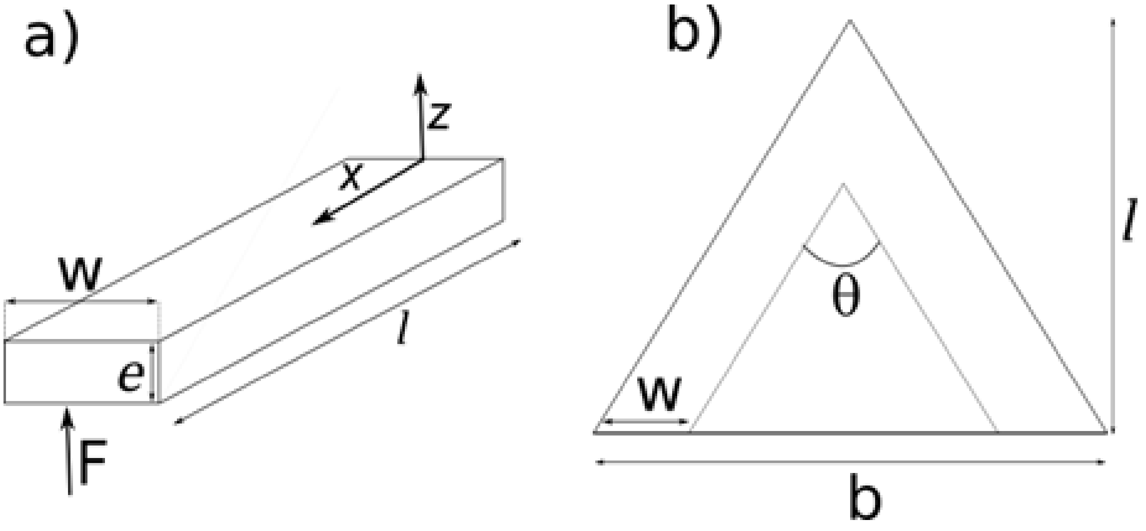

Figure 2.2: schematic of (a) rectangular and (b) triangular (V-shaped) cantilever.

In dynamic situation, the bending of the cantilever is given by Euler-Bernoulli equation as:

$$EI\frac{\partial^4 Z}{\partial x^4} + \rho we\frac{\partial^2 Z}{\partial t^2} = 0. \tag{2.10}$$

Where ρ is the density of the material. A solution for equation 2.10 is given in the following form:

$$Z(x,t) = \chi(x)a(t). \tag{2.11}$$

In equation 2.11 $\chi(x)$ is the beam profile of the cantilever and $a(t)$ is the amplitude of the cantilever oscillation. After inserting equation 2.11 in equation 2.10 and seperating the variables in equation 2.10, we get:

$$\frac{\partial^2 a(t)}{\partial t^2} = -\omega^2 a(t), \tag{2.12}$$

and

$$\frac{\partial^4 \chi(x)}{\partial x^4} = \frac{\alpha^4}{l^4}\chi(x), \tag{2.13}$$

where

$$\alpha^4 = \frac{12\rho\omega^2 l^4}{Ee^2}, \tag{2.14}$$

with ω being the angular frequency of the cantilever. At the end of the cantilever, $\chi(x)$ must satisfy the following boundary conditions [87–89]:

$$\chi(0) = 0; \frac{\partial \chi(0)}{\partial x} = 0; \frac{\partial^2 \chi(l)}{\partial x^2} = 0; \frac{\partial^3 \chi(l)}{\partial x^3} = 0;$$

We obtain the expression for $\chi(x)$ as:

$$\chi(x) = \frac{1}{2}\Bigg((\cos\frac{\alpha}{l}x - \cosh\frac{\alpha}{l}x) - (\frac{\cos\alpha + \cosh\alpha}{\sin\alpha + \sinh\alpha})(\sin\frac{\alpha}{l}x - \sinh\frac{\alpha}{l}x)\Bigg), \tag{2.15}$$

where

$$\cos\alpha\cosh\alpha + 1 = 0. \tag{2.16}$$

The solution of equation 2.16 gives values for the α for the respective modes of the cantilever vibration. The values for the first six modes are presented in table 2.1.

Table 2.1: The values for α_i, (i is the mode number), are given for the free end of the cantilever.

i	1	2	3	4	5	6
α_i	1.875	4.694	7.855	10.995	14.137	17.279

By inserting equation 2.11 and 2.15 into equation 2.9, we obtain a time-dependent relation for the deflection of the cantilever (measured using the optical deflection method) for the corresponding modes:

$$Z_c(t)_i = \frac{2\alpha_i}{3}\frac{\sin\alpha_i\sinh\alpha_i}{\sin\alpha_i + \sinh\alpha_i}a(t)_i. \tag{2.17}$$

The prefactor multiplying to the amplitude indicates that the cantilever deflection is deduced from the measurement of the inclination of the cantilever [87,88].

The cantilever stiffness k_i for each mode i is given as:

$$k_i = \frac{\alpha_i^4}{12}k_c. \tag{2.18}$$

V-shaped (triangular) cantilever:

These types of cantilevers (as shown in figure 2.2(b)) are calibrated using the parallel beam approximation. In this approximation the legs of the V-shaped cantilever are considered to be two rectangular beams attached at a point. Thus the analytical solution in case of the rectangular cantilever can be doubled to obtain the results for a V-shaped cantilever. Correspondingly, the spring constant (equation 2.8) will be [90–92]:

$$k_c = \frac{Ewe^3}{2l^3}. \tag{2.19}$$

Since, commercially available AFM cantilever are designed through Microelectromechanical System (MEMS) process, which means that geometries and shapes of the cantilevers can deviate from the aimed parameters. For instance, in the case of triangular cantilevers, most of the practically used cantilevers are not exactly V-shaped and hence the spring constant changes with slight change in the cantilever length or shape. Moreover, two rectangular beams are not really parallel, but skewed. So, equation 2.19 is no longer valid to obtain an accurate value for the spring constant. Keeping in view the complexities, various authors came up with different incremental changes to the basic equation (equation 2.19) for a V-shaped cantilever. Sader and White [93] expressed this in the following way:

$$k_c = \frac{Ewe^3}{2l^3}\left(1 + \frac{4w^3}{b^3}\right)^{-1}, \tag{2.20}$$

where b is the distance between the two beams of the V-shaped cantilever.

It should be noted that the equations (2.8, 2.19 and 2.20) are applicable, when the load is applied exactly at the tip of the free end of the cantilever. However, there is a possibility that the load might be applied at finite distance Δl back from the end of the cantilever. This results in a variation in the value of the spring constant, and now the spring constant versus the length will be $\left(\frac{l}{l-\Delta l}\right)^3$.

In our experimental work we used colloidal probes with microspheres larger in size than the tip of the AFM cantilevers. It makes it even more complicated for an accurate measurement of the point of loading along the length. We did not rely on this method for the measurement of the spring constant of the AFM cantilever.

2.2.2 Added Mass Method

In this method, which is also known as Cleveland method, the spring constant is determined by measuring the shift in the resonant frequency ω_0 of the oscillating cantilever following the addition of a known mass at the free end of the cantilever [94–96]. Typically,the attached mass is spherical in shape. The relation between the added mass M_s and the resonance frequency is given by:

$$\omega_0 = 2\pi f = \sqrt{\frac{k_c}{M_s + m^*}}, \tag{2.21}$$

or

$$M_s = \frac{k_c}{\omega_0^2} - m^*, \tag{2.22}$$

In order to find the exact value of the normal spring constant, several experiments are required by attaching different masses at the end of the cantilever. The slope of the plot $M_s \propto \omega_0^{-2}$ yields a straight line that gives the spring constant of the cantilever.

The largest uncertainty with this method is the estimation of the added mass, which is usually obtained with the measurement of the diameter of added mass. Additionally, the position of the added mass from the base of the cantilever is also important, since, this significantly affects the resonance frequency. Typically, optical microscope with image capturing ability is used to measure the diameter of the sphere and position of the sphere on the beam. The complexity and time-demanding nature of the process add to its disadvantages.

2.2.3 Normal Sader Method

This method involves the measurement of the resonance frequency ω_f and the quality factor Q for a rectangular cantilever immersed in a fluid. The dimensions of the cantilever are determined using optical microscope, while resonance frequency and quality factor are obtained by measuring the thermal noise spectrum or by exciting the cantilever [83, 86]. Normal spring constant is given by the following relation provided that the quality factor needs to be greater than unity and that the length of the cantilever is larger than the width, which in turn is larger than the thickness of the cantilever [97].

$$k_c = 0.1906\rho_f w^2 l Q \omega_f^2 \Gamma_i(\omega_f), \tag{2.23}$$

where ρ_f is the fluid density and Γ_i is the imaginary part of the hydrodynamic function. The hydrdodynamic function of an oscillating rectangular cantilever of infinite length depends on the Reynolds number Re. This parameter gives relative influence of the inertial and the viscous force, and expressed by:

$$Re = \frac{\rho_f w^2 \omega}{4\eta}, \tag{2.24}$$

where η is the fluid viscosity. For the cantilever oscillating in the fluid, one needs to consider an additional characterstic length $\delta = \sqrt{\frac{2\eta}{\rho_f \omega_f}}$, which is penetration depth length of the acoustic wave in fluid. Now the Re becomes a simple ratio of two lengths i.e. $Re = \frac{w^2}{2\delta^2}$ [83, 84, 98, 99].

For the values of the Re ranging between the 1 and 1000, the assumptotic expression for the hydrodynamic function $\Gamma(\omega_f) = \Gamma_r(\omega_f) + j\Gamma_i(\omega_f)$ is given as:

$$\Gamma(\omega_f) = a_1 + a_2\frac{\delta}{w} + j\left[b_1\frac{\delta}{w} + b_2(\frac{\delta}{w})^2\right], \tag{2.25}$$

and the parameters are: $a_1 = 1.0553$, $a_2 = 3.7997$, $b_1 = 3.8018$, and $b_2 = 2.7364$ [84].

Although this method was developed for bare cantilevers, but Green *et al* [86] proposed that equation 2.23 also holds for a cantilever, which is loaded with a sphere at the tip provided that the size of the sphere is smaller than the width of the cantilever. However, when the sphere diameter becomes comparable to or exceeds the width of the cantilever, the flow around the cantilever changes and as a result the energy dissipated per cycle also changes, which leads to an error in the calculation of the spring constant using equation 2.23.

Due to this limitation, we did not use this method for the calibration, since the diameter of the spheres (collidal probes) used in this work were exceeding the width of the cantilever.

2.2.4 Thermal Noise Method

Equipartition theorem method

The motion of the cantilever induced by the thermal excitation was measured while setting the sampling frequency and number of points in a proportional ratio. The experiment is performed in pure water far from the substrate (mica). After adjusting the laser on the tip of the probe, the temporal signals are recorded.

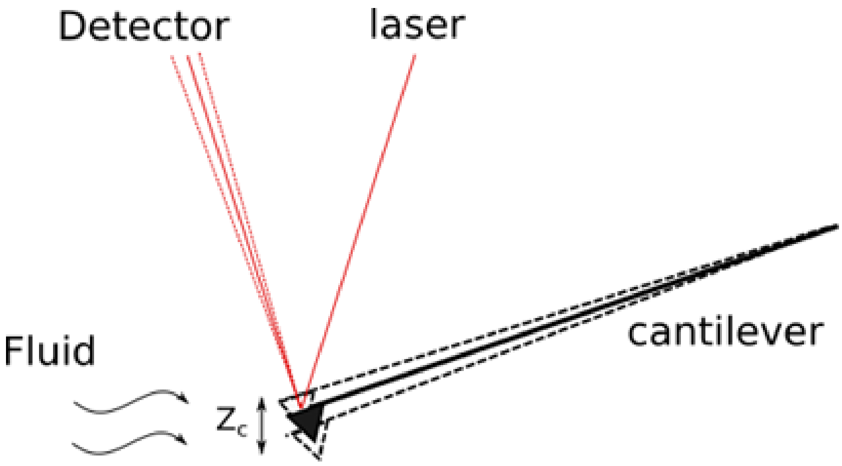

Figure 2.3: schematic is showing an oscillating AFM cantilever in fluid. The oscillation is induced by the Langevin forces.

The deflection of the cantilever for each mode is given by equation 2.17. The vibration of the cantilever is induced by the thermal excitation force. At thermal equilibrium every independent mode i is described by harmonic oscillator driven by fluctuating noise force with the mean value of energy equal to $(k_B T)/2$. Where k_B is Boltzmann's constant and T is the absolute temperature (Kelvin). Thus the mean square amplitude $\langle a_i^2 \rangle$ at the free end of the cantilever for mode i is:

$$\langle a_i^2 \rangle = \frac{k_B T}{k_i}. \tag{2.26}$$

From equation 2.18 and 2.17, we have:

$$\langle Z_c^2 \rangle = \sum_{i=0}^{\infty} \frac{4\alpha_i^2}{9} \left(\frac{\sin\alpha_i \sinh\alpha_i}{\sin\alpha_i + \sinh\alpha_i} \right)^2 \langle a_i^2 \rangle, \tag{2.27}$$

and using equation 2.26 we get:

$$\langle Z_c^2 \rangle = \frac{16}{3} \frac{k_B T}{k_c} \sum_{i=0}^{\infty} \frac{1}{\alpha_i^2} \left(\frac{\sin\alpha_i \sinh\alpha_i}{\sin\alpha_i + \sinh\alpha_i} \right)^2. \tag{2.28}$$

The sum is estimated numerically as:

$$\sum_{i=0}^{\infty} \frac{1}{\alpha_i^2} \left(\frac{\sin\alpha_i \sinh\alpha_i}{\sin\alpha_i + \sinh\alpha_i} \right)^2 = \frac{1}{4}. \tag{2.29}$$

Finally the equipartition theorem is:

$$k_c\langle Z_c^2\rangle = \frac{4}{3}k_BT, \tag{2.30}$$

where $\langle Z_c^2\rangle$ is the cantilever deflection from mean position measured using the optical deflection method.

In figure 2.4, the measured thermal vibration of the cantilever (MLCT type B, Bruker) is presented. The value of $\langle Z_c^2\rangle$ is measured as $0.25 \pm 0.05 nm^2$. Using equation 2.30 the spring constant was determined as $k_c = 0.022 \pm 0.005 N/m$ [87].

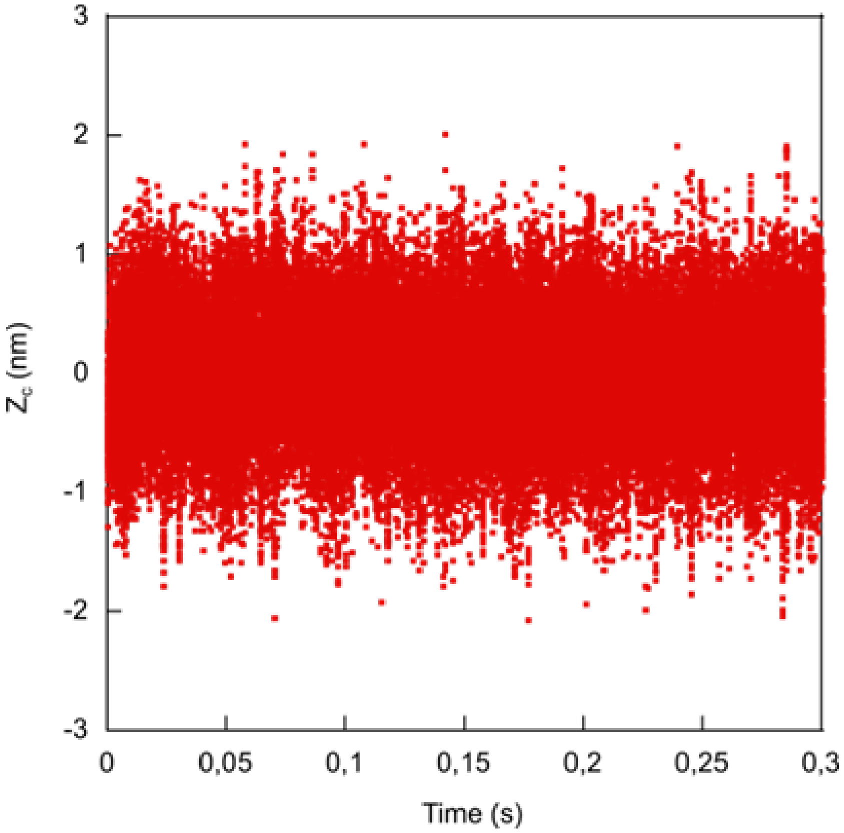

Figure 2.4: Temporal signal of the thermal vibration of the cantilever (MLCT type B, Bruker) is depicted with sampling frequency of $200kHz$. The spring constant of the cantilever was determined as $0.022 \pm 0.005N/m$.

Power spectral density method

The stiffness of the cantilever can be obtained using the power spectral density (PSD) of the cantilever thermal vibration. If $F_{(T)i}$ is the thermal force acting on the cantilever, then the cantilever motion for mode i is expressed as:

$$m^*\ddot{a}_i + \gamma_b\dot{a}_i + k_i a_i = F_{(T)i}, \tag{2.31}$$

where γ_b is the bulk damping. Using Fourier transformation, we have:

$$F_{(T)i}(\omega) = (-m^*\omega^2 + j\omega\gamma_b + k_i)a_i(\omega), \tag{2.32}$$

and

$$|a_i(\omega)|^2 = \frac{|F_{(T)i}(\omega)|^2/m^*}{(\omega_i^2 - \omega^2)^2 + (\omega\omega_i/Q_i)^2}. \tag{2.33}$$

The quality factor and thermal noise force for mode i are given by $Q_i = m^*\omega_i/\gamma_b$ and $|F_{(T)i}(\omega)|^2 = \gamma_b k_B T$, respectively [100]. The power spectral density is expressed as:

$$PSD(a_i, \omega) = \frac{2k_B T\omega_i/Q_i}{\pi m^* \Big((\omega_i^2 - \omega^2)^2 + (\omega\omega_i/Q_i)^2 \Big)}. \tag{2.34}$$

In an AFM experiment, the cantilever deflection is obtained using cantilever inclination (equation 2.17), So the equation of the PSD for mode i is given as:

$$PSD(Z_c, \omega_i) = \left[\frac{4\alpha_i^2}{9} \left(\frac{\sin\alpha_i \sinh\alpha_i}{\sin\alpha_i + \sinh\alpha_i} \right)^2 \frac{2k_B T/Q_i}{\pi k_i \omega_i \Big((1 - (\omega/\omega_i)^2)^2 + (\omega\omega_i/Q_i)^2 \Big)} \right], \tag{2.35}$$

and for the all modes it will be:

$$PSD(Z_c, \omega) = \sum_{i=1}^{\infty} \left[\frac{4\alpha_i^2}{9} \left(\frac{\sin\alpha_i \sinh\alpha_i}{\sin\alpha_i + \sinh\alpha_i} \right)^2 \frac{2k_B T/Q_i}{\pi k_i \omega_i \Big((1 - (\omega/\omega_i)^2)^2 + (\omega\omega_i/Q_i)^2 \Big)} \right]. \tag{2.36}$$

In order to present the power spectral density in the frequency domain, we use $PSD(Z_c, \omega) = 2\pi PSD(Z_c, f)$, then the equation 2.35 is expressed as:

$$PSD(Z_c, f_i) = \left[\frac{4\alpha_i^2}{9} \left(\frac{\sin\alpha_i \sinh\alpha_i}{\sin\alpha_i + \sinh\alpha_i} \right)^2 \frac{2k_B T/Q_i}{\pi k_i \omega_i \Big((1 - (f/f_i)^2)^2 + (f f_i/Q_i)^2 \Big)} \right]. \tag{2.37}$$

The power spectral density of the cantilever is the superposition of the contribution from all modes. As the frequency, spring constant and quality factor are independent parameters, equation 2.37 allows independent measurement of all these parameters from a single measurement of power spectral density of the cantilever [101].

In figure 2.5, the power spectral density for the cantilever motion is calculated from the measured temporal signal of the thermal vibration shown in figure 2.4. The first three modes of cantilever vibration are shown. The fitting curve for the first mode of the cantilever vibration is presented in figure 2.6. From the fitting, we obtained: $f_1 = 2948Hz$, $Q_1 = 1.5$ and $k_1 = 0.023 \pm 0.005N/m$. Likewise, for second mode we obtained: $f_2 = 25240Hz$, $Q_2 = 2.35$ and $k_2 = 0.87 \pm 0.02N/m$.

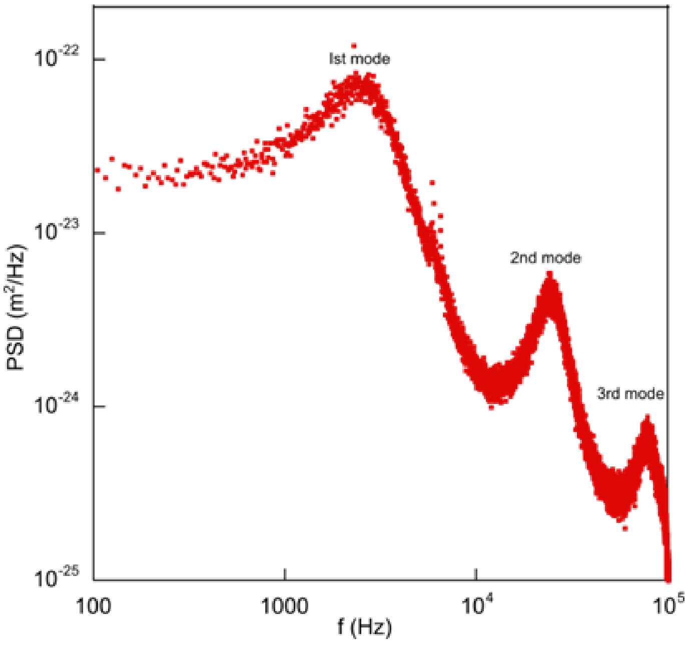

Figure 2.5: Power spectral density measured for the cantilever (MLCT type B, Bruker) at sampling frequency of $200kHz$.

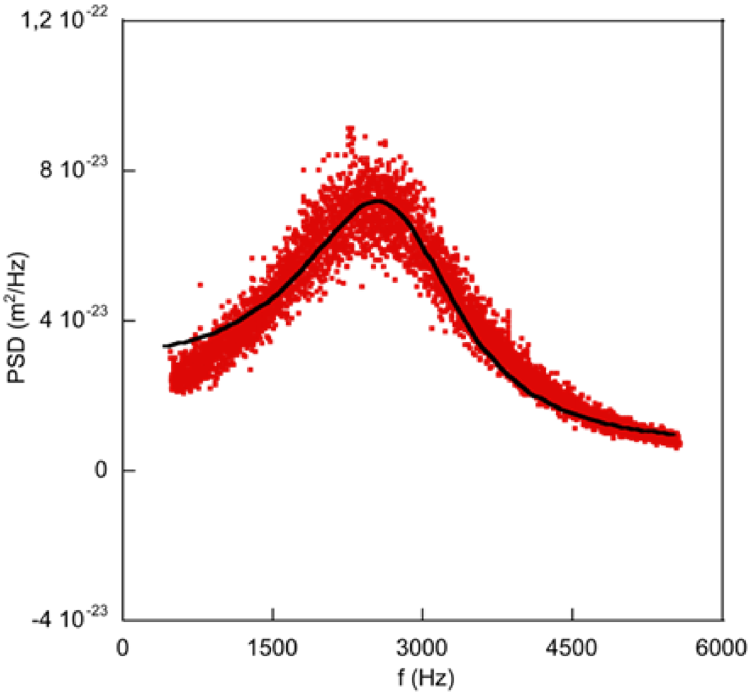

Figure 2.6: From figure 2.5 the first mode of the PSD curve is fitted using equation 2.37. The values extracted as: f_1=2948Hz, Q_1=1.5 and k_1=0.023±0.005 N/m.

2.2.5 Hydrodynamic Drag Method

All the techniques discussed above for the normal spring constant calibrations have their own set of advantages and limitations. But above all, these techniques are suitable for the determination of the stiffness of the bare cantilevers. Since, the colloidal probes are used in most of our experimental work, and none of those methods give accurate value for the stiffness of the colloidal probes. The presence of the particle (spheres of known geometry) at the free end of the cantilever changes the point of loading onto the cantilever, and as a result changes the stiffness.

The drainage force method is one of the simplest and most applicable methods for a colloidal probe calibration. The schematic is shown in figure 2.7. It is equally applicable for all types of cantilever provided that the radius of the colloidal probe and the viscosity η of the fluid are known. In this method, we measure the hydrodynamic force experienced by the sphere that is moving towards a hard substrate in a liquid [102].

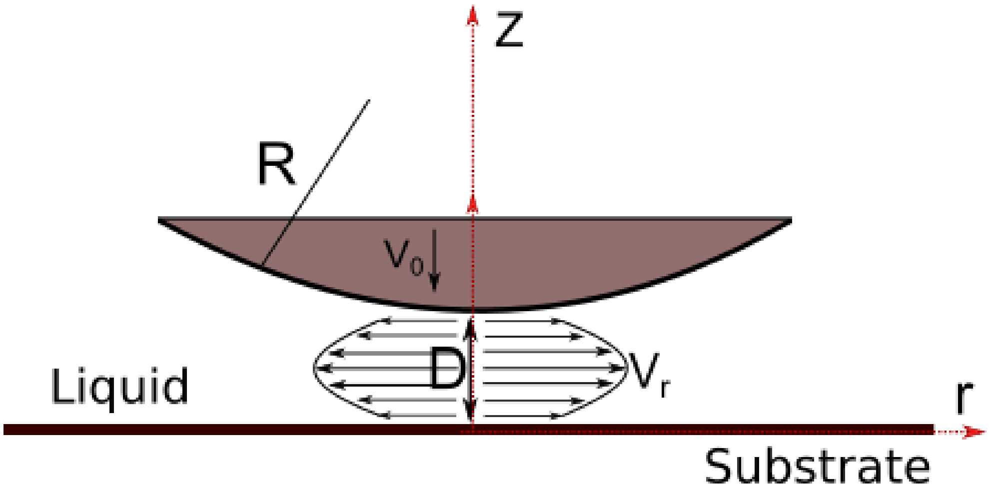

Figure 2.7: Schematic for a colloidal probe approaches a hard substrate at velocity V_0 in a viscous fluid.

For small Reynolds number and for very small gap i.e. $D << \sqrt{2RD}$, the flow is described using the Navies-Stokes and the continuity equation in the framework of lubrication approximation as:

$$\eta \frac{\partial^2 V_r}{\partial z^2} = -\frac{\partial P}{\partial r}, \tag{2.38a}$$

$$\frac{\partial P}{\partial z} = 0. \tag{2.38b}$$

$$\frac{\partial V_z}{\partial z} + \frac{1}{r}\frac{\partial}{\partial r}(rV_r) = 0, \tag{2.38c}$$

Where V_r is the radial component of velocity, V_z is the vertical component of velocity and P is liquid hydrodynamic pressure. If the instantaneous distance between the sphere and the substrate is D and the sphere is approaching the substrate, which is placed at $z = 0$, with velocity of V_0, then the parabolic approximation gives the thickness of the confined liquid as $h(r) = D + r^2/2R$.

Integrating equation 2.38a, we have:

$$V_r = \frac{1}{\eta}\left(\frac{\partial P}{\partial r}\frac{z^2}{2} + a_0 z + b_0\right), \tag{2.39}$$

Applying initial boundary conditions of no slip at $z = 0$ and $z = h$, we get:

$$V_r = \frac{1}{2\eta}\frac{\partial P}{\partial r} z(z-h). \tag{2.40}$$

Integrating equation 2.38b, after inserting V_r from equation 2.40 and applying initial boundary conditions for the velocity at $z = 0$ and $z = h$. We get:

$$V_z(z=h) = V_0 = \frac{1}{12\eta r}\frac{\partial}{\partial r}\left(rh^3\frac{\partial P}{\partial r}\right), \tag{2.41}$$

and from 2.41 we have:

$$\frac{\partial P}{\partial r} = \frac{6\eta r V_0}{h^3}. \tag{2.42}$$

The hydrodynamic force F_h between the sphere and the substrate is calculated as:

$$F_h = \int_0^\infty P(r) 2\pi r dr, \tag{2.43}$$

Integrating equation 2.42 and then equation 2.43. we obtain [103]:

$$F_h = 6\pi\eta V_0 \frac{R^2}{D}. \tag{2.44}$$

This equation is valid for the distances that satisfy the lubrication approximation ($D << \sqrt{2RD}$). For the general case, Brenner [104] has formulated an equation for hydrodynamic drag force acting on a sphere that moves toward a solid plane in a fluid, as:

$$F = 6\pi\eta R V_0 \lambda, \tag{2.45}$$

where λ is the correction to the stoke's law and given as:

$$\lambda = \frac{4}{3}\sinh\alpha \sum_{n=1}^{\infty} \frac{n(n+1)}{(2n-1)(2n+3)}\left[\frac{2\sinh(2n+1)\alpha + (2n+1)\sinh 2\alpha}{4\sinh^2(n+0.5)\alpha - (2n+1)\sinh^2\alpha}\right], \tag{2.46}$$

where $\alpha = \cosh^{-1}(R/D)$ is the ratio of sphere radius to the sphere-sample separation. For a distance too large than the sphere radius $\lambda \sim 1$; equation 2.45 becomes:

$$F = 6\pi\eta R V_0. \tag{2.47}$$

For the case of small distance where the sphere radius is larger than the distance, the $\lambda \sim R/D$,

$$F = 6\pi\eta R V_0 \frac{R}{D}. \tag{2.48}$$

This relation is used to calculate the drag force on the sphere attached to an AFM cantilever. In quasi-static equilibrium condition the hydrodynamic force will induce the static deflection in the colloidal probe, and the measured force $F = k_c Z_c$ relates to the equation 2.48 as:

$$6\pi\eta V_0 \frac{R^2}{D} = k_c Z_c, \tag{2.49}$$

or

$$\frac{Z_c}{V_0} = \frac{6\pi\eta R^2}{k_c}\frac{1}{D}. \tag{2.50}$$

Where k_c is the spring constant of the cantilever. First we convert the measured deflection signal from volt to nanometer (see section 2.2) and than we obtain the spring constant in N/m using the equation 2.50 as discribed below.

We present here the calibration of the cantilever, which is used chapter 4, where a polystyrene microsphere of radius $R = 20 \pm 0.5\mu m$ is glued to a rectangular cantilever (NSG-11/tipless) to obtain a colloidal probe. A freshly cleaved mica sheet, which was used as substrate, fixed on the piezo stage that controls the approaching velocity. A few drops of solution (with viscosity measured as $\eta = 49 \pm 1mPa.s$) is poured in to immerse the colloidal probe close to the substrate. We first calibrated the photodiode sensitivity on a hard silicon substrate at low velocity of $400nm/s$ to obtaine the sensitivity $\beta = 0.037V/nm$ (that allows to convert the vertical deflection in volts to defelection in nm). Then the deflection signals were recorded to obtain the force in nN versus distance for lager velocity. The relative velocity was obtained by doing time derivative of the distance [105].

The deflection of the cantilever Z_c and the velocity for one of the measurements are shown in figure 2.8. As we reduce the gap between the sphere and the substrate, the cantilever starts to deflects away under the influence of the hydrodynamic force. The relative velocity is the difference between the velocity imposed by the piezo displacement and the velocity at which the cantilever deflect away. At the proximity of the substrate, the deflection of the cantilever increases and the relative velocity decreases.

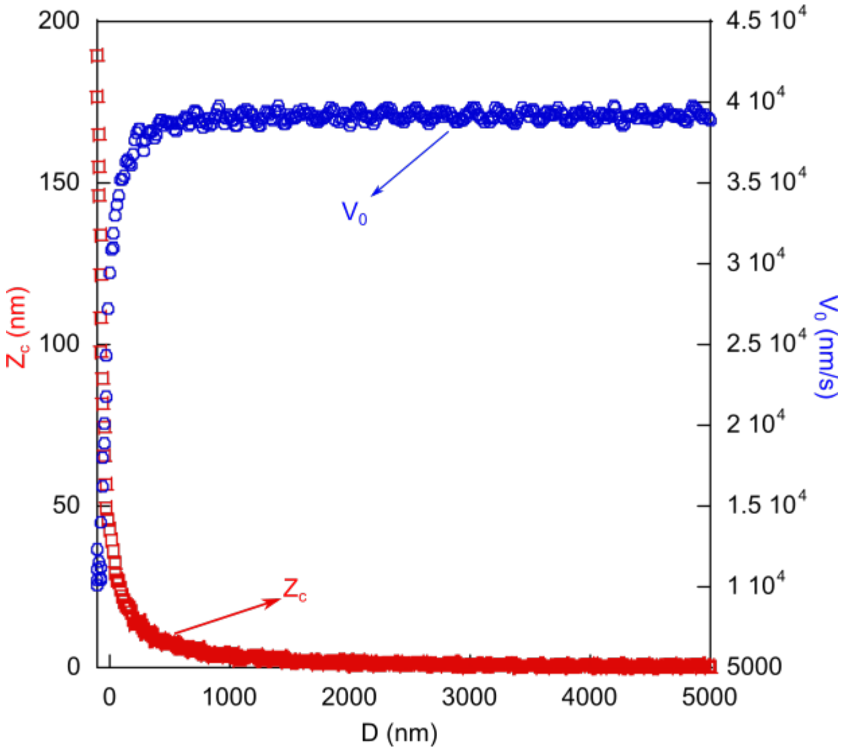

Figure 2.8: For the cantilever used in chapter 4, the cantilever deflection (red square) and relative velocity (blue circle) are shown as function of tip-sample separation.

The measured drag force is the sum of the drag force on the cantilever beam and the drag on the sphere. But when the distance between the sphere and the substrate is smaller than the sphere radius, then drag force is dominated by the drag on the sphere, so we neglect the drag on the cantilever.

In the above relation (equation 2.50) the only unknown parameter is the spring constant of the cantilever. In figure 2.9, we present the ratio of the cantilever deflection to the approaching velocity versus the distance. We obtained the spring constant of the cantilever as $k_c = 3.9 \pm 0.1 N/m$, by fitting the curve using equation 2.50. It is observed that very close to the substrate, the validity of equation 2.50 may be affected due to the contribution of the partial boundary slip. Additionally, the roughness of the colloidal probe and electrostatic force also affect the accuracy of the measurements at smaller separation. To avoid these aspects, we have used the data for the distance larger than $200 nm$.

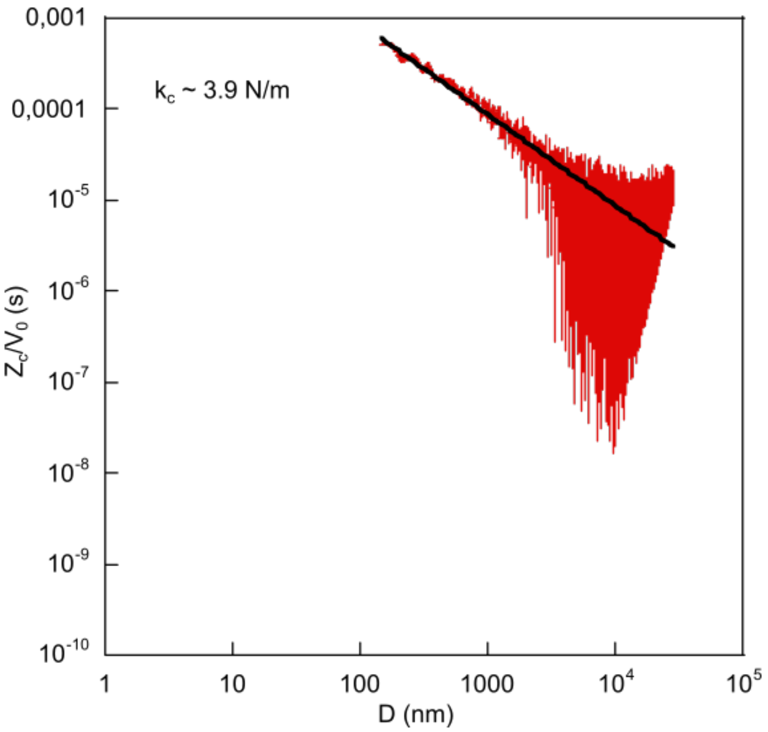

Figure 2.9: For the calibration of the cantilever used in chapter 4, we present the ratio of the the cantilever deflection to the approaching velocity versus the distance. The solid black line is the fitting using equation 2.50, which gives the spring constant of the cantilever as $k_c = 3.9 \pm 0.1 N/m$.

Similarly, the cantilever used in chapter 3 was calibrated using this drainage method. The ratio of the approaching velocity to the cantilever deflection versus the distance are presented in figure 2.10. The fitting using equation 2.50 gives the force constant as $k_c = 0.25 \pm 0.2 N/m$.

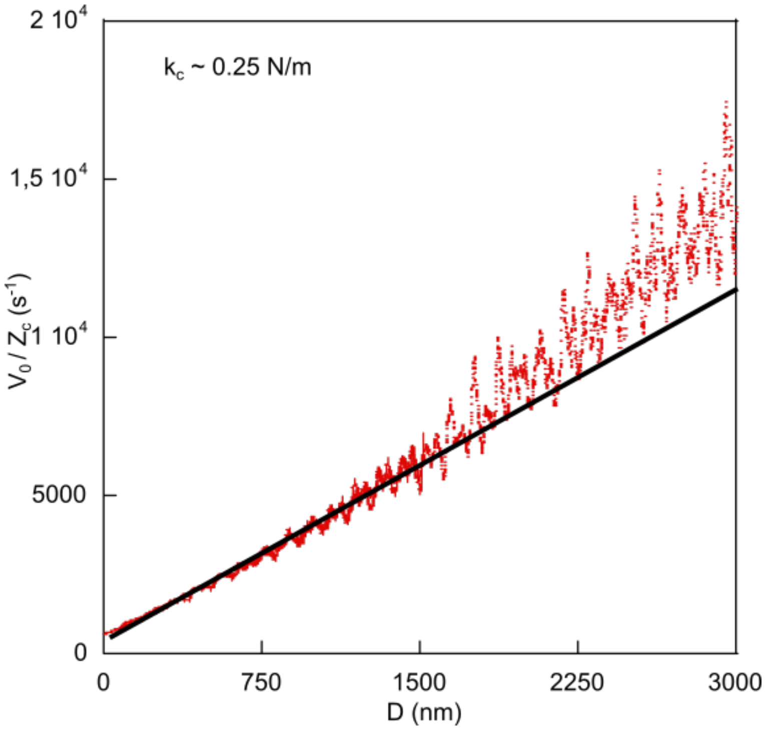

Figure 2.10: For the calibration of the cantilever used in chapter 3, we present the ratio of the approaching velocity to the cantilever deflection versus the distance. The spring constant of the cantilever is obtained by fitting the data in linear region (dark sold line). From the fitting we obtained $k_c = 0.25 \pm 0.2 N/m$.

2.3 Lateral Force Calibration

Lateral force calibration is more challenging than the normal force calibration because of the difficulty in determining the lateral deflection sensitivity. Additionally, the lateral spring constant is much larger than the normal spring constant of the cantilever [78, 79]. Over the last two decades, several methods are developed for the lateral force calibration. Keeping in view the wide acceptability and usage of LFM as a technique, the search for an established and precise lateral calibration technique is inevitable [106]. Once the lateral calibration factor is obtained, then the multiplication with the change in lateral signal ΔV_l gives the lateral force F_l :

$$F_l = \alpha \Delta V_l, \tag{2.51}$$

with α being lateral conversion factor [16].

In this section we will discuss different calibration methods in analogy to the techniques used for the normal force calibration.

2.3.1 Geometry of Cantilever

The torsion constant is a geometrical property of the rectangular beam, which gives the relation between the angle of twist θ and applied torque τ. This constant along with the geometry of the beam gives the torsional stiffness k_ϕ as:

$$k_\phi = \frac{\tau}{\theta} = \frac{GJ}{l}, \tag{2.52}$$

where k_ϕ is the torsional spring constant or torque constant in newton-meter per radian, G is the shear modulus and J is torsion constant. For a rectangular bar, axis passing through the base of the bar, the torsion constant will be $J = we^3/3$. Applying this to the case of a rectangular cantilever, the torsional spring constant k_ϕ for an AFM cantilever is described as:

$$k_\phi = \frac{Ge^3w}{3l}. \tag{2.53}$$

If the rectangular cantilever has a tip or for the colloidal probe, the torsional stiffness relates to the lateral stiffness k_l by the following relation:

$$k_l = \frac{k_\phi}{(h+e/2)^2}, \tag{2.54}$$

with h is the torsional moment of arm, it corresponds to the distance from the point of action of the lateral force (that acts on the end of tip) to the twisting axis of the cantilever. In the case of a colloidal probe, its the colloidal diameter plus the neutral axis of the cantilever that gives moment of arm.

The lateral spring constant is related to the normal spring constant by:

$$\frac{k_c}{k_l} = \frac{3E}{4G}(\frac{h}{l})^2. \tag{2.55}$$

The relation between the Young modulus and the shear modulus is given as: $E = 2(1+v)G$. For an isotropic materials with positive Poisson's ratio the Young modulus of the cantilever is always greater than the shear modulus [107]. For a rectangular cantilever having a tip of height h of a few micrometers, the square of ratio between h and l is smaller, which in turn gives smaller value for the ratio between the normal and lateral spring constant [16]. Whereas, in case of a colloidal probe with a large sphere, the torsional moment of arm h ($h = 2R$) becomes large and thus the ratio between the two spring constant is also expected to be large.

2.3.2 Torsional Sader Method

This method is derived in an analogy to the normal Sader method. Considering the case of a rectangular cantilever where the length of the cantilever is larger than its width and the width is greater than the thickness of the cantilever, the torsional spring constant k_ϕ is given by [83]:

$$k_\phi = \frac{1}{3\pi^2}\rho w^3 e l \omega_{t(vac)}^2, \tag{2.56}$$

where ρ is the cantilever density and $\omega_{t(vac)}$ is the radial resonant frequency for torsional vibrations in vaccum. This equation 2.56 is of limited use because of difficulties in measuring the cantilever geometry. In addition, the assumption for the cantilever density being homogeneous is not always valid [86]. Thus for the case, when the quality factor of the cantilever's torsional resonance peak is greater than one, $\omega_{t(vac)}$ is related to the torsional resonant frequency in fluid ω_t by the following relation:

$$\omega_{t(vac)} = \omega_t\left(1 + \frac{3\pi\rho_f w}{2\rho h}\Gamma_r^t(\omega_t)\right)^{1/2}, \tag{2.57}$$

and also we have [108]:

$$\rho e = \frac{3\pi\rho_f w}{2}\left[Q_t\Gamma_i^t(\omega_t) - \Gamma_r^t(\omega_t)\right], \tag{2.58}$$

where ρ_f is the fluid density, Q_t is quality factor of torsional resonance peak, $\Gamma_i^t(\omega_t)$ and $\Gamma_r^t(\omega_t)$ are the imaginary and the real part of hydrodynamic function, respectively. By inserting equation 2.57 and 2.58 in equation 2.56, we obtain the required expression for the torsional spring constant at the end of the cantilever as [83, 108]:

$$k_\phi = 0.1592\rho_f w^4 l Q_t \omega_t^2 \Gamma_i^t(\omega_t). \tag{2.59}$$

This equation is only valid when $Q_t >> 1$.

2.3.3 Torsional Cleveland Method

The normal Cleveland method (added mass method) is extended for the calibration of torsional spring constant of an arbitrary geometry. The torsional spring constant in relation to the radial resonanant frequency ω_t is given as,

$$\omega_t^2 = \frac{k_\phi}{J_e}, \tag{2.60}$$

where J_e is the effective mass moment of inertia of the cantilever. For a colloidal probe, equation 2.60 is modified as:

$$\omega_t^2 = \frac{k_\phi}{J_e + J}, \tag{2.61}$$

where J is the mass moment of inertia for the added mass, which is assessed using Parallel axis theorem provided that the diameter of the added spherical mass is greater than the thickness of the cantilever [109]:

$$J = \frac{7}{5}M_s R^2, \tag{2.62}$$

Where M_s and R are the mass and radius of the added spherical mass, respectively. Inserting equation 2.62 in equation 2.61, we have:

$$\omega_t^2 = \frac{k_\phi}{7/5 M_s R^2 + J_e}, \tag{2.63}$$

The above relation is rearranged by replacing the mass with the density ρ and radius of the sphere.

$$\frac{28\pi\rho R^5}{15} = \frac{k_\phi}{\omega_t^2} - J_e. \tag{2.64}$$

Following the torsional resonant frequency measurements for different spherical masses attached to the end of cantilever, the linear plot of $\frac{28\pi\rho R^5}{15}$ against ω_t^{-2} gives the torsional spring constant k_ϕ of the cantilever [86].

2.3.4 Thermal Noise Method

In an analogy of section 2.2.4, this method can be used for the lateral (torsional angle measurement). The equivalent equation for a sphere executing thermal torsional vibration is given as:

$$\frac{1}{2}K_B T = \frac{1}{2}k_\phi\langle\phi^2\rangle, \tag{2.65}$$

where $\langle \phi^2 \rangle$ is in radians and depicts the mean square angular displacement of the cantilever. The torsional angle of the cantilever relates to the lateral voltage change V_y as:

$$\phi = sV_y, \tag{2.66}$$

where s is the angular inverse optical lever sensitivity and measured in radian per volts [110].

2.3.5 Hydrodynamic Drag Method

The lateral force calibration, such as for the normal force calibration, is generally comprises of two steps: measurements of optical lateral sensitivity (nm/V) and determination of lateral spring constant of cantilever $(nN/\mu m)$. However, an one-step lateral force calibration method is used in this work. In this method, the lateral force/torque conversion factor k_t^l in $(\mu N.\mu m/V)$ is measured in a viscous fluid by applying the lateral forces of known magnitude to the AFM colloidal probe, which is placed close to the substrate. The one-step calibration method has an additional advantage of doing non-contact measurements that minimize the risk of damage to the probe.

In this work, we opted for in situ hydrodynamic method for lateral calibration of our cantilevers. In this method, the probe is placed close to the substrate immersed in a viscous liquid. The lateral motion of the substrate generates a creeping Couette flow, which induces a twist in the AFM colloidal probe by exerting viscous drag force and torque on the probe. The working principle and experimental set up are illustrated in figure 2.11. The colloidal probe is fixed in the liquid cell and placed close to a freshly cleaved mica substrate (that is fixed on piezo stage) in a solution having viscosity of $\eta = 49mPa.s$. In order to induce the lateral motion of the substrate, the frequency and the voltage of the piezo are set to the desired values using a function generator. It is noteworthy that the distances h_o between the sphere and the substrate must satisfying the condition $\frac{h_o}{R} < 1$. We repeated the experiment for different distances and different frequencies [111].

The direction of shear U, force and torque produced are shown in figure 2.11. The force F and the torque τ exerted by the fluid onto the sphere are given as:

$$F = 6\pi\eta RUf^*, \tag{2.67}$$

$$\tau = 8\pi\eta RU\tau^*, \tag{2.68}$$

where f^* and τ^* are the normalized scaler force and torque, respectively. These normalized quantities can be positive or negative depending only upon the ratio h_o/R, and are given by the asymptotic formula of Goldmen *et al* as:

$$f^* = c_1 \ln \frac{h_o}{R} + c_2, \tag{2.69}$$

$$\tau^* = c_3 \ln \frac{h_o}{R} + c_4, \tag{2.70}$$

where the interpolation coefficients are: $c_1 = -8/15$, $c_2 = 0.9588$, $c_3 = 1/10$ and $c_4 = 0.1895$ [112, 113].

It is observed that the lateral voltage change V_y for a bare cantilever is negligible as compared to the colloidal probe under the same experimental conditions. Therefore,

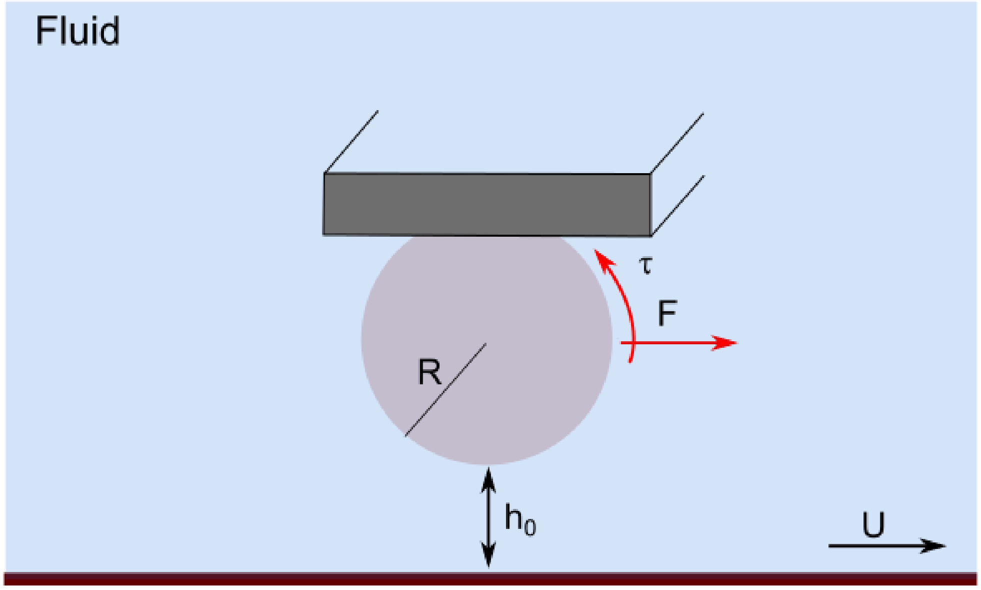

Figure 2.11: Schematic illustration for hydrodynamic lateral force calibration. An AFM colloidal probe placed close a substrate in a viscous liquid having lateral velocity U. The direction of viscos drag force and torque are shown that are result of the creeping couette flow.

it is concluded that the twist in the cantilever is mostly due to the drag force and the torque acting on the sphere. Additionally, it is also assume that the viscous loading on the colloidal probe is applied to the center of the sphere. However, for very small distance the hydrodynamic force center might not be identical to the geometrical center of the colloidal probe, because the fluid motion around the sphere close to the substrate is not exactly symmetric. It was proposed that the offset in the centers needs to be considered if $h_o/R < 0.05$ [114]. This ratio was always greater than 0.25 in our experiments, so we did not consider the center offset in our measurements.

The total torque experienced by the probe is $\tau_{tot} = RF + \tau$, and using equations 2.67, 2.68, 2.69 and 2.70 we write it as:

$$\tau_{tot} = 6\pi\eta R^2 U \left[-\frac{8}{15} \ln \frac{h_o}{R} + 0.9588 + \frac{8}{60} \ln \frac{h_o}{R} + \frac{8}{6} 0.1895 \right] \tag{2.71}$$

Using the above relation, we have calculated the total torque applied to the cantilever for a given velocity and distance.

After placing the probe close to the substrate, the lateral motion of the substrate is tuned (from low to high) by varying the amplitude of the lateral oscillation at given frequency and distance. For the given piezo input values, the lateral displacement of the piezo is recorded to obtain the lateral velocity. Using the sine wave equation, the amplitude of the lateral velocity is calculated by fitting the velocity-time plot. Figure 2.12 shows an example of the measurement.

The torsion of the cantilever is measured by acquiring the lateral deflection of the cantilever. This enables us to know the amplitude of the lateral voltage change V_y produced as a result of twist in the cantilever. The measured lateral voltage change V_y versus time at different velocities and distances is shown in figure 2.13. An increase in the amplitude of the lateral deflection is observed: when the substrate is moved at a higher velocity (figure 2.13(a) and also when the AFM probe is closer to the substrate (figure 2.13(b)). Thus, we conclude that the torsion of the cantilever increases with increasing velocity and also with the decreasing sphere-substrate distance.

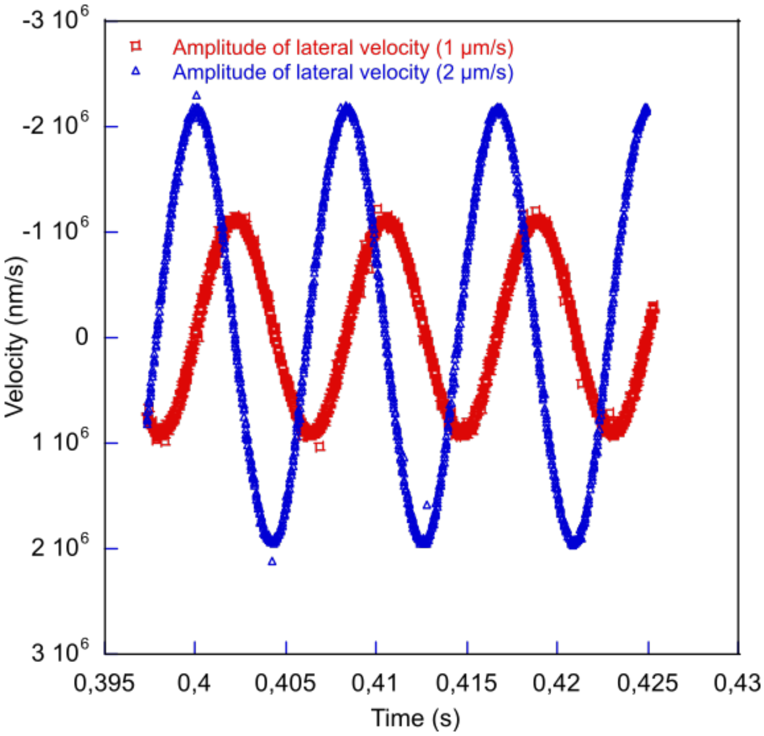

Figure 2.12: Examples of lateral velocity as function of time at different scanning speed.

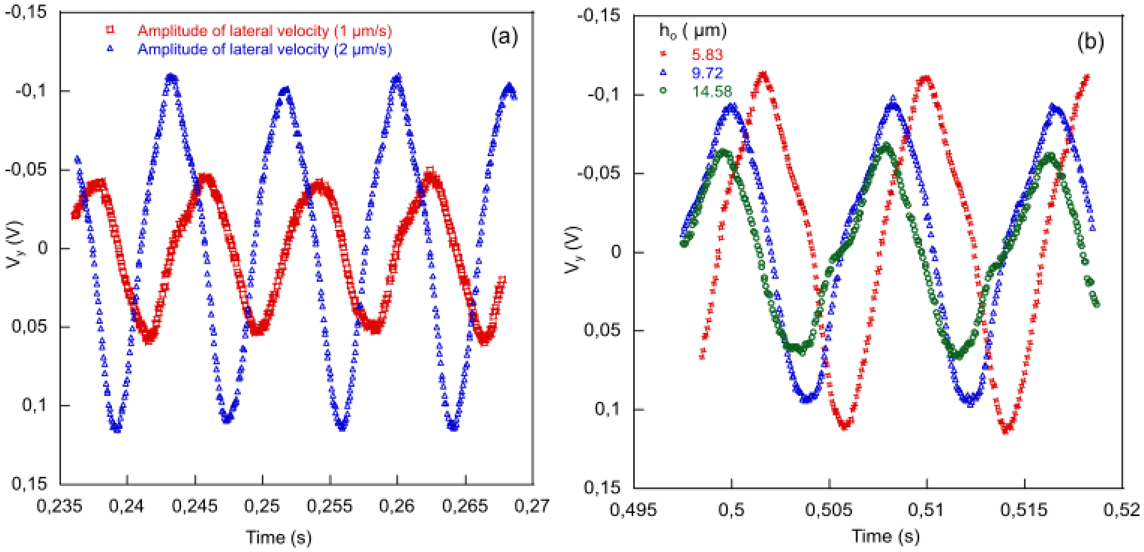

Figure 2.13: The torsion of the cantilever V_y as a function of time(a) the torsion V_y is plotted for different lateral scanning velocities but at same distance of 5.83μ m. (b)the torsion V_y is plotted for same scanning speed amplitude of 2 μm/s for different distances.

The tip-substrate separation is controlled using step motor in small steps movement of $1\mu m$. Once the velocity, distance and amplitude of lateral voltage are measured, the total torque produced in the cantilever is obtained using equation 2.71. The plot of the total torque produced versus the lateral voltage change shows a linear increase, as shown in figure 2.14. The linear fit of the plot gives the lateral torque conversion factor k_t^l.

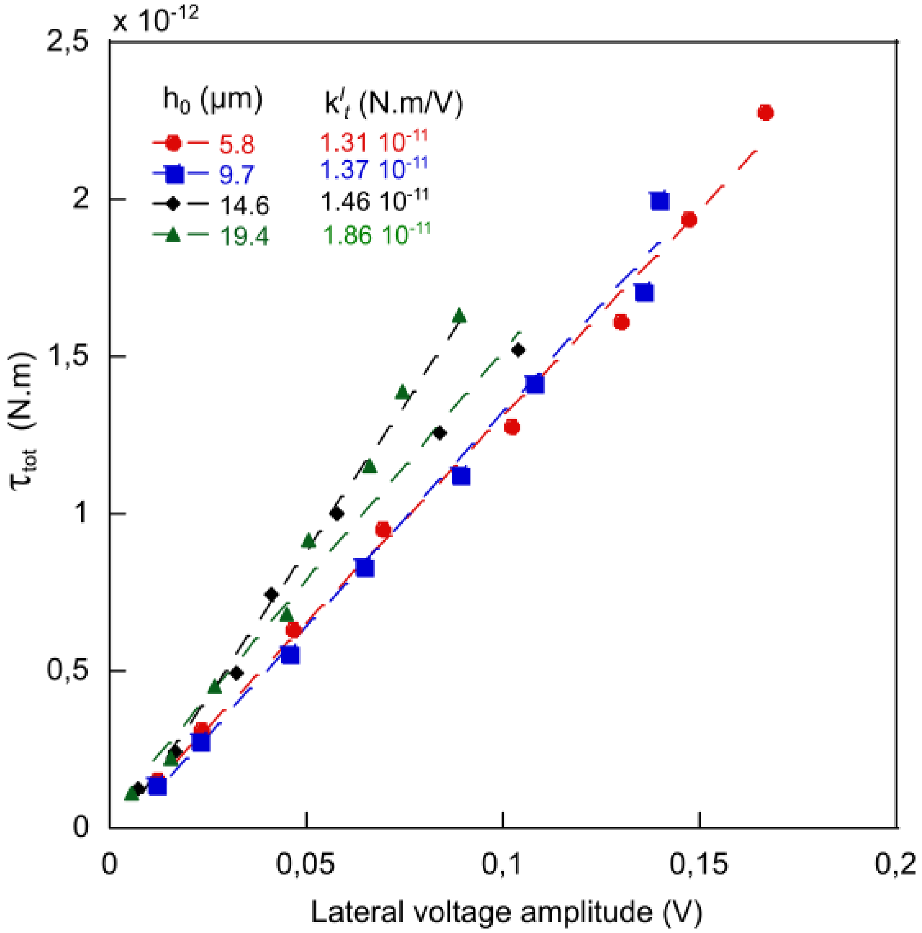

Figure 2.14: Hydrodynamic calibration of the conversion factor $k_t^l(N.m/V)$ in liquid: Applied torque versus the lateral deflection. The measurement was performed in solutions of (water + glycerol solution with viscosity 49cSt) and at working frequency of 120Hz. The dashed (fitting) line gives lateral force conversion factor for all the distances. We have choosen $k_t^l = 1.31 \times 10^{-11} N.m/V$ from small tip-substrate separation.

The calibrated lateral force conversion factor (see figure 2.14) at different distances gives slightly different values. One of the reasons for the deviation of k_t^l is the error in the determination of the tip-substrate separation. The uncertainty in the measurement of h_0 is possibly contributed by two factors: first, the sphere did not seem to return to the same position after each traverse during the determination of h_o and it is inevitable because of nonlinearity and creep of the motor [111]; second, we have ignored the cantilever drag, which more likely modifies the flow around the colloidal probe. The relative contribution of this effect on the torque becomes smaller as the tip-substrate separation decreases, but reducing the distance to too low value induces an error in the evaluation of the torque. We have found that $h_o \approx 6\mu m$ appears to be a good compromise that gave a conversion factor as $k_t^l = 1.31 \times 10^{-11} N.m/V$.

2.4 Conclusion

In this chapter, we have presented different calibration techniques and highlighted the practical limits in each method. It is concluded that among all the methods, the hydrodynamic drag method gave an accurate value for the spring constant of the colloidal probe. The practical implementation of other methods has its own set of constraints. For instance, in the thermal noise method, the attachment of the probe to the cantilever tip induces a torque due to motion in x-axis. This motion contributes to the thermal vibration of the probe in z-axis and resulting in a false estimation of the spring constant of the cantilever. The Sader method was developed specifically for the bare cantilevers. In added mass method, the complexities and difficulties in the measurement of the size and position of the sphere on the cantilever add to its disadvantages. The uncertainty and error in the calibration of the colloidal probes using the geometry of the cantilever method are caused by the variation in length, difficulty in thickness measurement and inhomogeneous density of the cantilever.

The hydrodynamic force method is used to calibrate the lateral and vertical force. The hydrodynamic force will be experienced by a colloidal probe in a viscous fluid. For the case of vertical spring constant calibration, the hydrodynamic force is measured by recording the deflection of the colloidal probe. The drainage method is adopted because of its simplicity and higher accuracy compared to other methods. In case of the lateral force calibration, the hydrodynamic drag method is used to obtain the lateral force conversion factor. Here a laterally moving substrate generates creeping Couette flow, whicht induces a torsion of the colloidal probe. From the plot of the applied torque to the cantilever versus the lateral deflection amplitude (volts), we have computed the lateral force conversion factor (by the linear fit of the plotted data).

Chapter 3

Viscoelastic Properties of PDMS

Contents

3.1 Introduction **44**
3.2 Experimental Details **45**
  3.2.1 PDMS sample preparation 45
  3.2.2 Dynamic AFM Method 46
3.3 Analytical Solution for Viscoelastic Response: A Simple Model **52**
3.4 Hydrodynamic Model for Viscoelastic Response **54**
3.5 Contact Mechanics **59**
3.6 Conclusion and Perspective **60**

3.1 Introduction

Mechanical properties of thin soft solids are of great interest for many emerging applications including photonics, microelectronics, and biosensors [115]. The mechanical traits of thin surfaces differ significantly from those of the bulk materials because of theire reduced dimensions, large surface-to-volume ratio and unique microstructure. The qualitative difference between the thin soft solids and stiff materials is observed in elastic instabilities during adhesion [116, 117] and Schallamach waves in friction [41, 118]. The mechanical features such as the hardness, adhesion, elastic modulus and yield strength are critical for the comprehensive investigation of a thin film [119].

Methods, such as the tensile testing, bending tests and indentations are used for the mechanical characterizations of the materials. For a thin film, AFM is one of the tools that allows excellent force sensitivity, surface imaging and nanomechanical characterization measurements. AFM probe of known shape is used as nano-indenter to measure the variation of the cantilever deflection versus the indentation in the sample under applied normal compression [16, 18, 120–122]. Using an AFM, it is possible to perform nanomechanical characterization of materials with modulus in range of kPa to GPa [34, 123]. However, there are limitations in the measurement of elastic moduli for the soft and biological samples using a direct contact method. There is often a strong adhesion observed between the sample and the probe. It is not only difficult to account for the adhesion, but the contact area in the adhesive contact is also difficult to measure [124, 125]. In addition, the sample damage and the probe contamination may also occur during these measurements, especially for the biological samples [126].

Contactless measurement is an alternative to the direct contact methods. Here, the nano-hydrodynamic interaction between a probing sphere and a soft sample in liquid environment makes it possible to assess the mechanical properties of the sample surface [22, 23]. At a small gap between a vibrating sphere and the substrate, the generated hydrodynamic pressure becomes large enough to induce deformation of the substrate, which leads to the elastohydrodynamic (EHD) coupling. Over the years, various tools and methods have been developed to probe the mechanical properties of the soft interfaces. Using the dynamic surface force apparatus, team of Elisabeth Charlaix has performed mechanical characterization of surfaces of various rigidity ranging from soft surface to the hard surface like glass at low frequencies (i.e. less than $100Hz$) [19, 21, 127]. Guan *et al* have used vibrating nano-needle glued to the AFM cantilever to probe the viscoelastic properties of the PDMS surfaces [128] and living cells [129]. In these measurements, they fixed the probed frequency to a single value given by the resonance frequency of the cantilever. Nonetheless, the technique based on the vibrating the probe close to a substrate inspired to probe the rheological properties at different frequencies.

Usually, the frequency dependent rheology of soft solid is probed at macroscale with conventional shear rheometers where the sample is fixed between the two rotating parallel plates [30–32]. Imposing a rotating displacement on one plate and measurement of the applied torque on the other one, allows to extract the complex shear modulus of the system. This method requires a perfect contact between the sample and the plates of the rheometer. The dynamic colloidal AFM method is a good candidate to probe the EHD interaction at nanoscale for different vibration frequencies without such constraint. It allows working in large frequency range from $20Hz$ up to few kHz, depending on the resonance frequency of the cantilever [33–35].

In this work, we performed viscoelasticity measurements of the soft and thin polymeric films using the dynamic colloidal AFM technique. The measurements for the mechanical response of a thin soft solid (PDMS) are presented as a function of the separation between the probe and the substrate. From the mechanical response, the loss and storage moduli of the soft solid are obtained. The measured viscoelasticity of the thin PDMS sample for different frequencies are in good agreement with the Chasset-Thirion model for the frequency response of a soft gel. Our measurements demonstrate that the contactless colloidal AFM technique is a powerful tool for probing the soft interface over the wide range of excitation frequencies.

3.2 Experimental Details

3.2.1 PDMS sample preparation

PDMS samples were prepared on cover-slips (with a size of 24 $mm\times$ 24 mm) using the spin-coating method. The uncross-linked PDMS and the curing agent (Sylgard 184, Dow Corning) were mixed in a weight ratio of (71:1) and then degassed in a vacuum. A droplet of solution spin-coated on the cover-slip for a minute to obtain the PDMS sample with a thickness of $26 \pm 3\mu m$. For an efficient cross-linking these coated substrates are cured at 50° C for 24 hours in an oven.

3.2.2 Dynamic AFM Method

The experiments were performed using an AFM (Bioscope II, Bruker), which is equipped with a liquid cell (DTFML-DDHE) that allows working in a liquid environment. The schematic for the experimental setup is shown in figure 3.1. The colloidal probe was obtained by gluing a borosilicate sphere of radius R=55±1μm at the tip of a silicon nitride cantilever (SNL-10, Bruker, USA). The sample was fixed on the piezo stage, which was used to control the distance between the sphere and the sample by imposing the vertical displacement to the substrate at low velocity. Dodecane, having viscosity of η=1.34 mPa.s, was used as the working liquid in the experiment. The stiffness of the cantilever $k_c = 0.25 \pm 0.2 N/m$ was determined using the drainage method (see section 2.2.5).

We have used signal access module (Nanoscope III, Bruker) that allows to control the input signal of the AFM (driving frequency and amplitude) and also gives access to the measured output signal of the AFM (deflection, lateral deflection etc.). The DC component of the cantilever deflection was recorded and the AC component was used as an input to lock-in amplifier (Signal Recovery, 7280 DSP) to measure the amplitude A and the phase φ of the cantilever oscillation.

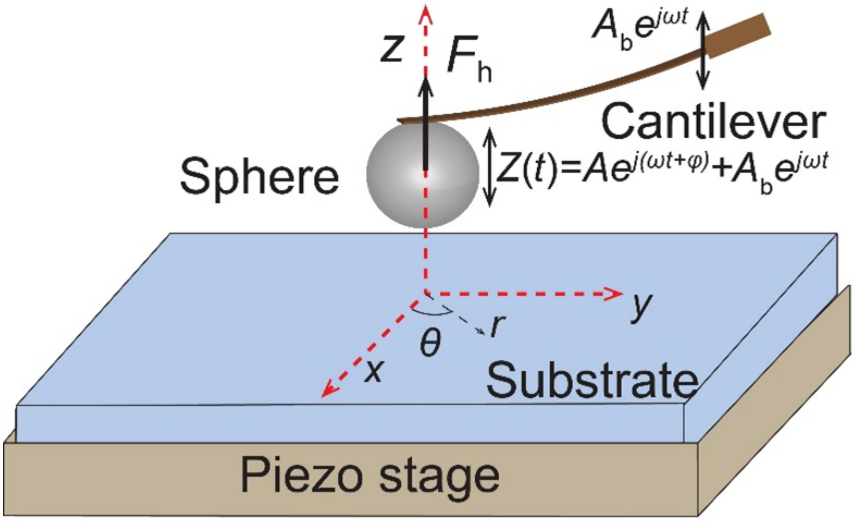

Figure 3.1: The schematic for the experimental setup based on dynamic collidal AFM method is shown. A colloidal probe is vibrating close to the substrate in a viscous liquid. The cantilever motion is the sum of the deflection and the base oscillation.

The base of the cantilever was oscillated using the piezo with driving amplitude of A_b and frequency ω. Meanwhile, the substrate on multi-axis piezo stage is monitored to approach the oscillating probe. The amplitude A and the phase φ of the cantilever deflection were recorded as a function of the piezo displacement. The deflection of the cantilever was also recorded and used to determine the tip-sample separation. It is observed that in a liquid environment (i.e. for low quality factors), the amplitude of the cantilever will not be very large compare to the base displacement. Thus, the cantilever motion will be the sum of the base and the deflection oscillation of the cantilever [130–132].

If the instantaneous deflection of the cantilever is $X = Ae^{j(\omega t+\varphi)}$ and the base displacement of the cantilever is given by $Z_b = A_b e^{j\omega t}$, then the total displacement of cantilever is given as:

$$Z = Ae^{j(\omega t+\varphi)} + A_b e^{j\omega t}. \tag{3.1}$$

The motion of the cantilever is given by the harmonic oscillator model as:

$$m^*\ddot{Z} + \gamma_b \dot{Z} + k_c Z = F_d + F_h. \tag{3.2}$$

Where m^* and k_c are the effective mass and spring constant the cantilever, respectively. While, F_d is the driving force in liquid and F_h is the force corresponding to the interaction between the tip and the sample. For the oscillations with an amplitude smaller than the interaction length; the Interaction force is linearized and given as $F_h = -(k_{int}Z + \gamma_{int}\dot{Z})$. This expression comprises of two terms: a conservative one $(k_{int}Z)$ and dissipative one $(\gamma_{int}\dot{Z})$. Here γ_{int} and k_{int} are the interaction damping and stiffness, respectively. The equation 3.2 is rearranged as:

$$m^*\ddot{Z} + \gamma_b \dot{Z} + k_c Z = F_d - k_{int} - \gamma_{int}\dot{Z}. \tag{3.3}$$

The driving force is induced by the displacement of the cantilever base and calculated as [132–134] :

$$F_d = (m^*\omega^2 - j\omega\gamma_b)\beta A_d e^{j\omega t}, \tag{3.4}$$

where $\beta \approx 1.565$ [131].

However, in a real experiment, part of the cantilever excitation comes from the cantilever base vibration and the other part comes from the acoustic waves that propogates from the piezo-actuator through the fluid. The accurate determination of the contribution of the acoustic wave is not an easy task, since it depends on the geometry and the fixation of the cantilever in the holder. It is much easier to measure the whole driving force for a given cantilever in a liquid. The general expression for the total driving force in a liquid far from the substrate (which means the interaction force is neglected) can be written as [132]:

$$F_d = (F_1 + jF_2)e^{j\omega t}. \tag{3.5}$$

In the above relation, the term F_1 is in phase with the base vibration, while F_2 is the phase quadrature. The expression for these terms is obtained by inserting equation 3.1 and 3.5 in equation 3.2, and using $F_h = 0$:

$$F_1 = k_c A_{free}\left[\left(1 - \left(\frac{\omega}{\omega_0}\right)^2\right)\cos\varphi_{free} - \left(\frac{\omega}{\omega_0 Q}\right)\sin\varphi_{free}\right], \tag{3.6a}$$

$$F_2 = k_c A_{free}\left[\left(1 - \left(\frac{\omega}{\omega_0}\right)^2\right)\sin\varphi_{free} + \left(\frac{\omega}{\omega_0 Q}\right)\cos\varphi_{free}\right]. \tag{3.6b}$$

Where Q is quality factor, ω_0 is resonance of the cantilever,while A_{free} and φ_{free} are the amplitude and the phase of the cantilever far from the substrate, respectively. During the tip-sample interaction, the interaction stiffness and damping come into play and equation 3.3 is written as:

$$m^*\ddot{Z} + (\gamma_b + \gamma_{int})\dot{Z} + (k_c + k_{int})Z = (F_1 + jF_2)e^{j\omega t} - (k_{int} + j\omega\gamma_{int})A_b e^{j\omega t}, \tag{3.7}$$

and under the study condition,

$$\begin{aligned} k_{int} + j\omega\gamma_{int} &= \frac{F_1 + jF_2 + (m^*\omega^2 - k_c - j\omega\gamma_b)Ae^{j\varphi}}{Ae^{j\varphi} + A_b} \\ &= \frac{F_1 + jF_2 + [(\omega/\omega_0)^2 - 1 - j\omega/\omega_0 Q]k_c A e^{j\varphi}}{Ae^{j\varphi} + A_b}, \end{aligned} \tag{3.8}$$

By separating the real and imaginary part of the equation 3.8, we obtain the expressions for the interaction damping and stiffness as:

$$\frac{\omega\gamma_{int}}{k_c} = \frac{-\frac{AF_1}{A_b k_c A_b}\sin\varphi + \frac{F_2}{k_c A_b}\left(1 + \frac{A}{A_b}\cos\varphi\right) - \frac{A}{A_b}\sin\varphi\left(1 - \frac{\omega^2}{\omega_0^2}\right) - \frac{A\omega}{A_b\omega_0 Q}\left(\frac{A}{A_b} + \cos\varphi\right)}{1 + \left(\frac{A}{A_b}\right)^2 + 2\frac{A}{A_b}\cos\varphi}, \tag{3.9a}$$

$$\frac{k_{int}}{k_c} = -1 + \frac{\omega^2}{\omega_0^2} + \frac{\frac{AF_1}{A_b k_c A_b}\cos\varphi + \frac{AF_2}{A_b k_c A_b}\sin\varphi + \left(1 + \frac{A}{A_b}\cos\varphi\right)\left(1 - \frac{\omega^2}{\omega_0^2}\right) + \frac{F_1}{k_c A_b}\frac{A\omega}{A_b\omega_0 Q}\sin\varphi}{1 + \left(\frac{A}{A_b}\right)^2 + 2\frac{A}{A_b}\cos\varphi}. \tag{3.9b}$$

Moreover, the expressions for the amplitude and the phase of the cantilever deflection were obtained as :

$$A = \beta\frac{A_b\sqrt{(\omega^2 - k_{int}/m^*)^2 + (\gamma_{tot}\omega\omega_0/\gamma_b Q)^2}}{\sqrt{(k_{int}/m^* + \omega_0^2 - \omega^2)^2 + (\gamma_{tot}\omega\omega_0/\gamma_b Q)^2}}, \tag{3.10a}$$

$$\varphi = -\arccos\left(\frac{m^*\omega^2 - k_{int}}{\sqrt{(m^*\omega^2 - k_{int})^2 + (\gamma_{tot}\omega)^2}}\right) + \arccos\left(\frac{-m^*\omega^2 + k_c - k_{int}}{\sqrt{(m^*\omega^2 - k_c - k_{int})^2 + (\gamma_{tot}\omega)^2}}\right), \tag{3.10b}$$

where $\gamma_{tot} = \gamma_b + \gamma_{int}$ is the total damping. When the AFM cantilever is far from the surface, the above equations (3.10a and 3.10b) for the amplitude and phase of the cantilever are expressed as:

$$A = \beta\frac{A_b\omega\sqrt{(\omega^2 + \omega_0/Q)^2}}{\sqrt{(\omega_0^2 - \omega^2)^2 + (\omega\omega_0/Q)^2}}, \tag{3.11a}$$

$$\varphi = -\arccos\left(\frac{\omega^2}{\sqrt{\omega^4 + (\omega\omega_0/Q)^2}}\right) + \arccos\left(\frac{\omega_0^2 - \omega^2}{\sqrt{(\omega^2 - \omega_0^2)^2 + (\omega\omega_0/Q)^2}}\right). \tag{3.11b}$$

We excited the cantilever far from the substrate and recorded the amplitude A_{free} (red circles) and phase φ_{free} (blue squares) as function of the oscillation frequency, as shown in figure 3.2. The black solid line is the fitting curve using equation 3.11a. We extracted the resonance frequency $\omega_0/2\pi = 1375Hz \pm 5Hz$ and the quality factor $Q = 2.8 \pm 0.1$ for the cantilever. The driving forces F_1 and F_2 versus the frequencies are shown in figure 3.3.

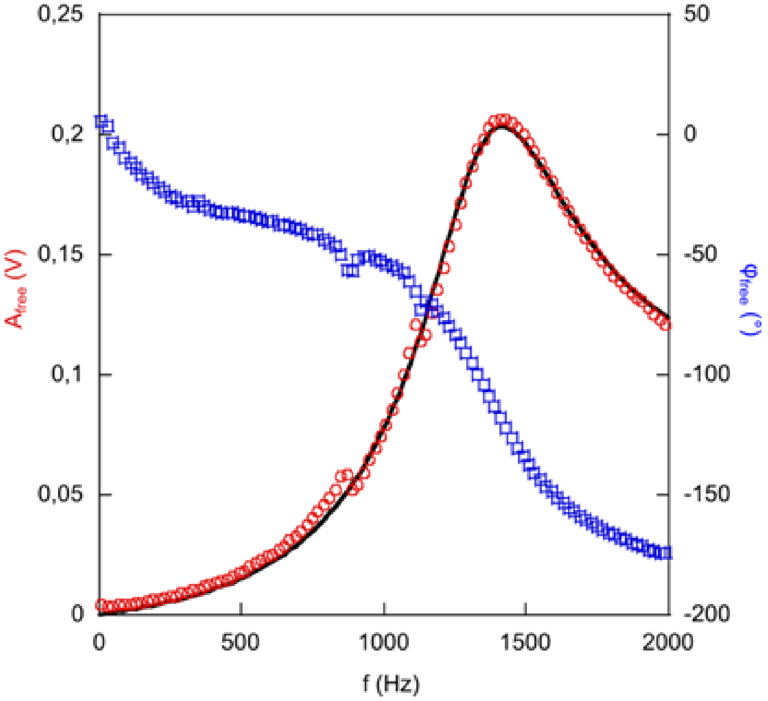

Figure 3.2: Amplitude (red circles) and phase (blue boxes) measured far from the PDMS (71:1) surface in viscous liquid dodecane. The solid line is the fit using the equation 3.11a and we obtained $\omega_0/2\pi$=1375±5Hz and $Q = 2.8 \pm 0.1$.

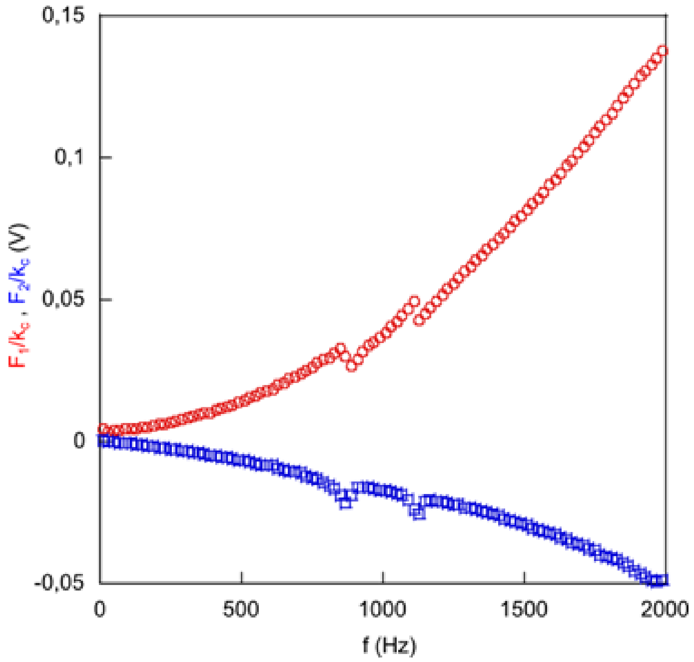

Figure 3.3: The real F_1 and imaginary F_2 components of the driving force are shown. These components were calculated from the amplitude and phase data in figure 3.2 using equation 3.6a and 3.6b.

These force curves were calculated from the data shown in figure 3.2, and using equation

3.6a and 3.6b for F_1 and F_2, respectively.

In order to obtain the base oscillation A_b, we have performed an experiment on a silicon surface that is hard enough to neglect the sample deformation, and thus the interaction is purely viscous. The interaction damping tends to infinity at $D \to 0$ (i.e. very close to the substrate), and the amplitude (see blue line, inset of figure 3.4) of the cantilever oscillation tends to be the base oscillation ($A \to A_b$) [132]. In our experiment, the amplitude of the base oscillation is determined as the measured amplitude just before contact on the silicone surface. The amplitude of the base oscillation is determined as A_b=3.1 nm at excitation frequency of $\omega/2\pi$=500 Hz, as shown in figure 3.4. The interaction damping and stiffness are determined using the equations 3.9a and 3.9b, and the determined parameters ($A_b, Q, \omega_0/\pi, F_1, F_2$ and piezo displacement).

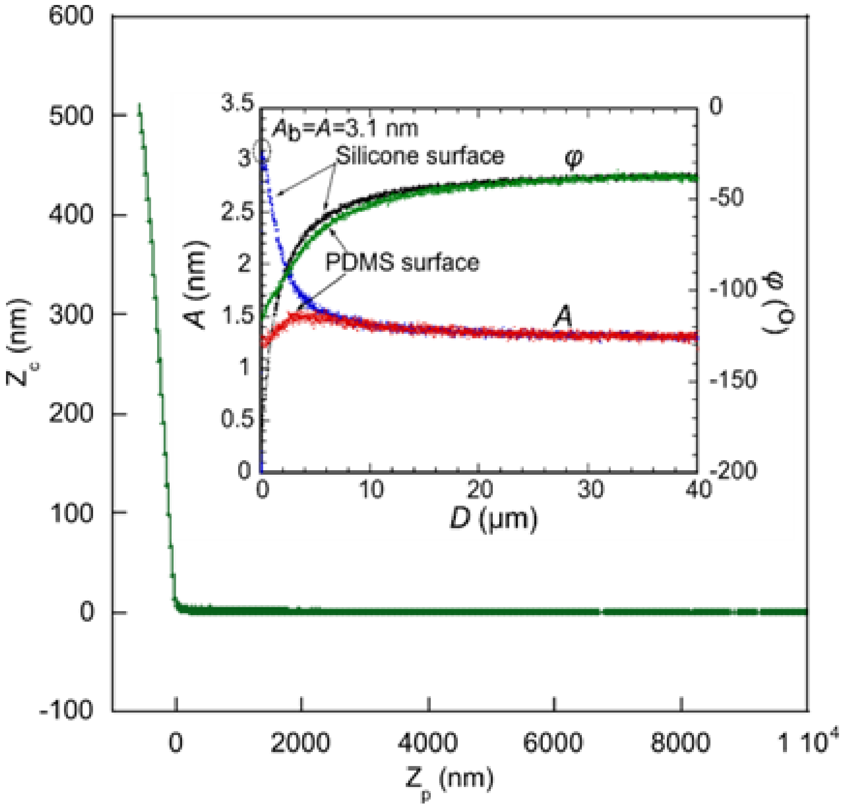

Figure 3.4: The cantilever deflection Z_c is shown as function of the piezo displacement Z_p on the silicon substrate. The oscillation frequency is set to 500Hz. Inset shows the measured amplitude and phase versus the distance for both silicone and PDMS (71:1) substrates.

Figure 3.5 shows the interaction damping and stiffness between the sphere and the silicon surface. The interaction damping increases as the tip-sample separation decreases, while the stiffness is zero, as there will be no elastic interaction in case of the hard substrate.

The interaction damping and stiffness for PDMS (71:1) substrate are shown in figure 3.6. The dynamic force response (see the inset of figure 3.6) shows two regimes in relation to the tip-sample separation. At large distance, the response is dominated by the damping and recovers the asymptotic expression of the hydrodynamic damping between a sphere

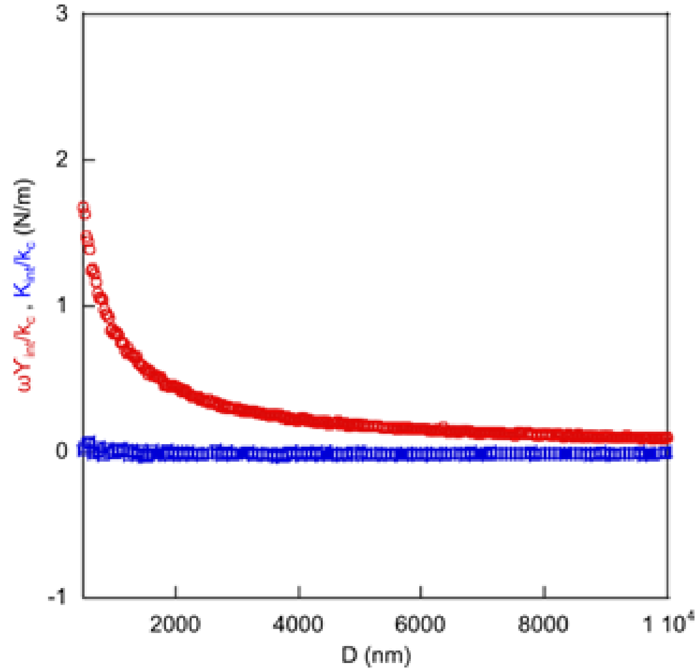

Figure 3.5: The calculated damping $\omega\gamma_{int}/k_c$ (red circles) and stiffness k_{int}/k_c (blue boxes) are shown versus the distance on the silicone substrate. The driving frequency is set to $500Hz$.

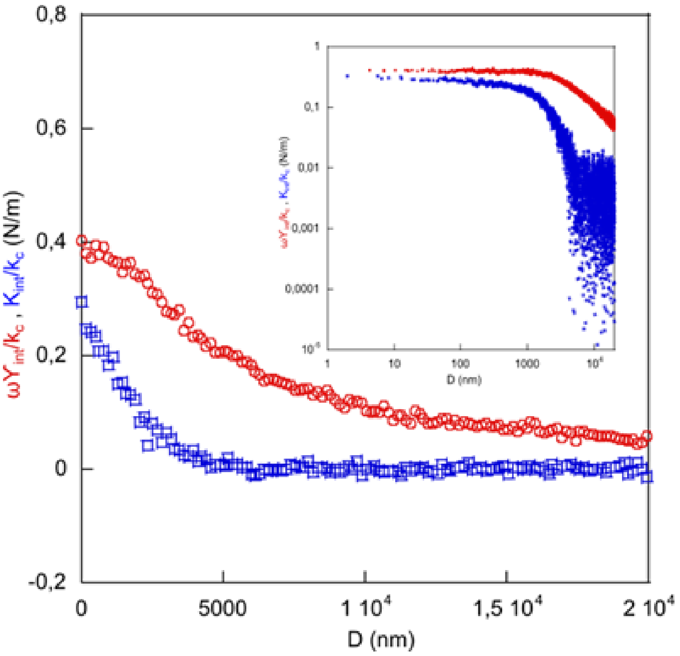

Figure 3.6: The interaction stiffness (in blue squares) and damping (in red circle) versus tip-sample separation at driving frequency of $500Hz$. These values are calculated from the data for amplitude and phase shown in figure 3.4. The interactions are also presented in the log-log scale in the inset of the figure.

and the hard substrate as $6\pi\eta R^2\omega/D$ [20]. In this regime the flow pressure is too small to make any significant contribution to the deformation of the surface. With further decrease in the distance, we start to get the elastic component of the force response. Lastly, very close to the substrate the damping and the stiffness saturate to a constant value, where the damping does not diverge as $1/D$ because the fluid is no longer being expelled from the gap between the sample and the probe. The elastic surface does not sustain the viscous pressure and accommodates for most of the probes displacements [20, 21, 128].

3.3 Analytical Solution for Viscoelastic Response: A Simple Model

A nanoscale flow induced by an oscillating sphere close to a soft substrate result in a hydrodynamic coupling between the sphere and the substrate. The response is obtained for small oscillation amplitudes compare to the distance D, which means the deformation of the sample will also be small compare to D. The typical distance over which the flow probes the surface and the fluid in the gap generates dynamic pressure is specified by the hydrodynamic radius ($\sqrt{2RD}$).

The force response with its elastic k_{int} and viscous part $\omega\gamma_{int}$, here after mentioned as G' and G'', respectively, is presented as function of the distance in figure 3.6. These curves display a power law regime as: at large distance the response is dominated by viscous damping and it scales as $1/D$, whereas, the compliance of elastomer appears at small distance through the elastic part of the response and scales as $1/D^{5/2}$. As the distance decreases, both the elastic and the viscous parts saturate to a constant value. This power law is the signature of a semi-infinite substrate having a thickness much larger than the hydrodynamic probe radius [20].

It is of interest to describe this scaling with a semi-quantitative model. A model scheme in figure 3.7 is used to fit the data. This model assumes that the system reacts as if two elements are placed in series. The fluid having a damping coefficient ($6\pi\eta R^2\omega/D$) applies pressure over the area $2\pi RD$. The substrate responds to this localized stress as a semi-infinite medium, with stiffness $k^* = \pi E^*\sqrt{2RD}$ [135]. Here, the complex modulus $E^* = E' + jE''$ of PDMS layer is considered to model its viscoelastic properties. The real part corresponds to the elastic modulus and imaginary part to the viscous one.

The dynamic force response G of this spring-dashpot in series is given by the following relations.

$$G = G' + jG'', \tag{3.12}$$

and

$$G = \left(\frac{1}{k^*} + \frac{1}{j\omega\gamma}\right)^{-1}. \tag{3.13}$$

In equation 3.13 the k^* has both viscous $k'' = \pi E''\sqrt{2RD}$ and elastic $k' = \pi E'\sqrt{2RD}$ components. Using equation 3.12 and 3.13, we express the mechanical impedances in the following relations:

$$G'' = \omega\gamma\left(\frac{\pi^2 E'^2(2RD) + \pi E''\sqrt{2RD}(\pi E''\sqrt{2RD} + \omega\gamma)}{\pi^2 E'^2(2RD) + (\pi E''\sqrt{2RD} + \omega\gamma)^2}\right), \tag{3.14a}$$

$$G' = (\omega\gamma)^2\left(\frac{\pi E'\sqrt{2RD}}{\pi^2 E'^2(2RD) + (\pi E''\sqrt{2RD} + \omega\gamma)^2}\right). \tag{3.14b}$$

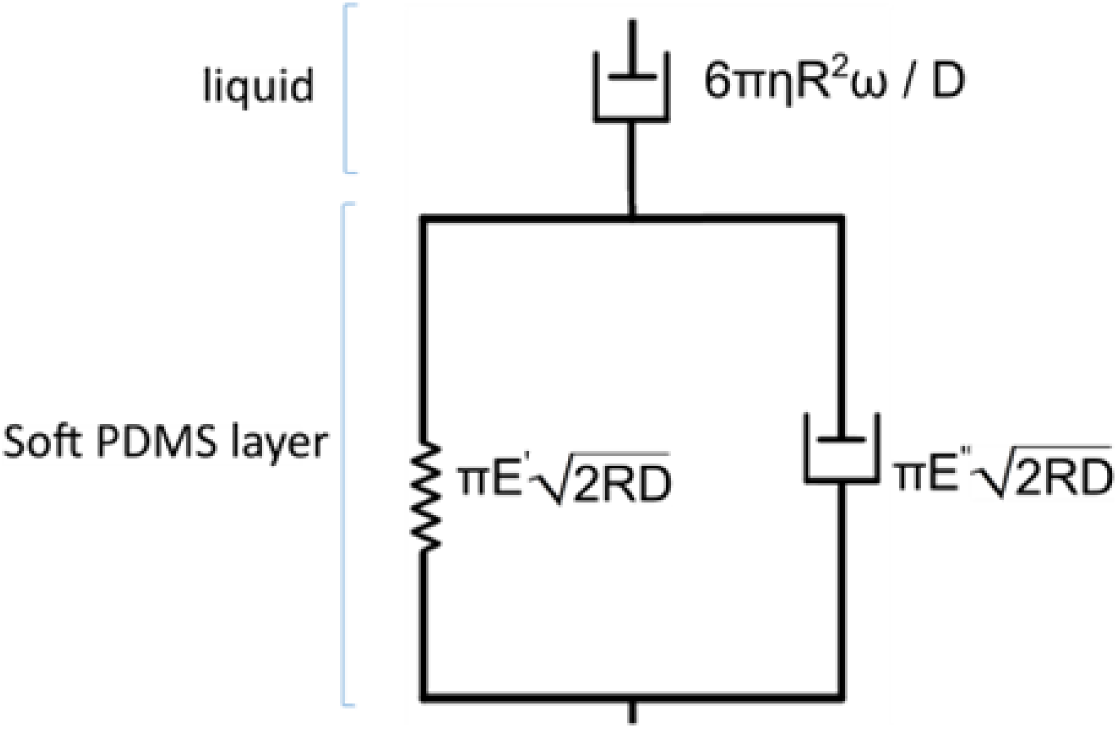

Figure 3.7: Spring and dashpot model corresponding to the experimental setup. The liquid (damping coefficient $(6\pi\eta R^2/D)$) applies pressure on the substrate. The soft PDMS modulus is complex having both viscous and elastic part.

In order to extract the effective modulus of the sample, the measured mechanical impedances were fitted using the simple model, as shown in figure 3.8. We observed a discrepancy at small distance for both elastic and viscous components. However, the model works reasonably well for large distance response. By fitting the data for large distances, we have extracted: $E' = 3.1 \pm 0.2kPa$ and $E'' = 2.6 \pm 0.3kPa$ at driving frequency of $500Hz$. We observe a behavior of $G' \sim D^{1/2}$ and $G'' \sim D^{1/2}$ in the low distance regime, which means a drastic drop in hydrodynamic force and infinite defromation. This is not possible, since the deformation of the sample cannot exceed the oscillation of the sphere. Note that even if the material is assumed to be pure elastic, this model fails to fit the low distance response (i.e. saturation part of elastic and viscous impedances).

For an absolute determination of the elastic and viscous moduli of the PDMS soft layer, Vincent Bertin (one of the collaborator in ESPCI Paris, PSL Research University) extended the model of Leroy and Elisabeth [20] to viscoelastic materials, which shows a good agreement with experimental measurements in all distance regimes. The model is described briefly in the next section.

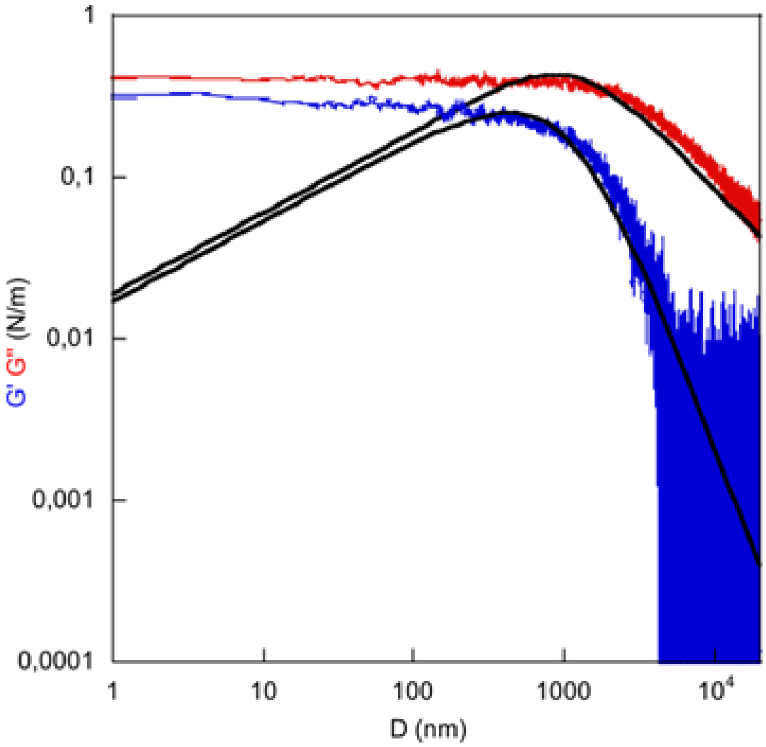

Figure 3.8: The real and imaginary part of the force response is shown for the PDMS (71:1) substrate at driving frequency of $500Hz$. The black solid lines correspond to the equations 3.14a and 3.14a to extract the modulus of the sample. By fitting the large distance response, we have obtained: $E' = 3.1 \pm 0.2kPa$ and $E'' = 2.6 \pm 0.3kPa$

3.4 Hydrodynamic Model for Viscoelastic Response

In order to rationalize the experimental data, a lubrication model was developed to describe the viscoelastic response of the samples. The schematic for a viscoelastic interaction of the PDMS film and a spherical probe immersed in viscous liquid is shown in figure 3.9. The spherical probe, which is at distance D from the substrate, oscillates vertically with a nanometric amplitude $Z << D$. The motion of the spherical probe creates an oscillating drainage flow and induces pressure on the PDMS substrate. The mechanical impedance, which is a ratio between the hydrodynamic force F_h and the amplitude of the sphere oscillation, is expressed as:

$$G(D) = \frac{F_h}{Z}. \tag{3.15}$$

The vertical flow is negligible compared to the lateral force, when $D \ll R$ and the liquid thickness in the gap obeys Reynold equation. The flow rate conservation gives the lubrication equation as [136]:

$$\frac{\partial h(r,t)}{\partial t} = \frac{1}{12\eta r}\frac{\partial}{\partial r}\left(rh(r,t)^3\frac{\partial}{\partial r}P(r,t)\right), \tag{3.16}$$

where P is the hydrodynamic pressure, r denotes the radial variable and $h(r,t)$ is the

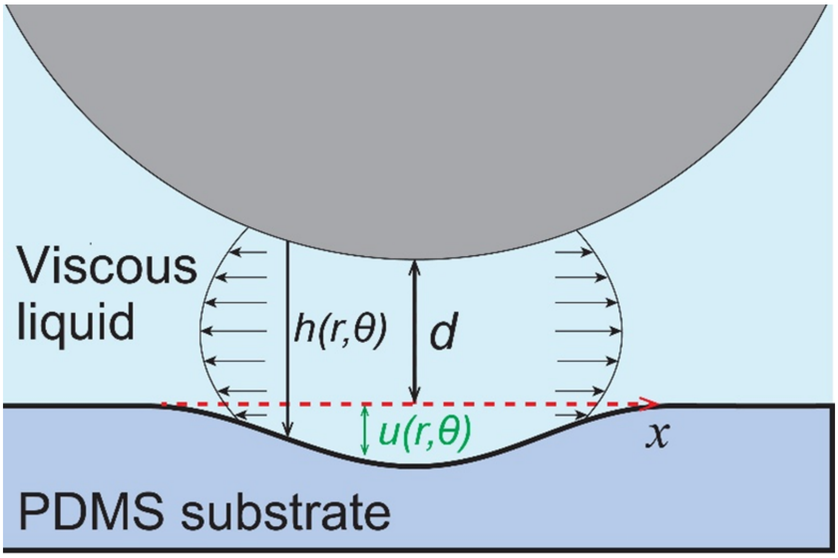

Figure 3.9: Schematic shows a supported elastic PDMS layer stressed by an oscillating spherical probe through the drainage of a viscous liquid.

fluid thickness, which is given as:

$$h(r,t) = D + \frac{r^2}{2R} + Z(t) + u(r,t), \tag{3.17}$$

where $u(r,t)$ is the deformation of surface and $Z(t) = A\cos\omega t$ is the cantilever oscillation. The amplitude of the base oscillation and the sample deformation are very small compare to the gap distance D, and thus equation 3.16 is linearized to form:

$$\frac{\partial Z(t)}{\partial t} + \frac{\partial u(r,t)}{\partial t} = \frac{\partial}{\partial r}\left[r\left(D + \frac{r^2}{2R}\right)^3 \frac{\partial}{\partial r} P(r) \right]. \tag{3.18}$$

The cantilever motion, the surface deformation and excess pressure are assumed to take time dependence in the form of: $\frac{\partial Z(t)}{\partial t} = i\omega Z(t)$, $u(r,t) = u(r)e^{i\omega t}$ and $P(r,t) = P(r)e^{i\omega t}$, respectively. Using these values, equation 3.18 becomes,

$$12\eta r i\omega\Big(Z + u(r)\Big) = \frac{\partial}{\partial r}\left[r\left(D + \frac{r^2}{2R}\right)^3 \frac{\partial}{\partial r} \tilde{P}(r,\omega) \right]. \tag{3.19}$$

Integrating equation 3.19 with respect to radial variable r, we get:

$$\frac{\partial}{\partial r} P(r) = \frac{6i\eta\omega r Z}{\left(D + \frac{r^2}{2R}\right)^3} + \frac{12i\eta\omega}{r\left(D + \frac{r^2}{2R}\right)^3} \int_0^r r u(r) dr. \tag{3.20}$$

The PDMS film is incompressible (i.e. Poission's ratio $v = 0.5$) and assumed to be a semi-infinite viscoelastic material with complex Young's modulus (E^*), which includes both the loss modulus $E''(\omega)$ and storage modulus $E'(\omega)$ [20]. Therefore, the deformation u is related to the axisymmetric pressure field through:

$$\widehat{u}(k) = \frac{2\widetilde{P}(k)}{E^*(\omega)k}, \tag{3.21}$$

with

$$\begin{aligned}\widehat{u}(k) &= \int_0^\infty J_0(kr)u(r)rdr \\ \widehat{P}(k) &= \int_0^\infty J_0(kr)P(r)rdr\end{aligned} \tag{3.22}$$

The $\widehat{u}(k)$ and $\widehat{P}(k)$ are the zeroth order Hankel transform of the deformation and the pressure, respectively.The J_0 is the zeroth order Bessel function of first kind. Thus the deformation of the sample will be:

$$u(r) = \int_0^\infty J_0(kr)\widehat{u}(k)kdk = \int_0^\infty J_0(kr)\frac{3\widehat{P}(k,\omega)}{2E^*}dk, \tag{3.23}$$

Inserting equation 3.23 in equation 3.20 and using the relation between the zeroth order J_0 and first order J_1 Bessel function, we obtain:

$$\frac{\partial}{\partial r}P(r) = \frac{6i\eta\omega rZ}{\left(D+\frac{r^2}{2R}\right)^3} + \frac{18i\eta\omega}{\left(D+\frac{r^2}{2R}\right)^3 E^*(\omega)}\int_0^\infty \frac{J_1(kr)\widehat{P}(k)}{k}dk. \tag{3.24}$$

We introduce the variables:

$$x = \frac{r}{\sqrt{2RD}}, q = k\sqrt{2RD}, p = \frac{PD^2}{\eta RZ\omega}, D_c = 8R\left(\frac{3\eta\omega}{4E'(\omega)}\right)^{2/3}, B(\omega) = \frac{E''}{E'},$$

then equation 3.24 can be expressed as:

$$\frac{\partial}{\partial x}p(x) = \frac{12ix}{(1+x^2)^3} + \frac{3i}{(1+x^2)^3}\left(\frac{D_c}{D}\right)^{3/2}\frac{1-iB}{1+B^2}\int_0^\infty \frac{J_1(qx)\widehat{p}(q,\omega)}{q}dq, \tag{3.25}$$

At first order Hankel transform of the equation 3.25 leads to a Fredholm equation for the dimensionless pressure:

$$\widehat{p}(q) = \frac{3i}{2}qK_1(q) - 3i\left(\frac{D_c}{D}\right)^{3/2}\frac{1-iB}{1+B^2}\int_0^\infty \widehat{P}(q')dq'\int_0^\infty \frac{J_1(qx)J_1(q'x)}{qq'(1+x^2)^3}xdx, \tag{3.26}$$

where K_1 being first order modified Bessel function of second kind. The mechanical impedance is then given by [20]:

$$G(D) = -\frac{1}{Z}\int_0^\infty 2\pi rP(r)dr = \frac{4\pi\eta\omega R^2}{D}\widehat{p}(q=0), \tag{3.27}$$

which is rescaled as:

$$G(D) = \frac{6\pi\eta R^2\omega}{D_c}g_c\left(\frac{D_c}{D},B\right), \text{where } g_c\left(\frac{D_c}{D},B\right) = -\frac{4D}{6D_c}\widehat{p}(q=0). \tag{3.28}$$

The function $g_c(\frac{D_c}{D},B)$ is a dimensionless complex function and is calculated numerically using the equation 3.26. At large distance $D >> D_c$, the response is dominated by the viscous component and the asymptotic expression of the hydrodynamic damping between a sphere and the substrate restores. The asymptotic expression for the force response in this regime (i.e. $D > D_c$) is given by:

$$G(D) = \frac{6\pi\eta R^2\omega}{D}\left(i + \frac{9\pi^2}{512}\left(\frac{D_c}{D}\right)^{3/2}\frac{1}{1+B^2}\right). \tag{3.29}$$

When the $D < D_c$, the elastic and viscous components of the force response saturate to a constant value. This is due to the fact that the indentation of the surface cannot exceed the amplitude of the sphere oscillation and the sample deformation accomodates the sphere motion. Besides a residual damping that occurs outside the gap due to the viscous flow, part of the damping occurs inside the soft PDMS due to the loss modulus of the soft PDMS. This later contribution increases as the oscillation frequency increases, and dominates at high frequencies. From the numerical calculation, we obtain the asymptotic value for G'' for small distances, which is given by:

$$G'' = \frac{6\pi\eta R^2\omega}{D_c}(1.16 + 1.32B(\omega)), \tag{3.30}$$

The above equation is valid for small B, typically $B < 2$, which is always valid for a gel.

Figure 3.10a and 3.10b show the dimensionless mechanical impedance $GD_c/6\pi\eta R^2\omega$ as a function of the dimensionless distance D/D_c for the PDMS(71:1) substrate for two excitation frequencies of $50Hz$ and $500Hz$, respectively. We have obtained the values for the elastic E' and the viscous E'' moduli by fitting the curves using equation 3.28 (solid lines). The values are extracted as $E' = 1.6 \pm 0.2kPa$, $E'' = 0.6 \pm 0.1kPa$ and $E' = 3.2 \pm 0.3kPa$, $E'' = 2.1 \pm 0.2kPa$ at the excitation frequency of $50Hz$ and $500Hz$, respectively. Moreover, the comparison between figure 3.10a and 3.10b shows that the real and imaginary parts of impedance crosses for the low excitation frequency and saturates to the same value at small distances, whereas for the higher frequencies, they do not cross and the imaginary part is larger than the real one at all distances. Furthermore, the dimensionles imaginary part increases as the frequency increases. Thus, we can deduce that the dissipation is more pronounced at large frequency, which means the increase with frequency is larger for loss modulus E'' than for the storage modulus E' (B increases as the frequency increases).

The extracted elastic modulus E' and viscous modulus E'' at different oscillation frequencies are shown in figure 3.11. Both loss and storage modulus increase with the increase of the excitation frequency. The PDMS (71:1) substrate, which is used in the experiment, is considered as a soft gel and the frequency dependence of the complex modulus is modeled by the Chasset-Thirion equation as [32, 137, 138]:

$$E(\omega) = E'(\omega) + iE''(\omega) = E_0(1 + (j\omega t)^n). \tag{3.31}$$

Where E_0 is the static Young's modulus ($\omega = 0$). The relaxation time t (which is regarded as the time duration for the spontaneous recovery of the deformation after the removal of external force) and the exponent n, (having values between 1/2 and 2/3 [139]), depend on the sample preparations, curing procedure and stoichiometric ratio between the PDMS and the curing agent. In figure 3.11 the solid lines are the fitting curves for both elastic and viscous moduli, which gives the values $E_0 = 1 \pm 0.1kPa$, $n = 0.5 \pm 0.02$ and $t = 3 \pm 0.2ms$. Note here that, the obtained relaxation time is in the range of value obtained from the Kelvin-Voigt model [140] where $\frac{\eta}{E_0} \approx 2 \sim 3ms$ with $E_0 \approx 1kPa$ and $\eta \approx 2 \sim 3Pa.s$.

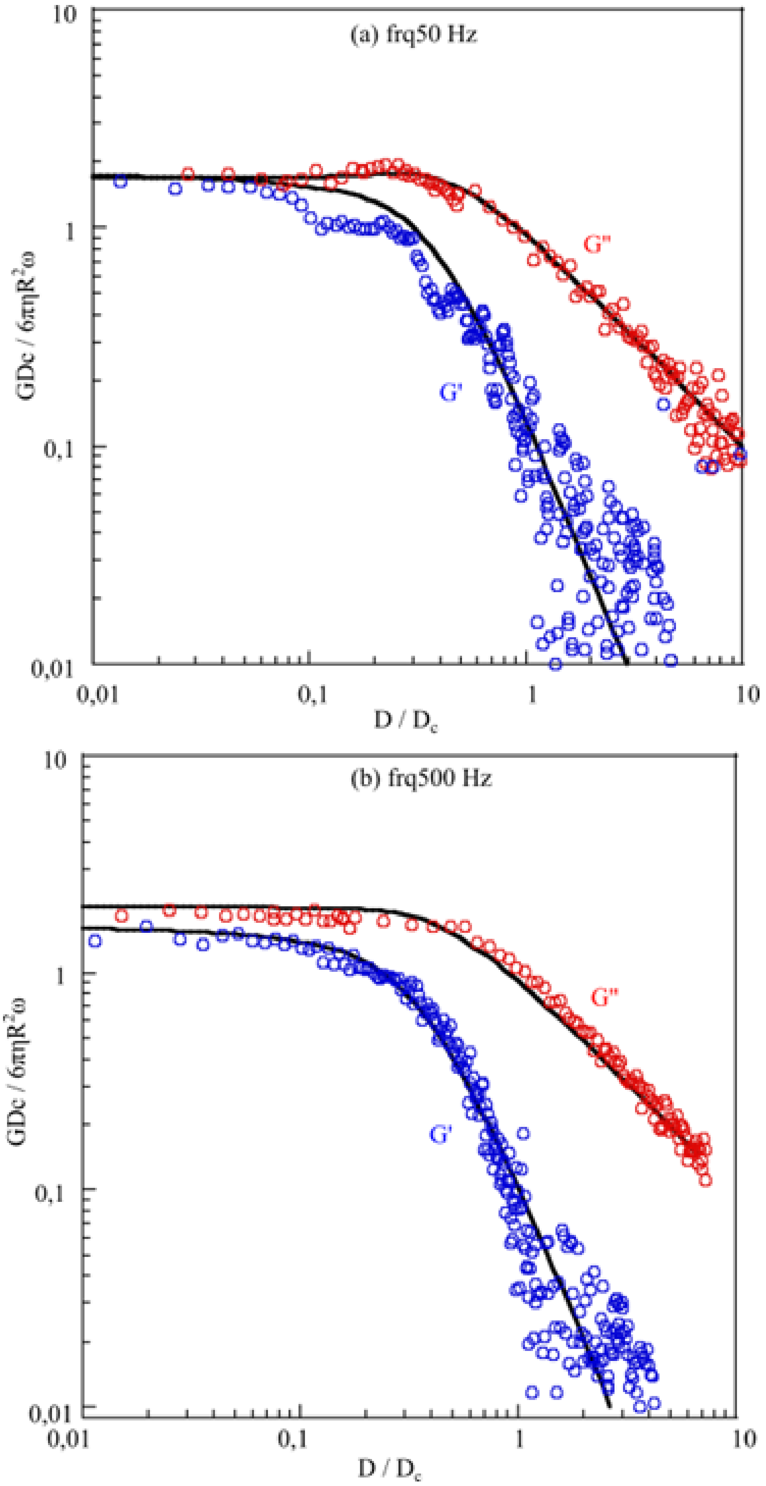

Figure 3.10: The normalized mechanical impedance is shown against the normalized distance for two oscillation frequencies. The black solid lines are the fitting curve (using equation 3.28) used to extract the loss E'' and the storage E' moduli. (a) The extracted values are $E' = 1.6 \pm 0.2kPa$, $E'' = 0.6 \pm 0.1kPa$ at the oscillation frequency of $50Hz$ (b) and when the oscillation frequency set to $500Hz$, we have obtained: $E' = 3.2 \pm 0.3kPa$ and $E'' = 2.1 \pm 0.2kPa$.

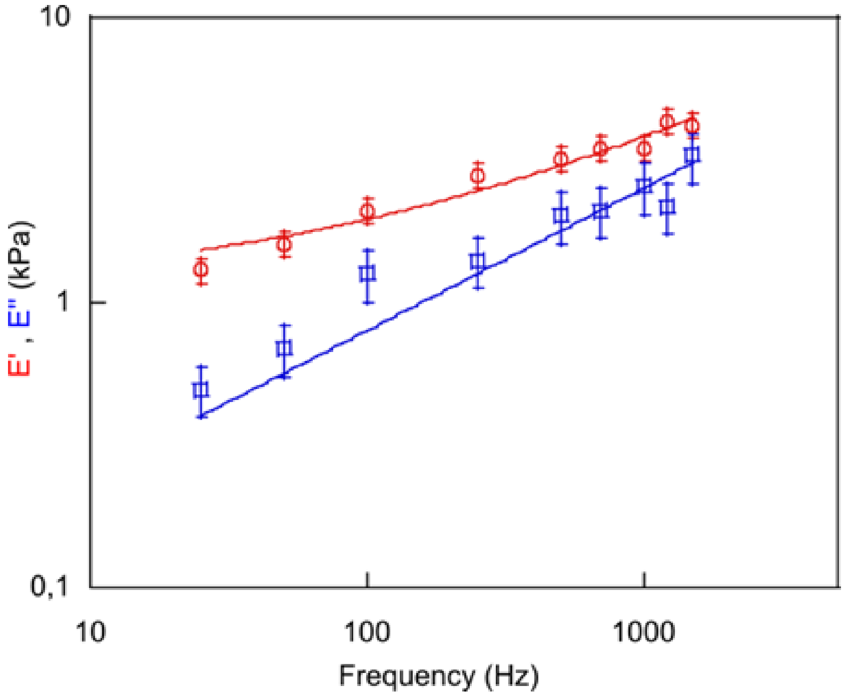

Figure 3.11: The extracted storage modulus E' (red) and loss modulus E'' (blue) for different excitation frequencies. The solid lines are the fitting using equation 3.31, and we obtained the parameters in the equation as: $E_0 = 1 \pm 0.1kPa$, $n = 0.5 \pm 0.02$ and $t = 3 \pm 0.2ms$.

3.5 Contact Mechanics

In order to check the validity of our measurement for the static modulus of the sample, we have analyzed the DC component of the cantilever deflection. The measured cantilever deflection versus the piezo displacement allows to construct the force indentation curve. The indentation δ is obtained by subtracting the cantilever deflection from the piezo displacement and zero displacement is defined as the position where the deflection of the cantilever increases sharply.

Several models of applied mechanics can be used depending on the shape of the AFM tip and the sample surface. For an elastic and infinitely thick sample the classical Hertz's model is the widely used model that describe the mechanics between two contacting bodies. For an applied load F the interaction of the AFM cantilever with an elastic half-space is given by Hertz as [135, 141, 142]:

$$F = \frac{4E_0}{3(1-v^2)} R^{1/2} \delta^{3/2}. \tag{3.32}$$

To minimize the contributions of the adhesion force and elasto-capillary effect [121, 143], we performed the analysis only on the regime of large indentation. But for large indentation, the value of the contact radius $\sqrt{R\delta}$ becomes comparable to the thickness h of the sample. Thus, the classical Hertz model for an incompressible sample (Poisson's ratio $v = 0.5$) should be corrected to [122]:

$$F = \frac{16}{9} E_0 R^{1/2} \delta^{3/2} \left[1 + 1.133\varepsilon + 1.283\varepsilon^2 + 0.769\varepsilon^3 + 0.0975\varepsilon^4 \right], \qquad (3.33)$$

with $\varepsilon = \sqrt{R\delta}/h$. The prefactor multiplied to the Hertz equation accounts for the finite thickness of the sample and must be taken into consideration.

Using equation 3.33 the fit (black solid line) of the force versus indentation curve is presented in the figure 3.12. The fit, which is for the indentation in the range of $0.5\mu m - 2\mu m$, gives static Young's modulus as $E_0 = 0.9 \pm 0.05 kPa$. The extracted value coincides to the value obtained from the fitting of the contactless measurement using equation 3.31.

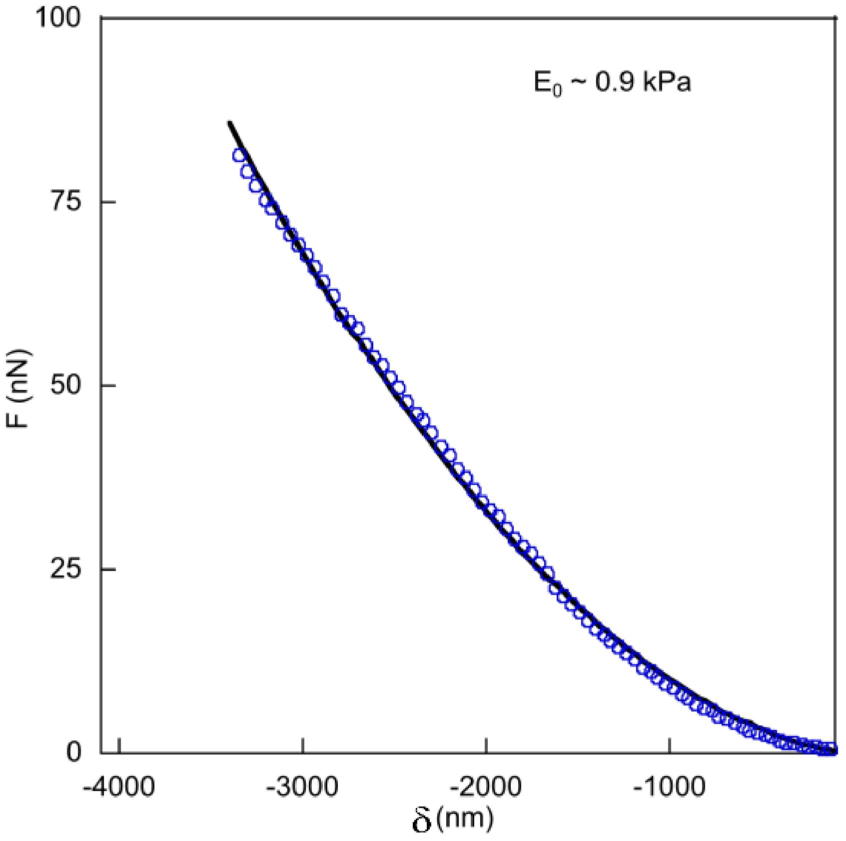

Figure 3.12: The quasi-static force versus the indentation δ. The black solid line is the fitting curve using equation 3.33 that gives the static modulus as $E_0 = 0.9 \pm 0.05 kPa$.

3.6 Conclusion and Perspective

The damping and stiffness coefficients of the tip-sample interaction are obtained using dynamic AFM method. The viscoelastic response measurements at different excitation frequencies for a PDMS (71:1) sample are performed without the solid-solid contact. This is achieved using a colloidal probe, which is vibrated vertically close to the PDMS surface to generate nanoscale flows. This viscous flow leads to the elastohydrodynamic coupling with a deformable surface. A simple (spring-dashpot) model was developed to extract the viscoelastic response of the PDMS sample. The model worked reasonably well for the large distance response, but a discrepancy observed in small distance regime. Based on the lubrication theory, we have developed a new model that relates the viscoelasticity of the PDMS sample to the mechanical force applied on the colloidal probe. Using this model and from the measurement of the mechanical impedance of the interaction, we have extracted the complex modulus for a wide range of frequencies. The extracted moduli as a function of the frequency are in good agreement with the Chasset-Thirion model. In order to validate the static modulus of the sample, we have also performed the quasi-static measurements and the findings are comparable with dynamic measurements using the non-contact method. In short, this method paves the way for a contactless investigation of the mechanical behaviors of thin polymers coatings, bubbles and soft biological layers in liquid environments for a wide range of frequencies.

It is an on-going project and will be extended further to characterize the viscoelastic properties of the various mixing ratios of PDMS at the wide range of excitation frequency. The PDMS substrates will be prepared in different mass ratio (higher cross-linked ratios) to perform the mechanical characterization. However, a single model with a finite number of parameters for the viscoelastic samples cannot describe the behavior of all materials due to the use of different relaxation mechanisms at different frequency scales. The Chasset-Thirion model, which was developed for the frequency response of the soft gel, might fail to capture the frequency response of these PDMS substrates. That is for, we also project to derive a theoretical model to fit the extracted storage and loss moduli for these samples to obtain their rheological properties at wide range of excitation frequencies.

The broader aspect of applications of this study provide a strong motivation for the study of hydrodynamic interaction in presence of deformable substrate. In continuation of this, the viscocapillary measurements at air-water interface is performed by one of our team member. They performed interfacial rheology of air-water interface in the absence of any direct contact at different excitation frequencies using the dynamic colloidal AFM technique. They probed the capillary deformation due to hydrodynamic pressure and used the numerical solution of Navier-Stokes equation in combination of Young-Laplace equation to fit the experimental results. The numerical calculation showed good agreement with the measurements and gave the surface tension of the bubble interface without direct contact.

Chapter 4

Friction between Polystyrene Microspheres

Contents

4.1 Introduction **62**

4.2 Mono Asperity Contact Model **64**

4.3 Materials and Method **67**

4.4 Experimental Measurements **69**

  4.4.1 Roughness Characterization of Polystyrene Microspheres 69

  4.4.2 Static Friction Measurement 70

  4.4.3 Dynamic Friction Measurement 73

  4.4.4 Viscosity Measurement of Suspension 79

4.5 Conclusion and Perspective **82**

4.1 Introduction

Concentrated suspensions of solid particles are present in technologies such as paints, coating, food materials, transport, drugs, and natural flows. The immense significance and wide occurrence of the suspensions have attracted researchers in the last two decades. The studies have revealed that a variety of non-Newtonian behaviors such as shear-thickening, shear-thinning, anisotropic normal stress, etc. are exhibited by the particle suspension rheology. Several features are highlighted in the literature [52, 144–148] to explain the origin of these behaviors. Some of these behaviors originate due to possible complexities (such as, the liquid is non-Newtonian, the particles may be of irregular shape, etc.) in the suspensions themselves. Additionally, the coupling between the flow, frictional contact between the particles, and spatial organization of particles in suspensions (microstructure) [149] also elaborate these behaviors. Nonetheless, it is noted that even a simple model for a suspension made up of non-Brownian (NB) and singly disperse particles in Newtonian liquid show non-Newtonian behaviors [52].

Several numerical [44–46], theoritical [47] and experimental [48, 49] work are evidence to the fact that the inter-particle friction has a significance influence on the rheology of the concentrated suspensions. Seto *et al.* [50], Mari *et al.* [51] and Wyart *et al.* [47] proposed to explain that the contact force leads to the explanation of Discontinuous Shear Thickening (DST), which is observed in the highly concentrated NB suspension. They proposed two cases in relation of pressure: at low pressure,two neighboring particles, separated by the gap filled with liquid, will interact via hydrodynamic force; at high pressure, the overwhelming of the repulsive forces between the micro-particles leads to the frictional contact between them . This model has given rise to several experimental validation including those of Guy [150], Clavaud [151], Comtet [48] and Hsu [152]. In the first two cases, authors have compared rheology of several suspensions whose DST characteristics stress tuned either by varying the particle size [150] or by the range of repulsive force between the particles [151]. Comtet *et al.* [48] performed direct measurement of frictional interaction between the pair of particle using quartz tuning fork based AFM, They observed a transition from lubricated contact at low load to frictional contact beyond critical load. They established a quantitative relationship between the critical load and the stress associated with DST. Hsu *et al.* [152] combined the tuning of the DST transition by varying the roughness of the particles and measurements of friction coefficient using the AFM. Their results explicitly show a strong link between the rheology of the suspensions and tribological properties of the particles.

Shear-thinning (define to be the decrease in the viscosity with the increasing shear rate) is a typical non-Newtonian behavior of the suspension, which was observed in many experimental results and attributed to the interparticle and fluid-particle interaction. Different mechanism, such as particle structuring under shear, frictional and adhesive interparticle interactions have been proposed in the literature to explain the origin of the shear thinning [144]. It was first explained by Acrivos *et al.* [153] back in 1994. They observed an apparent shear-thinning due to disparity in densities of the liquid and of the particles, when the viscosity of a NB suspension measured in the couette device. The origin of the phenomena in non-adhesive NB suspensions was not clear untill Chatte *et al.* [49] proved that the shear-thinning take place for higher stress than the DST characterstic stress. They confirmed that the interparticle interactions plays a strong role in determining shear thinning behaviour and the shear-thinning was found to be dominated by the frictional contact at high load. They used quartz-tuning fork based AFM to measure friction coefficient between two types of Polyvinyl Chloride (PVC) particles in liquid dinch (which is a solvent act as a plasticizer for particles). They also measured viscosity of the suspension based on type of particle and they confirm that there is a strong correlation between the value of jamming fraction (extrapolated from viscosity measurement at given volume fraction) and measured friction coefficient. This was first experimental proof that showed a relation between the shear thinning and friction. Around the same time, a model was proposed on bootstrap mechanism of friction where friction coefficient is a decreasing function of sliding speed between the particles [154]. This was followed by a scenario proposed by Lobry *et al.* [52], which showed that the quantitative study of the shear thinning is possible by properly modelling the contact between the particles. It was based on the assumption that in shear flow the particles come into contact via one or a few roughnesses.

Since at smaller (nanometric) length scale, when two macroscopic surfaces are brought in contact, unlike topographies end up in very little actual physical contact amongst surfaces. In this case, it is expected that the friction coefficient will no longer be constant, unlike to what happens for the macroscopic contact [155] . In Lobry model roughness are represented by the hemispheres whose radius is of the order of one thousandth of radius of the sphere. More and Ardekani [148] also used Lobry's model to study influence of roughness size on viscosity of suspensions. In their numerical studies both Tanner *et al.* [154] and Lobry *et al.* [52] used mono-contact friction model proposed by Brizmer [42], where the contact between a plane and perfectly smooth surface (single asperity) was considered. This microscopic friction model opens up possibility that the viscosity depends on the applied stress.

This work is dedicated to the rheology of NB suspensions with a focus on the role of the inter-particle friction in shear-thinning behavior. A quantitative experimental validation of Lobry's model, which links the viscosity to the friction and the shear-thinning to the load-dependent friction coefficient, will be presented. An AFM will be used to measure the friction coefficient between the polystyrene micro-spheres, immersed in Newtonian fluid, at different normal load. The cantilever twist and deflection will be recorded to obtain the friction and the normal force, respectively. The friction coefficient and its variation in a long range values of the normal force will be determined. The viscosity of the suspension of these particles (for several particle volume fraction) will be measured in rheometric experiment by our collaborators (team of Elisabeth Lemaire). The measured friction coefficient and the viscosity of suspension will be compared to the predictions of the Lobry model.

Here we will first present the summary of the mono-asperity contact under the combined normal and tangential loading. Then we will present our experimental data and their comparison to the Lobry model.

4.2 Mono Asperity Contact Model

Bowden and Tabor [36,37] simplified the Amonton's law, which was widely being used to explain friction. However it is not simple in single point contact like in an AFM experiment, where the contacts are not fully plastic, rather there is a range from fully elastic deformation to no deformation at all. Tabor has described fully plastic contact while, Hertz [156] has focused on elastic contact. The elastic-plastic spherical contact in coalesced normal and tangential loading is a conventional problem in contact mechanics. For the first time, Mindlin and Deresiewicz have solved the combined normal and tangential loading of elastic spherical contact [157,158], but the elastic-plastic mono-asperity contact model by Brizmer *et al.* [42, 43] best explain the elastic-plastic contact problem. They proposed that under combined loading central stick region is surrounded by slip zone and when tangential loading increases, the central region shrinks and at last vanishes. This is when sliding begins which satisfies Coulomb's friction law.

An Elastic-Plastic Single Asperity Contact Model

Consider two rough spherical surfaces of radius a_1, a_2 are in contact and the contact is materialized through surface asperities (see figure 4.1). It is presumed that the contact occurs between one asperity of radius h_r and smoothed patch of the second surface. In original work of Brizmer et al [42] the sphere was made up of elastic linear istropic hardening materials and the Hook's and Prandtl-Reuss constitutive laws governed the stress-strain relation in elastic and plastic regimes, respectively.

The friction coefficient is a ratio between the frictional force F_f and the normal load F_n, and a correlation was fitted to the variation of the frictional force to the load. The following two regimes are identified for the value of the normal load: one; when the load is smaller than the critical value L_c (at the given value of load the transition from elastic to plastic regime), the elastic effect dominates and the friction coefficient relates with load as $(F_n/L_c)^{1/3}$; two; when the load is larger than the critical value, the sphere experiences increasing plastic deformation and the friction coefficient slowly reduces to a constant value.

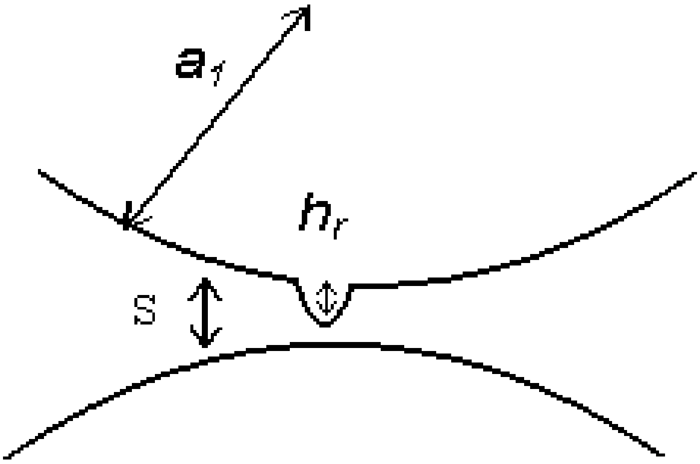

Figure 4.1: A sketch of the sphere in contact with an asperity of another sphere. The radius of the asperity is h_r and the distance between the spheres is defined by S.

A correlation between the normal load and the surface overlap ($\delta = h_r - S$) is also provided, which takes into account the transition from elastic to plastic regime. Additionally the influence of hysteresis of contact (that is related to the plasticity of the material) is neglected here. The normal force in the elastic regime ($\delta \leq \delta_c, L \leq L_c$) is given by the following relation:

$$F_n = L_c \left(\frac{\delta}{\delta_c}\right)^{3/2}, \tag{4.1}$$

whereas, in plastic regime ($\delta > \delta_c, L > L_c$) the normal force is shown as [52]:

$$F_n = L_c \left(\frac{\delta}{\delta_c}\right)^{3/2} \left[1 - \exp\left(\frac{1}{1 - (\frac{\delta}{\delta_c})^{\beta}}\right)\right]. \tag{4.2}$$

Where L_c and δ_c are the critical normal load and surface overlap, respectively, and $\beta = 0.174 + 0.08v$. The von Mises yield principle (that suggest yielding of ductile material begins when the elastic energy of distortion reaches a critical value) [159] is used to analysis the inception of plastic deformation for ductile materials with poisson's ratio in the range of $0.2 \leq v \leq 0.5$ [160, 161]. The von Mises stress expression along z-axis (i.e normal to surface) at any point for applied force is used to assess critical normal load and surface overlap at yield inception as:

$$L_c = \overline{L}_c \frac{\pi^3}{6} Y C_v^3 \left(h_r \frac{2(1-v^2)Y}{E}\right)^2, \tag{4.3}$$

$$\delta_c = \overline{\delta}_c h_r \left(\pi C_v \frac{(1-v^2)Y}{E} \right)^2 . \tag{4.4}$$

Here Y is the yield strength of the material and $C_v = 1.234 + 1.256v$ is the function of Poisson's ratio. The over-bare term, i.e. $\overline{L}_c$ critical load (in equation 4.3) and $\overline{\delta}_c$ critical overlap (in equation 4.4) are characteristics of full stick conditions. For smaller Poisson ratio these characteristics are considerably smaller as compare to the same parameters in slip. The reason for this is mentioned as the high tangential stresses in contact under the stick. But, for higher value of v tangential stresses in stick conditions are substantially low and it gives similar value for critical load and critical surface overlap as in slip conditions. For Poisson ratio $(0.2 \le v \le 0.5)$ the critical load and critical surface overlap are approximated as:

$$\overline{L}_c = [8.88v - 10.13(v^2 + 0.089)], \tag{4.5}$$

$$\overline{\delta}_c = [6.82v - 7.83(v^2 + 0.0586)]. \tag{4.6}$$

In the original work, Brizmer et al [42,43] have considered a flat rigid surface in contact with a sphere and this was swapped to the case of two spheres in contact. Here, we will focus on an asperity-sphere contact and requal the principle findings of Lobry's model.

In Lobry's model [52] for the case of stick phase, the tangential force has been designed as linear spring like force as [44,161,162]:

$$F_f = k_t y, \tag{4.7}$$

with y is the tangential displacement and the k_t is the tangential stiffness. The relative tangential displacement of two surfaces is estimated as the integral of slip velocity during the contact [45]. For elastic spherical contact under full stick, Mindlin [157] gave analytical solution for the tangential stiffness of the junction as:

$$k_t = \frac{F_f}{y} = \frac{4Ea}{2-v}, \tag{4.8}$$

with $a = \sqrt{R\delta}$ is the contact radius. Using equation 4.8 and the classical Hertz equation $F_n = 4ER^{1/2}\delta^{3/2}/3(1-v^2)$, we obtain:

$$\frac{F_f}{F_n} = 3\frac{1-v^2}{2-v}\frac{y}{\delta}, \tag{4.9}$$

or

$$k_t = 3\frac{1-v^2}{2-v}\frac{F_n}{\delta}. \tag{4.10}$$

The above relation shows that the tangential stiffness is a function of Poisson's ratio and the normal force intensity. In order to be more consistent with the earlier work [44,45], and in particularly to fit the experimental data obtained by Shafer *et al.* [163], the prefactor in the above equation was estimated as [52]:

$$k_t = \frac{2}{7}\frac{F_n}{\delta}, \tag{4.11}$$

the coeffcient 2/7 is smaller than the $3(1-v^2)/(2-v)$ as originally estimated by the Brizmer *et al.* [42].

Equation 4.7 for the case of the stick phase is $|F_f| < \mu|F_n|$. Whereas, for the slip phase the tangential force is given as:

$$|F_f| = \mu|F_n|\frac{F_f}{|F_f|}, \tag{4.12}$$

with μ is the static and dynamic friction coefficient.

Friction Coefficient

It is mentioned earlier that the elastic–plastic contact behavior over wide range of the normal load starts from the elastic and extends to the elastic-plastic contact. Brizmer et al [42] have shown that for the smaller value of the normal load, the dimensionless tangential load F_f/F_n against dimensionless tangential displacement y/δ shows a constant behavior. But as the tangential loading increases, the junction becomes more and more plastic and ultimately at a certain value of friction coefficient μ, tangential stiffness disappears completely, which is marked as the sliding inception [160]. The friction coefficient at sliding inception as a function of the normal load has the following forms [42, 43] :

$$\mu = 0.27\coth\left[0.27\left(\frac{|F_n|}{L_c}\right)^{0.35}\right]. \tag{4.13}$$

This expression accounts for transitions from elastic to plastic deformation, where the friction coefficient decreases with increase in normal force and at last levels off at high load. In elastic regime $\mu \propto (L_c/F_n)^{0.35}$ is nearly in agreement with Hertz contact law, where the relation between the normal force and contact area is $a \propto F_n^{2/3}$. At higher values of normal force, the material in contact zone undergoes plastic deformation and gives constant friction coefficient at $\mu = 0.27$.

4.3 Materials and Method

Materials

We have used polystyrene particles (Dynoseeds TS40 from Microbeads), with nominal radius of $20\mu m$ for the friction studies. These particles were also used by our collaborators in InPhyNi, Universite Cote d'Azur in Nice in rheometric experiment. They made a suspension in mixture of water, Ucon oil (75-H-9000, Dow) and 1.5% aqueous solution of zinc bromide. We have used the same liquid having viscosity of $50mPa.s$ in our AFM measurements of friction between the microspheres.

AFM Probe and Samples preparation

For friction study between the microspheres, the probing sphere of radius $20\mu m$ was glued to rectangular cantilevers (NSG 11/tipless) while the probed spheres were glued on to a glass substrate. For the roughness measurements, we used an AFM cantilever (PPP-Cont) having a sharp tip of height $10\mu m$ and radius of curvature less than $10nm$.

For the sample preparation a clean microscope glass slide was coated with a thin epoxy glue (Araldite) layer. Then the spheres were manually dispersed on the sticky surface.

After a while, jet of filtered air was used to remove the non-sticked spheres from the substrate. These microparticles glued to the substrate (see figure 4.2) were used in the friction and the roughness measurements.

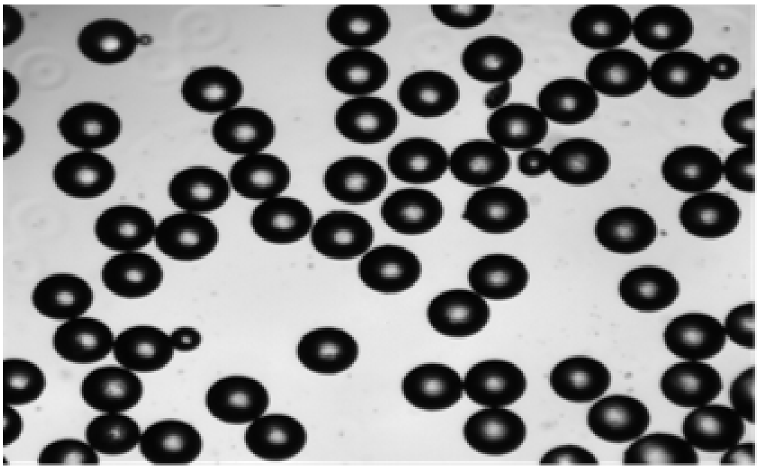

Figure 4.2: The optical image of polystyrene (TS40) spheres glued on a glass substrate.

Experimental Setup

We performed experiment using AFM (Bioscope II, Bruker) equipped with liquid cell (DTFML-DD-HE, Bruker) that allows working in liquid environment. The experimental setup is shown in figure 4.3.

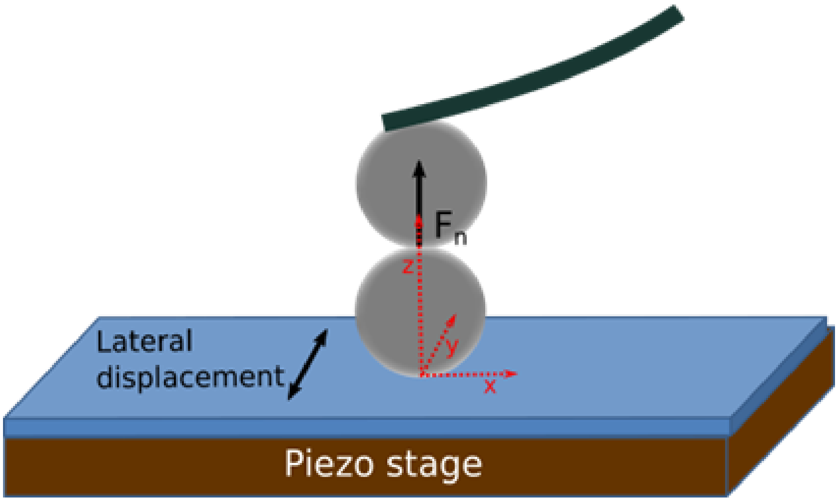

Figure 4.3: Experimental setup for the friction measurements.

After successful vertical and lateral calibration of the cantilever on a flat hard substrate (see chapter 2), we replace the hard substrate with the microspheres glued substrate on the piezo stage. The probing sphere on the cantilever tip is positioned a few millimeters above the glass substrate and a few drops of a liquid are poured in to form a thin liquid layer that has immersed both the probed and the probing spheres. After adjusting the laser at the tip of the cantilever, the AFM motor is used to approach the colloidal probe to one of the spheres on the substrate. We have centered the probe and the probing sphere using the optical microscope and also we have used the AFM in image mode for finer centering. The photodiode signals are recorded to measure both the vertical and the lateral forces. We have also recorded the output of the piezo in the y-direction to be sure about the lateral displacement.

The results for the roughness characterization and the friction (static and dynamic) measurements of the polystyrene spheres are discussed in the next section.

4.4 Experimental Measurements

4.4.1 Roughness Characterization of Polystyrene Microspheres

The topography and the friction images are obtained in contact mode with the resolution of 512×512 $pixel^2$. The set point (described as the applied load) is kept at $0.3V$ for whole set of experiments. We have performed the experiment at scan rate of 1Hz and scan sizes of $20\mu m\times$ $20\mu m$ and $5\mu m\times$ $5\mu m$. Images are recorded on several spheres to obtain an average value for the roughness of the spheres.

In figure 4.4(a), we present a 3D AFM image of polystyrene microsphere obtained in contact mode for the scan size of $5\mu m\times$ $5\mu m$. Figure 4.4(b) is showing the height section of the 3D image. We have removed the local curvature deviation by flattening the sphere image using plan fit at 3rd order for both x and y axis, shown in figure 4.4(c). In standard operations, the plane fit command figures out a polynomial of selectable order and subtract it from each scan line of image. The order and direction (either in x, y or both) of plane fit are required to be set for the particular operation. Since the plane fit of the order 0th, 1st, 2nd and 3rd are applied to center the data, remove the tilts, remove the 2nd and 3rd order bow, respectively. To go further, the height section for the plan fitted image is presented in figure 4.4d at different position (shown in different colors). The root mean squared roughness (Rq) on the image of polystyrene microsphere is measured as $Rq = 20 \pm 0.2nm$ and peak to peak value is of the order of $100nm$ (see figure 4.4d).

We have also performed quasi-static force measurements between the polystyrene microspheres to extract the adhesion force. The experiment was performed in a solution of $water + ZnBr$. The sphere-glued substrate on the piezo stage was imposed to approach the colloidal probe at velocity of $6\mu m/s$. The measured cantilever deflection versus the piezo displacement allow to construct the force curve. The value of the adhesion force is extrapolated from the retract curve as $F_{adh} \approx 18 \pm 2nN$.

From the microscopic model requaled in section 4.2 the dimensionless parameters (R, h_r, δ_c) and L_c are identified from the relevant length and force scales, respectively. Here the h_r is given by the value peak to peak obtained from image in figure 4.4d. The inter-particle force is quantified by the critical force L_c and we have estimated the critical force $L_c \sim 30nN$ using equation 4.3 with $h_r \sim 100nm$ $E \sim 3GPa$, $Y \sim 73MPa$ and $v = 0.33$ [164].

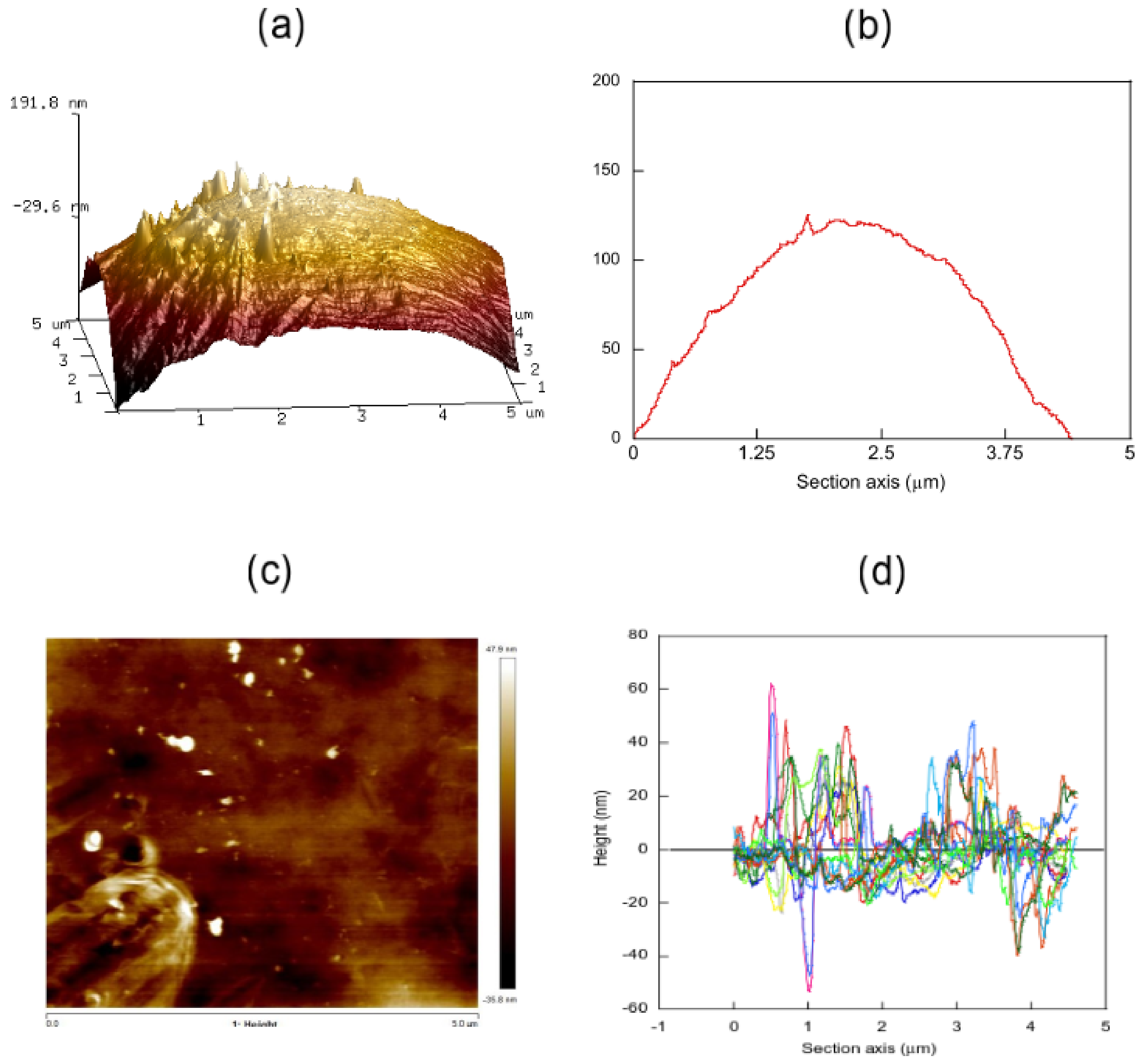

Figure 4.4: An AFM image of polystyrene sphere: (a) 3D AFM height image for sphere in scan size of $5\mu m\times$ $5\mu m$. (b) Height section for the image (a). (c) 3rd order plan fit of the image from which we obtain Rq=20 $\pm$ $0.2nm$. (d) The height section of plane fitted image at different positions i c.

4.4.2 Static Friction Measurement

The sharp tip cantilever is replaced with the polystyrene sphere glued cantilever in the liquid cell. During the typical experiment, the micro particles (the colloidal probe and glued spheres on the substrate) are immersed in aqueous solution of zinc bromide for the quasi-static friction measurements. The colloidal probe is centered to one of the spheres on the substrate and we have measured vertical load and frictional force by recording the AFM photodiode signals. The vertical deflection of the cantilever for each set point (set point was varied from $0.1V$ to $7V$) is recorded, which gives the normal force by multiplying the cantilever deflection to the spring constant $k_c = 3.4N/m$ of the cantilever. The lateral deflection of the cantilever is also recorded after setting the input to the y-direction of the piezoelectric actuator that has induced a lateral movement of $10\mu m$ in the substrate.

Typically, the frictional characteristics of a sample are studied by analyzing the friction curves. In figure 4.5, the friction curves are presented for the different set of the applied load. We observe an increase in the lateral deflection as per classical frictional laws, which state that the friction force increases with the increasing load. The lateral deflection variation V_y is measured for the given applied load from the friction curve. Knowing the lateral conversion factor k_t^l (discussed in section 2.3.5), the torque produced in the cantilever is given by $\tau = k_t^l V_y$. Subsequently, the friction force is deduced using the relation $F_f = \tau/2R$.

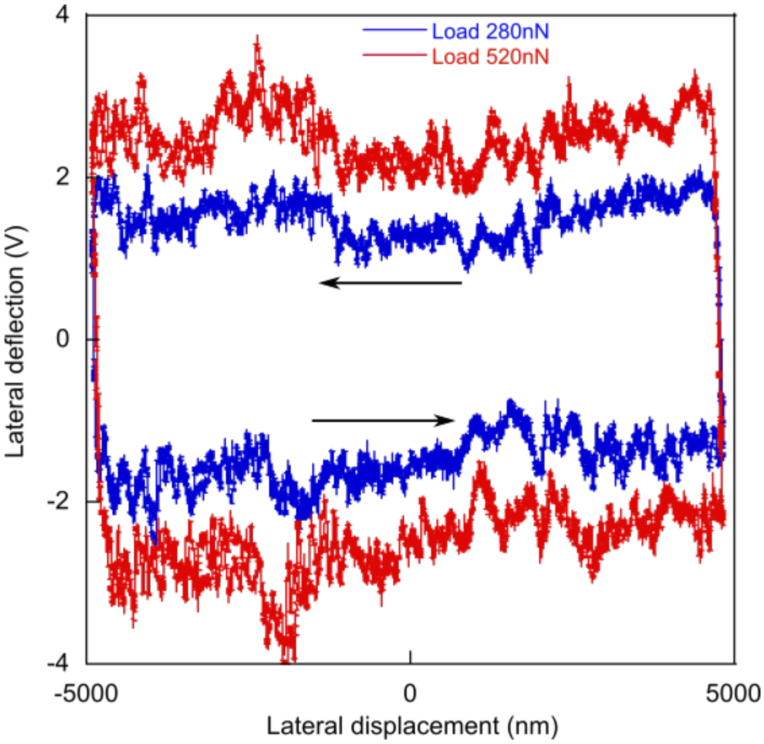

Figure 4.5: Lateral deflection of the cantilever is shown for different set of the applied load.

Once the measured signals are converted to the forces (i.e. normal and friction force), the friction coefficient μ of the polystyrene microspheres can be obtained by the ratio of the two force. In figure 4.6 we present the measured friction force versus the normal force and it is observed that at low load the relation between the two forces is not strictly linear. The friction coefficient versus the load is presented in figure 4.7. The friction coefficient measured for the larger applied loads has shown a deviation from the general pattern of the variation of μ with F_n. The measurements for the larger applied loads, are performed last in the given set of experiments, so most probably due to long time duration the normal force varies because of the variation in the photodiode response (drift). Although, the quasi-static measurements hardly lead to a reliable quantitative results, but still the variation of the friction coefficient with the load in measurements made in quasi-static mode gave same tendency to what is obtained in the dynamic mode measurements that will be shown in the next section.

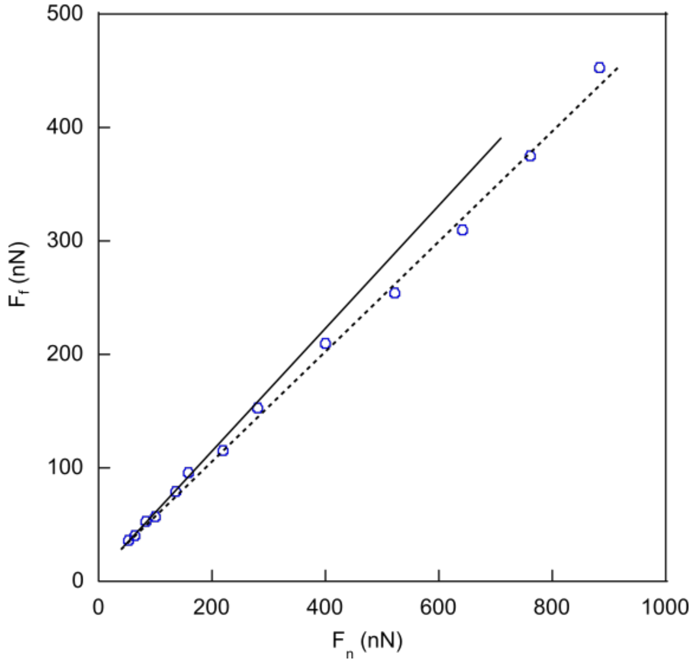

Figure 4.6: The friction force versus the applied load: The measured vertical and lateral deflections at different set points are converted to the normal and the friction force, respectively. The linear fit (at low load (solid line) and at high load (dashed line)) shows that at low load the relation between the friction and the load is not linear.

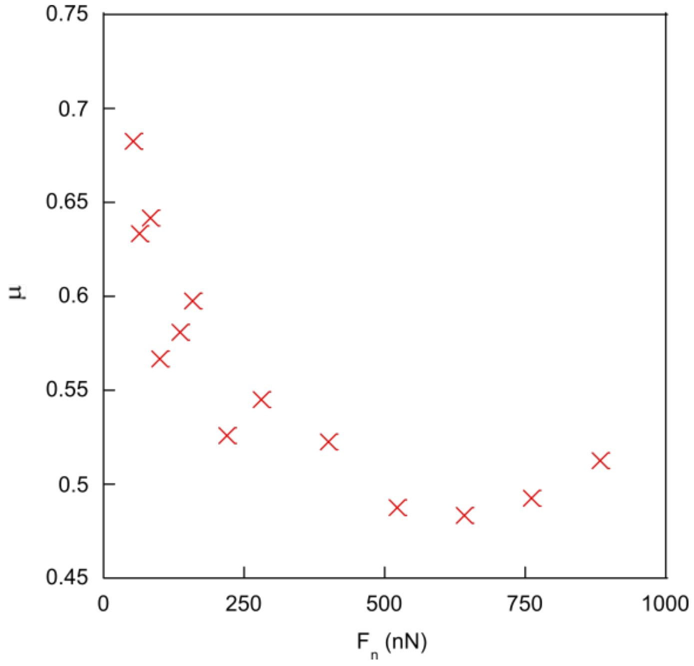

Figure 4.7: The measured static friction coefficient is presented as function of the applied load.

4.4.3 Dynamic Friction Measurement

In this section, we present the friction measurement using the dynamic mode AFM. After the vertical alignment of the colloidal probe to one of the spheres on the substrate, we have imposed the simultaneous vertical motion and the lateral oscillation of the substrate. The substrate is moved vertically at a low velocity of $0.1 \mu m/s$ to approach the colloidal probe, while for the lateral oscillation, the driving amplitude is varied around $1 \mu m$ at the driving frequency of 25, 50 and $100 Hz$ (see figure 4.8). We have obtained both the normal and the lateral force profile for the two approaching polystyrene microspheres.

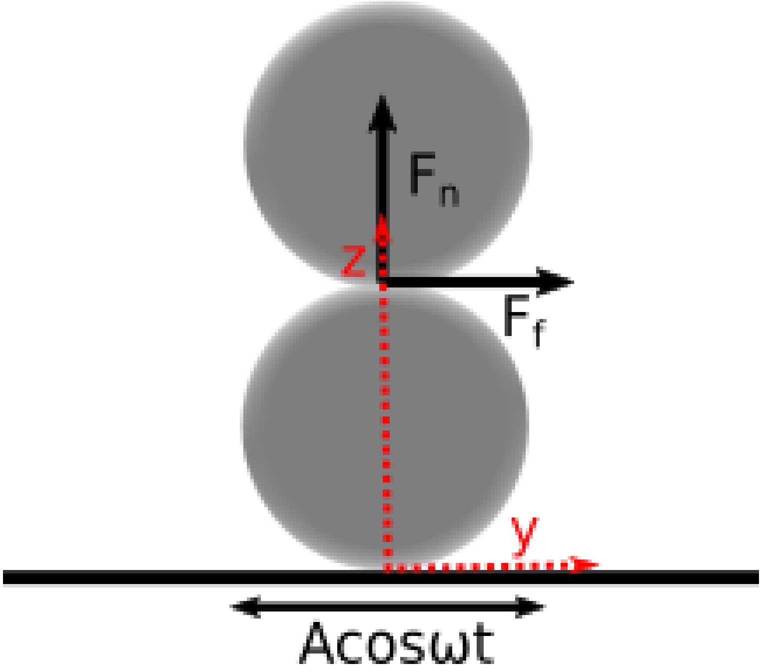

Figure 4.8: The schematic for the experimetal setup based on dynamic AFM method. A colloidal probe is shown in contact with a sphere, which is glued on an oscillating substrate.

Normal Force

The multiplication of the normal spring constant of the cantilever to the measured vertical deflection gives the normal force. As an example the normal force is shown against the piezo displacement in figure 4.9. The normal force increases as the microspheres come in contact. The vertical velocity of the substrate is sufficiently small to neglect the vertical lubricating hydrodynamic force. It is observed that an oscillation is induced in the normal force (see the inset of figure 4.9), which is contributed by the horizontal oscillation of the substrate. The quasi-periodic component of the normal force comes from the curvature of the spheres. The effect of particle curvature on AFM measurement of the normal and the lateral forces was studied in details and it was concluded that this effect could be very important if the particle size is not very large compare to the amplitude of lateral oscillation of the substrate [165]. However, in our study the particles of radius $20 \mu m$ are used in the experiments and the vibration amplitude of the substrate is in the order of a micron, so we can neglect this effect. Additionally, the curvature effect is nullified by considering the measurements of the normal and the lateral force over at a sufficiently

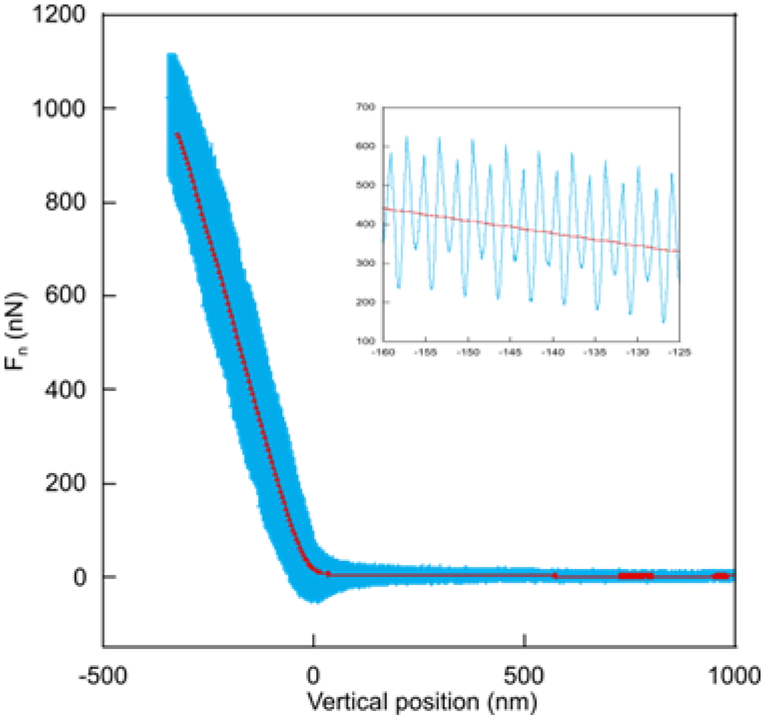

Figure 4.9: Normal force versus the piezo displacement is shown for working frequency of $25Hz$ and y-direction amplitude of $1.05\mu m$. The blue curve is the measured force while the red line is the force averaged over a period of oscillation of the substrate. Inset of the figure is the zoom of variation of the load verus the piezo position.

small interval of the lateral oscillation where the variation of normal force is small in comparison with its mean value. That is the reason, we have considered only the central region for each quasi-cycle so that normal force varies less than 10% from its mean value.

Friction Force

In figure 4.10, the measurements corresponding to the lateral deflection (before and after the contact) are presented. As the two approaching particles come in contact, the lateral deflection signal increases with the increasing load. In the inset of the figure, we zoomed in to observe the signal variation. For the same data, the friction curve versus the lateral displacement is presented in figure 4.11 for one period. As discussed in section 4.4.2, the friction force between the two spheres is deduced using the measured lateral deflection signal in volts.

In figure 4.12, we presented the typical friction versus load curve measured at oscillating frequency of $25Hz$ and amplitude of lateral displacement of one micron. The friction force increases nonlinearly with the normal force leading to a decreasing friction coeffcient with the increasing normal force. As discussed earlier that for quasi-cycle, we considered only the mean value of normal force, and in this region, the friction coefficient is defined as:

$$\mu = \frac{\langle F_f^{up} \rangle - \langle F_f^{down} \rangle}{2F_n^{mean}}, \tag{4.14}$$

Where F_f^{up} - F_f^{down} are the frictional force recorded when the substrate moves to the right

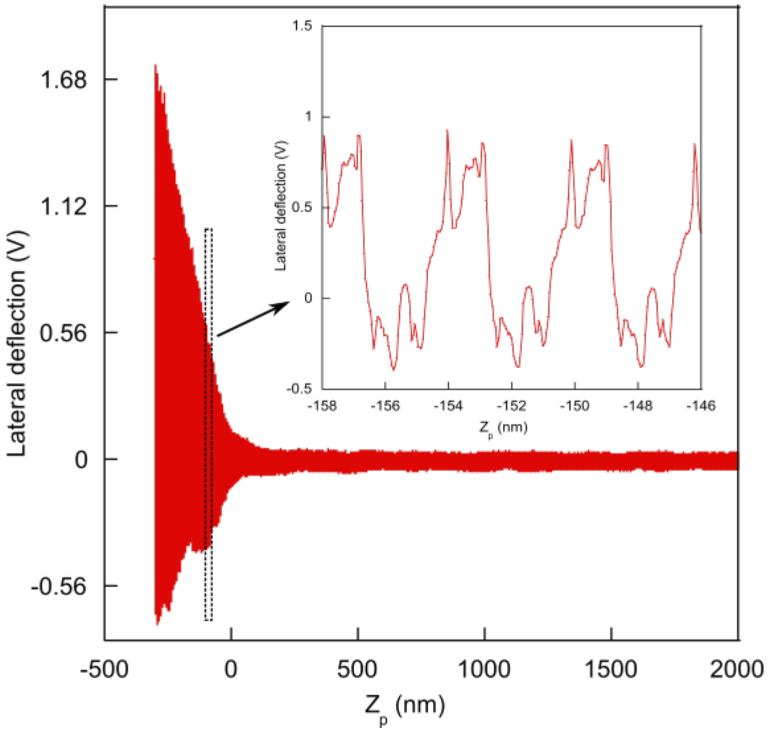

Figure 4.10: The measured lateral signals as function of the spheres separation for working frequency of $25Hz$ and y-direction amplitude of $1.05\mu m$ are presented. The Inset of figure is zoomed in look at the voltage variation corresponding to the lateral deflection.

($y' > 0$) and to the left ($y' < 0$), respectively. In figure 4.13 the typical variation of normal and frictional force during a cycle are shown. In equation 4.14 the symbol $\langle ... \rangle$ mean an average over the chosen interval of lateral displacement [166].

Friction Coefficient

Series of experiments were performed for the friction coefficient measurements between different pairs of the polystyrene microparticles at different driving frequencies and different lateral driving amplitudes. The variation of the friction coefficient μ is plotted against the normal force in figure 4.14. This figure shows the measured friction coefficient for 12 realizations and the averaged friction coefficient shown with a solid blue line. It is observed that μ decreases for increasing normal force and reaches a plateau at higher load, which is in conformity with the mono-asperity contact model. A significant variation is observed in the measured friction coefficient from one realization to another. These variations are not because of any experimental uncertainty, but due to spatial variation of local friction coefficient, especially when taking into account the surface roughness. The characteristic extension of surface roughness is, more or less, of the order of one micron and that is of the order of magnitude of lateral displacement set during the friction experiment. That is why, it is not surprising that the local friction coefficient changes from one realization to another. The mean friction coefficient is fitted with a Brizmer-like model [42], where the friction coefficient is fixed to 0.18 at infinite normal load with two free parameters L_c and n. The resulting friction coefficient is expressed as:

$$\mu = 0.18 \coth\left(0.18\left(\frac{F_n}{L_c}\right)^n\right), \tag{4.15}$$

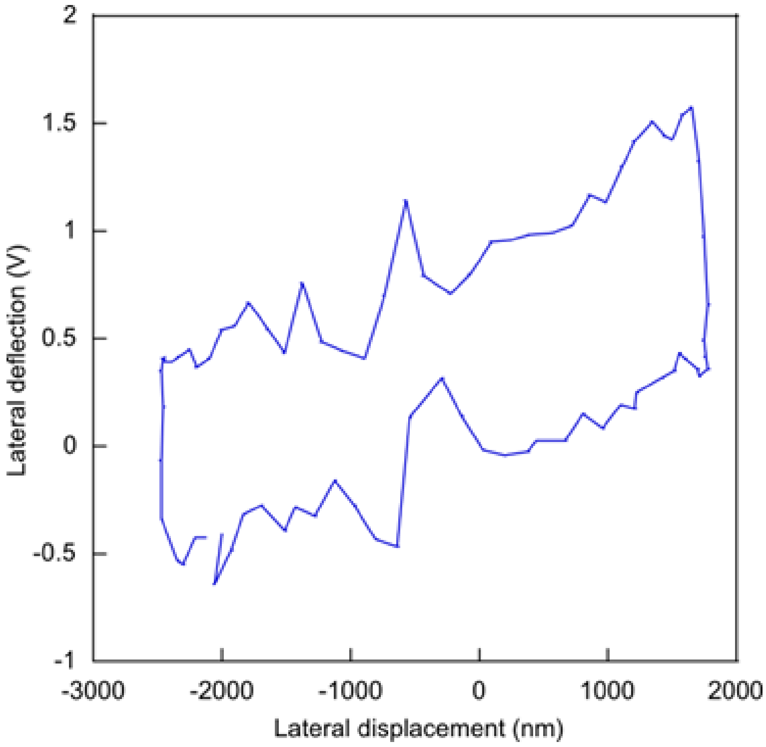

Figure 4.11: From the data of figure 4.10, lateral deflection is shown against the recorded piezo lateral output signal.

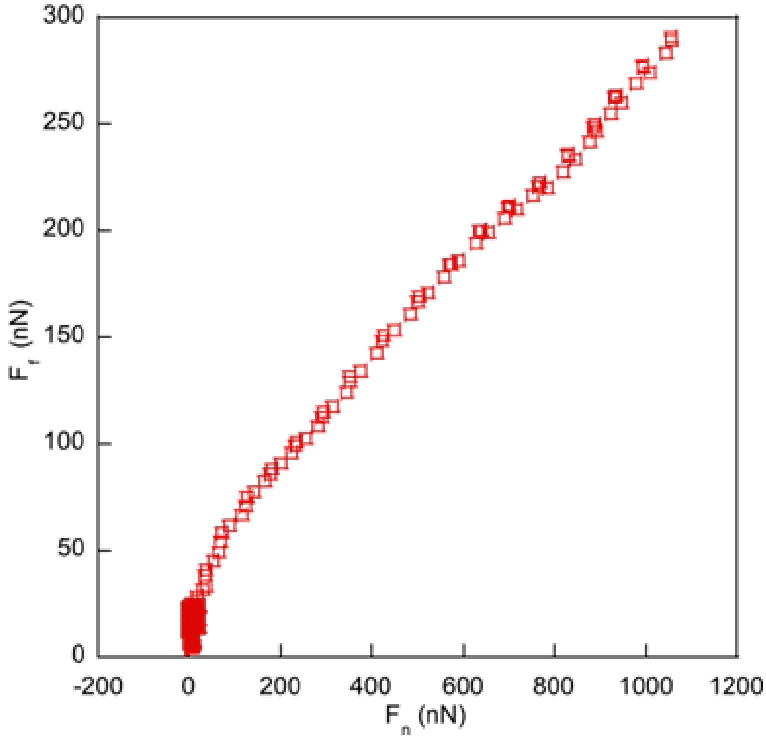

Figure 4.12: Measured frictional force is presented as function of the normal force for the working frequency of $25Hz$ and y-direction amplitude of $1.05\mu m$.

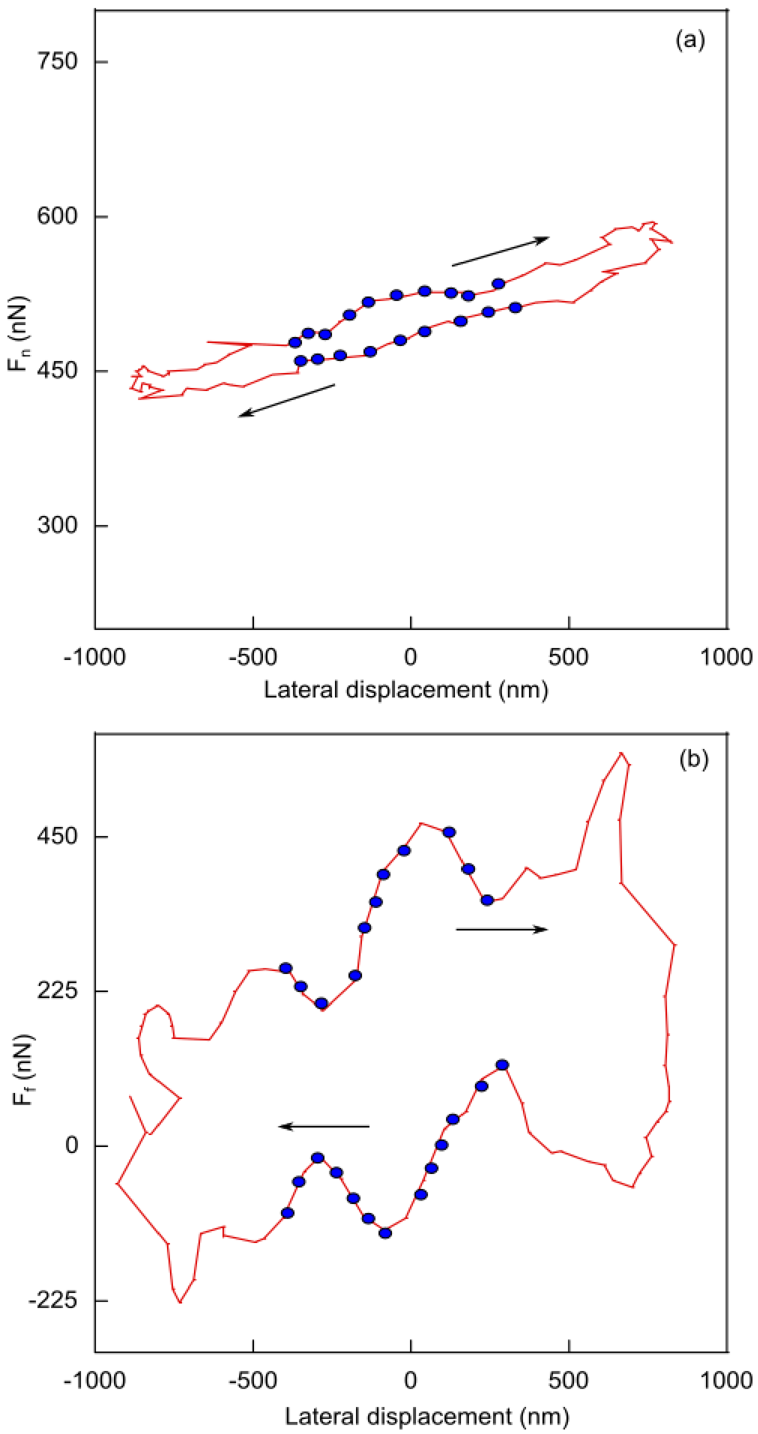

Figure 4.13: (a) The normal and (b) the frictional force variations are shown versus the lateral position of the substrate during one period of oscillation. To calculate the friction coefficient, we select the data (blue circles) for which the normal force deviates less than 10% from its mean value.

and the best fit was obtained for $L_c = 33.2nN$ and $n = 0.54$.

The different curves of the friction coefficient shown in figure 4.14 are averaged and shown in figure 4.15. We have also reported (on the same figure 4.15) the fitting of the averaged friction coefficient using equation 4.15 and also with original Brizmer model

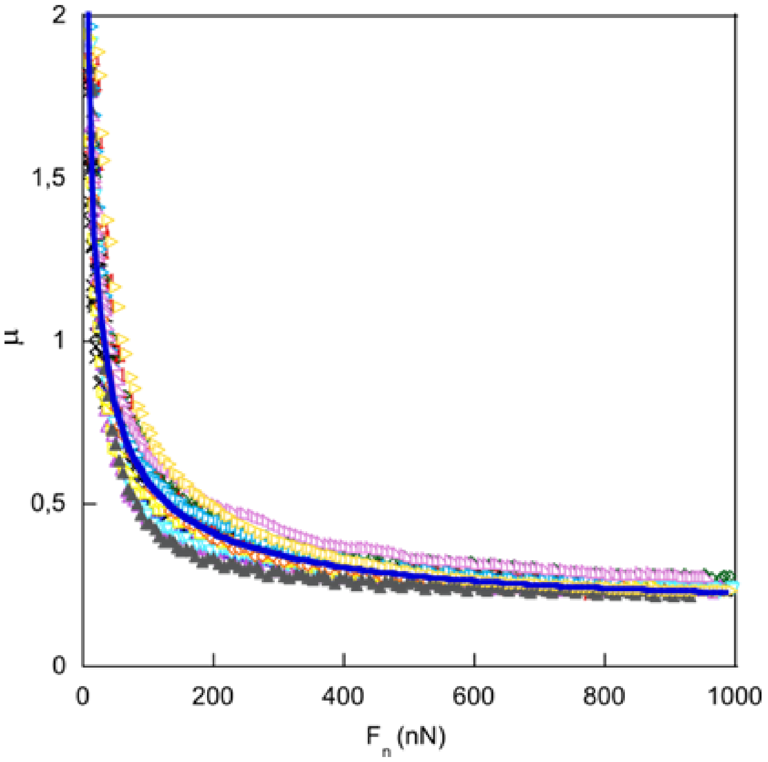

Figure 4.14: The measured friction coefficient for different particle pairs at different frequencies (25, 50 and $100Hz$) and different lateral displacement amplitudes (ranging from 600 to $2000nm$) is depicted against the normal force. The solid blue line is the mean friction coefficient averaged over all realizations.

(equation 4.13). At very small load, our experimental results are fairly in good agreement with the Brizmer model, but then Brizmer's model predicts a much slower decrease in friction coefficient in comparison to our measurements. This difference is not surprising and unexpected. As, the Brizmer's model considers an idealized contact between a plane and hemisphere, while in our case, the roughness geometry is much more complex. In addition to this, it is not necessary that the law of friction should strictly obey the Brizmer's model.

For a quantitative comparison between the microscopic friction and average rheological properties of the suspensions, it is required to obtain a relationship between inter-particle normal force and the shear stress σ. Lobry et al [52] showed that characteristic normal force that controls the friction and thus the suspension viscosity is proportional to the shear stress:

$$F_n = \frac{6\pi R^2 \sigma}{1.69} \tag{4.16}$$

The 1.69 is a rescaling factor introduced for the model to fit with constant friction coefficient simulation of Gallier et al [44].

In the upcoming section, we present the viscosity measurement in the rheometric experiment to compare it with friction coefficient measurements.

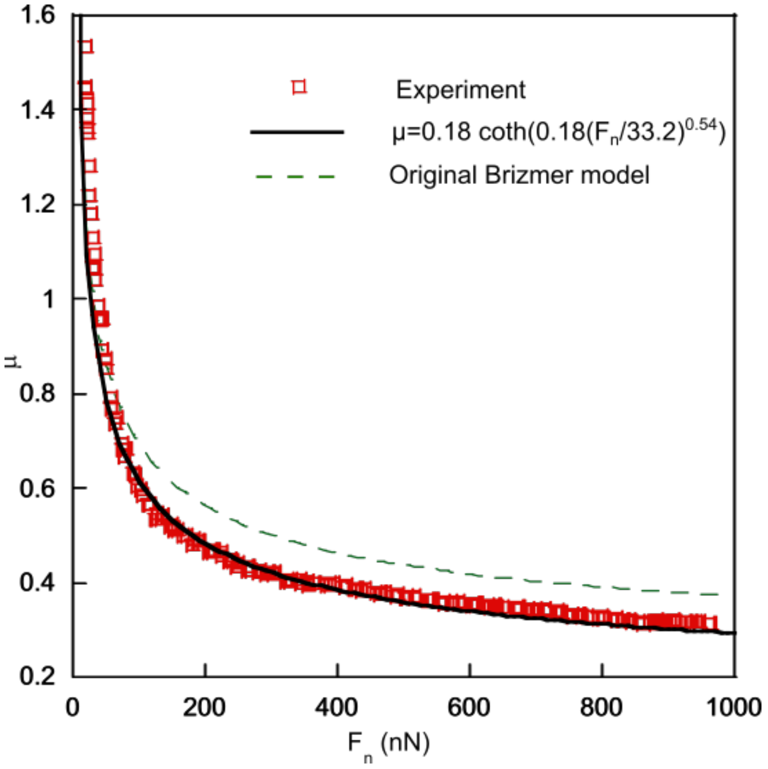

Figure 4.15: The averaged friction coefficient of polystyrene spheres as function of normal force. We fit the friction coefficient using equation 4.15 (black solid line) that gives fitting values L_c =33.2nN and n =0.54. For sake of comparison the original results of Brizmer theoretical model is also shown (dashed line).

4.4.4 Viscosity Measurement of Suspension

The viscosity of the suspension of polystyrene particles was measured for several particle volume fraction in the rheometric experiment by our collaborators (team of Elisabeth Lemaire) in InPhyNi, Universite C0te d'Azur in Nice. They prepared suspensions by suspending polystyrene particles in mixture of (water + ucon oil and zinc bromide). The mixture was made so that the density of liquid matches the density of particles, which was measured as 1045±4 $gram/cm^3$.

The viscosity of the suspension has been measured in a rotating parallel plate with the radius of the disks R=30mm and the gap height h between the two plates set to 1.2mm (see figure 4.16). The gap between the plates is equal to the diameter of 30 particles, which means we can neglect the wall structuring effect [167]. This geometry of the rotating plate provides advantages, like, there will be no migration [168] or very slow migration [169].

However, the varying shear rate over the gap is one of difficulties in using such geometry for the study of non-Newtonian materials. To account for the shear rate variation, from 0 at the center to the $\dot{\gamma}_R = \Omega R/h$ at the rim with Ω being angular velocity, the Mooney-Rabinovitch correction is used to correct the shear stress.

$$\sigma_R = \frac{\sigma_{rheo}}{4}\left(3 + \frac{d\ln\sigma_{rheo}}{d\ln\dot{\gamma}_R}\right), \tag{4.17}$$

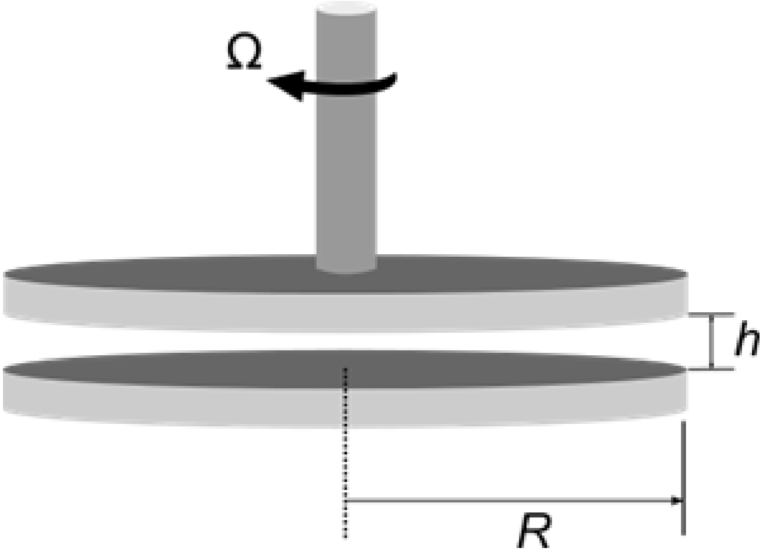

Figure 4.16: Schematic of a parallel plate rheometer. The gap between the fixed and rotating plates (of radius $R = 30mm$) is set to $h = 1.2mm$.

where $\sigma_{rheo} = 2\Gamma/\pi R^3$ with Γ being the applied torque by the rheometer. The viscosity is then obtained as:

$$\eta = \frac{\sigma_R}{\dot{\gamma}_R} \tag{4.18}$$

Viscosity is measured by imposing the stress steps whose duration varies depending upon the intensity of the stress. Indeed, the steady viscosity of the suspension is only reached when its microstructure is at equilibrium. Here, the normalized viscosity η_s is used, which is defined as the ratio of suspension viscosity to the suspending fluid viscosity.

The variation of η_s with the shear stress at different concentration (particle volume fraction) is shown in figure 4.17. The viscosity of the suspension increases as the shear stress decreases, regardless of the volume fraction value. The expression for the normalized viscosity using Lobry Model [52] is given as:

$$\eta_s = \frac{\alpha(\mu(\Sigma))}{1 - \frac{\phi}{\phi_m(\mu(\Sigma))}}. \tag{4.19}$$

Where Σ is the normalized shear stress and expressed as:

$$\Sigma = \frac{6\pi a^2 \sigma}{1.69 L_c} = \frac{F_n}{L_c}, \tag{4.20}$$

where $\alpha(\mu)$ and $\phi_m(\mu)$ are deduced from numerical simulation performed at various constant values of the friction coefficient, and are given by:

$$\begin{aligned} \alpha(\mu) &= \alpha^\infty + (\alpha^0 - \alpha^\infty)\frac{\exp(-X^\alpha \arctan\mu) - \exp(-\pi X^\alpha/2)}{1 - \exp(-\pi X^\alpha/2)} \\ \phi_m(\mu) &= \phi_m^\infty + (\phi_m^0 - \phi_m^\infty)\frac{\exp(-X^p \arctan\mu) - \exp(-\pi X^p/2)}{1 - \exp(-\pi X^p/2)} \end{aligned} \tag{4.21}$$

The normalized viscosity as function of shear stress, which is computed for different particle volume fractions using the model (equation 4.19), is presented in figure 4.17. All the rheological (fitting) parameters except for ϕ_m^0 and ϕ_m^∞ are used as same from the Lobry model [52]. The ϕ_m^0 and ϕ_m^∞ are taken here as 0.65 and 0.55 instead of 0.7 and 0.546, respectively.

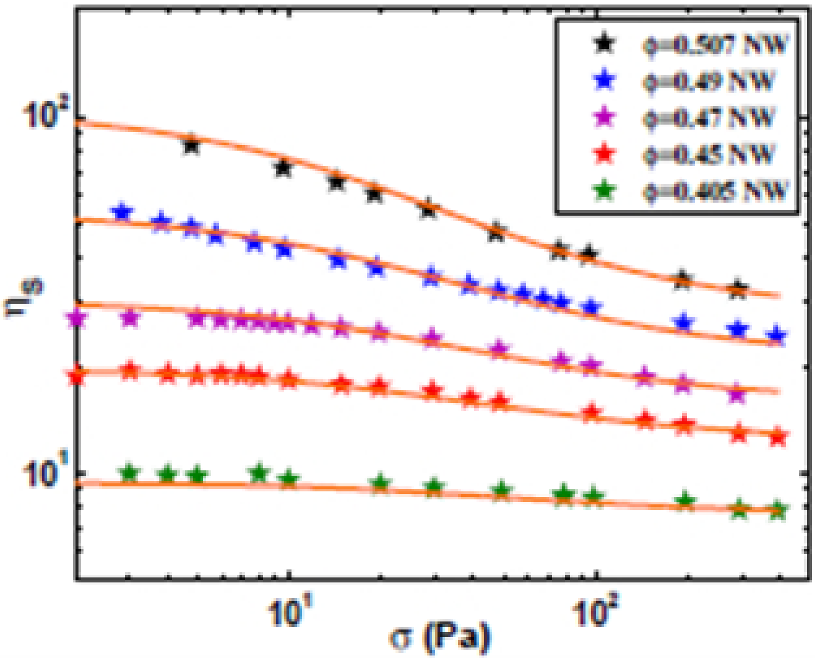

Figure 4.17: Normalized viscosity is shown as function of shear stress. The symbols represent the experimental measurements performed with suspension of polystyrene particles. The solid (orange) lines are calculations using the model (4.19) with only two free parameters are ϕ_m^0 and ϕ_m^∞. Note that viscosity data obtained for stresses that correspond to the force range in which the friction coefficient has been measured.

Figure 4.17 shows a good agreement between the experimental results and the Lobry model. This quantitative agreement predicts that the rheology of the concentrated non-Brownian suspensions is actually controlled by the frictional properties of the particles, as proposed by several authors [49,151,154]. Moreover, it validates many of hypotheses made by Lobry [52], and in particular, the choice to describe the contact between the particles by Brizmer-like mono asperity contact model. The variation of μ with F_n measured by an AFM for the normal forces of the same magnitude as experienced by particles in sheared suspensions is qualitatively close to that predicted by the Brizmer model [42]. The agreement between the experimental results and the model also shows that the rescaling factor 1.69 (in equation 4.16) used by Lobry *et al.* to link the normal force and the shear stress is the right one. In short, the numerical simulations by Lobry *et al.* carried out with constant friction coefficient have made it possible to propose fitting laws for linking the viscosity to the friction coefficient.

4.5 Conclusion and Perspective

We have presented a quantitative experimental validation of the model proposed by Lobry *et al.* [52]. This model links viscosity to the friction coefficient and, in particular, shear-thinning to the load-dependent friction coefficient. To this aim, the dynamic AFM measurements between the polystyrene microspheres is performed to determine the friction coefficient and its variation with the applied load. In order to avoid the curvature effect in the measurements of the normal and the lateral force, the amplitude of lateral displacement for particle-glued substrate (on piezo stage) is kept around a micron. The measured friction coefficient is observed to decrease with the increasing load and reaches a plateau at the sufficiently high load, which is contrary to the constant friction coefficient usually observed for the macroscopic contacts. This behavior suggests that the actual contact between the two microspheres involves small number of the asperities, as proposed by mono-asperity contact model. We have observed a slight disparity when the measured friction coefficient is compared to the scenario proposed by Brizmer *et al.* [42]. This lack of correspondence may be explained by the fact that the topography of the surface is more complicated than the ideal hemisphere considered by Brizmer *et al.*. Nonetheless, our measurements display same trend like mono-asperity contact model, so we have fitted the measured friction coefficient with a Brizmer-like model.

Lobry model is used to compare the measured friction coefficient (AFM measurements) and the viscosity measurements (rheometeric experiment). A correlation is observed between the decrease in the friction coefficient and decrease in the viscosity, which unambiguously validate the scenario proposed by the Lobry *et al.*. This also highlights a close link between the microscopic friction properties of the particles and the macroscopic rheological behavior of the suspension. To conclude with the fact that this is an effective and accurate methodology, which quantitatively predicts the rheology of the moderately concentrated NB suspension from the microscopic contact law.

Our measurements bridge the nano and macro scale measurements and open a broad perspective by highlighting the importance of the local interactions in the understanding of the overall rheological behaviors of the suspensions. Keeping in view the fact that the friction between the particles is greatly influenced by the intrinsic properties of the materials (such as its viscoelastic properties), the idea of reproducing this work with the particles of different materials to validate the scenario mentioned in this chapter would be interesting. A step further, it would be particularly relevant for soft materials where the viscoelastic mechanical effects dominate the friction between the materials. Since the nanoscale friction in soft surfaces (such as biological and soft polymeric interfaces) with relevant modulus offers excellent opportunities for future interdisciplinary research to tackle a variety of global challenges including the reduction in energy consumption to the biological tissue repair.

In addition to the viscoelasticity, the surface chemistry and topographies are crucial factors to interpret the surface tribology. To this aim, we project to perform the friction measurements between the particles having particular surface properties, such as the surface is electrically charged or grafted with some polymer brushes, to explore new aspects.

The fluid flows around the interacting particles is another intricate subject, which has attracted the researcher due to their wide occurrence and applications. In our experiment, we added Ucon oil in to water to increase the viscosity of the suspending fluid. This allowed us to perform the rheology measurements over a wide range of shear stress and still have a low Reynold number. However, it is more likely that all or part of the surfactant gets removed during the washing of the particles. The particles are then possibly subject to the adhesive force, which we have observed in AFM measurements. This leads us to another aspect for the future studies where for the case of adhesive suspension, it would be interesting to characterize the adhesion forces and establish a quantitative link between the adhesion (characterized using an AFM) and rheology (stress threshold, shear-thinning).

General Conclusion

This thesis work has been accomplished in to two parts. In the first part, We have studied the elastohydrodynamic coupling between a vibrating colloidal probe and a soft PDMS substrate using the dynamic AFM and we have extracted the rheological properties of the soft PDMS sample. In the second part, we have performed lateral force measurement to extract the friction coeffcient and AFM imaging to extract the roughness profile of polystyrene microspheres.

In AFM-based experiments a cantilever (probe) is used to sense the sample surface. An accurate calibration of the AFM cantilever is the primary requirement for the quantitative and comprehensive AFM studies. The hydrodynamic drag technique has been used for the vertical and the lateral calibrations of the colloidal probe. It allows determination of the spring constant of the cantilever in a viscous liquid by measuring the deflection (for the vertical calibration) and the twist (for the lateral calibration) of the cantilever. In the former case, the normal spring constant of the cantilever was obtained by measuring the deflection for a known hydrodynamic drag force on the colloidal probe, which was approaching the substrate perpendicularly. In the case of the lateral force calibration, a laterally moving substrate generated a creeping Couette flow and as a result induced a torsion of the AFM probe. The spherical geometry of the colloidal probe enabled the analytical calculation of the drag force and torque exerted on the probe. Fitting the measured lateral signal with the analytical expression of the calculated torque gave the lateral force conversion factor.

In first part of the thesis, the viscoelastic rheological properties of thin polymer films were obtained using non-contact AFM technique at different excitation frequencies. The experiments were carried out in a liquid using the colloidal AFM in dynamic mode. The dynamic colloidal AFM method allows to probe the elastohydrodynamic interaction at nanoscale for a large range of vibration frequencies. The nanoscale flow induced by the oscillation of the colloidal probe provides a hydrodynamic force acting on the film. The force response obtained as function of the distance displays a power law regime: at large distance the response is dominated by the viscous damping and it scales as $1/D$; The compliance of the elastomer appears through a small elastic contribution in the mechanical impedance and it scales as $1/D^{5/2}$. As the gap distance is reduced both viscous and elastic contributions increases and saturate to constant values at very small tip-sample separations. From the measured mechanical response, we have obtained the storage and loss moduli of the thin film. The experimental results were in a qualitative agreement with the simplified spring-dashpot model. A discrepancy was observed between the experimental findings and simple model at small distance. Therefore, a numerical solution of a viscoelastic soft-lubrication model was derived. The experimental results shown good agreement with the numerical calculations, which allowed us to measure the storage and loss moduli for a broad range of frequencies. The measured moduli versus the frequency showed a good agreement with the Chasset-Thirion model. In order to validate our measurements, we have also performed a force-indentation measurement to extract the value of the Young's modulus (E_0) of the sample, which was comparable to the outcomes of the dynamic mode measurements. In short, this contactless technique is a relevant alternative to direct contact techniques for the study of viscoelastic properties of soft and fragile samples including nanobubbles, lives cell and tissues.

The second part of the thesis aimed to understand and provide a quantitative link between the microscopic (frictional) properties of microparticles and the macroscopic behavior of suspensions made of these particles. For this purpose, we performed experiments for the quantitative measurement of friction between polystyrene microparticles by measuring the deflection and the twist produced in the colloidal probe using the dynamic AFM method. We have measured the friction coefficient for different values of applied normal force (varied from 10 to $1000nN$). The friction coefficient has been observed to decrease with an increasing load, which is contrary to usual constant behavior for the case of contacting macroscopic bodies. This behavior suggests that the contact between the particles involves a small number of asperities and shows the same trend as the one explained by the mono-asperity contact model. At small load, the friction coefficient decreases and reaches a plateau at high load. It is basically a transition from the fully elastic to plastic contacts marked by the characteristic force L_c. This decrease in friction coefficient makes it possible to accurately describe the shear-thinning phenomena observed in rheological measurements.

The correlation between the decrease in friction coefficient (measured using an AFM) and decrease in viscosity (measured in rheometric experiment) unambiguously support the scenario proposed by Lobry. It also highlights the close link between the microscopic friction properties of the particles and macroscopic rheological behavior of the suspension. This led to the conclusion that Lobry's model is an effective mechanism, which quantitatively predict the rheology of moderately concentrated non-Brownian suspensions from the microscopic contact law.

In short, all the measurements are evidence to the fact that the dynamic colloidal AFM technique is a powerful tool to study the surface properties in a confined geometry.

As a perspective for the viscoelastic measurements, we project to extend the work to viscoelastic characterization of the PDMS with various cross-linked densities. However, a single model with a finite number of parameters for the viscoelastic samples cannot describe the behavior of all materials due to different relaxation mechanisms at different frequency scales. The Chasset-Thirion model, which was developed for the frequency response of the soft gel, might fail to capture the frequency response of the PDMS substrates with higher cross-linked densities. That is for, we also project to derive a theoretical model to fit the extracted storage and loss moduli for those samples to obtain their rheological properties at wide range of excitation frequencies. Nonetheless, the broader aspect of applications of this study provide a strong motivation for the study of hydrodynamic interaction between soft and fragile samples.

As a perspective of our investigation of friction between the polystyrene microspheres, we project to reproduce this experiment with the particles of different materials. As, the friction between the particles is greatly influenced by the intrinsic properties (such as its viscoelastic properties) of the materials, so the idea of reproducing this work with the particles of different materials to validate the scenario would be interesting. A step further, it would be particularly relevant for soft materials where the viscoelastic mechanical effects dominate the friction between the materials. In addition to this, the surface chemistry and topographies are crucial factors to interpret the surface tribology. To this aim, the friction measurements between the particles having particular surface properties, such as the surface is electrically charged or grafted with some polymer brushes, would be interesting. Lastly, for the case of adhesive suspension, it would be interesting to characterize the adhesion forces and establish a quantitative link between the adhesion (characterized using an AFM) and rheology (stress threshold, shear-thinning).

Bibliography

[1] Bocquet Lydéric and E Charlaix. Nanofluidics from bulk to interfaces. *Chem. Soc. Rev*, 3:1073–1095, 2010.

[2] Lydéric Bocquet. Nanofluidics coming of age. *Nature materials*, 19(3):254–256, 2020.

[3] Takahiro Shimada, Kenji Ouchi, Yuu Chihara, and Takayuki Kitamura. Breakdown of continuum fracture mechanics at the nanoscale. *Scientific reports*, 5(1):1–6, 2015.

[4] Lydéric Bocquet and Jean-Louis Barrat. Flow boundary conditions from nano-to micro-scales. *Soft matter*, 3(6):685–693, 2007.

[5] Nikita Kavokine, Roland R Netz, and Lydéric Bocquet. Fluids at the nanoscale: From continuum to subcontinuum transport. *Annual Review of Fluid Mechanics*, 53:377–410, 2021.

[6] Lydéric Bocquet and Jean-Louis Barrat. On the green-kubo relationship for the liquid-solid friction coefficient. *The Journal of chemical physics*, 139(4):044704, 2013.

[7] W. Ducker, T. Senden, and R. Pashley. Direct measurement of colloidal forces using an atomic force microscope. *Nature*, 1991.

[8] Andreas Mark, Nicolas Helfricht, Astrid Rauh, Matthias Karg, and Georg Papastavrou. The next generation of colloidal probes: A universal approach for soft and ultra-small particles. *Small*, 15(43):1902976, 2019.

[9] Matteo Chighizola, Luca Puricelli, Ludovic Bellon, and Alessandro Podestà. Large colloidal probes for atomic force microscopy: Fabrication and calibration issues. *Journal of Molecular Recognition*, 34(1):e2879, 2021.

[10] Donna C Hurley, Malgorzata Kopycinska-Mueller, and AB Kos. Mapping mechanical properties on the nanoscale using atomic-force acoustic microscopy. *Jom*, 59(1):23–29, 2007.

[11] Marija Plodinec and Roderick YH Lim. Nanomechanical characterization of living mammary tissues by atomic force microscopy. In *Mammary Stem Cells*, pages 231–246. Springer, 2015.

[12] Pranjal Nautiyal, Fahad Alam, Kantesh Balani, and Arvind Agarwal. The role of nanomechanics in healthcare. *Advanced healthcare materials*, 7(3):1700793, 2018.

[13] Alexandre Dazzi, Craig B Prater, Qichi Hu, D Bruce Chase, John F Rabolt, and Curtis Marcott. Afm–ir: combining atomic force microscopy and infrared spectroscopy for nanoscale chemical characterization. *Applied spectroscopy*, 66(12):1365–1384, 2012.

[14] Sergei V Kalinin and Alexei Gruverman. *Scanning probe microscopy: electrical and electromechanical phenomena at the nanoscale*, volume 1. Springer Science & Business Media, 2007.

[15] Rachel A Oliver. Advances in afm for the electrical characterization of semiconductors. *Reports on Progress in Physics*, 71(7):076501, 2008.

[16] Hans-Jürgen Butt, Brunero Cappella, and Michael Kappl. Force measurements with the atomic force microscope: Technique, interpretation and applications. *Surface Science Reports*, 59(1):1–152, 2005.

[17] Dalia G Yablon. *Scanning Probe Microscopy¿ in Industrial Applications: Nanomechanical Characterization.* John Wiley & Sons, 2013.

[18] Ricardo Garcia. Nanomechanical mapping of soft materials with the atomic force microscope: methods, theory and applications. *Chemical Society Reviews*, 49(16):5850–5884, 2020.

[19] Frédéric Restagno, Jérôme Crassous, Elisabeth Charlaix, Cécile Cottin-Bizonne, and Michel Monchanin. A new surface forces apparatus for nanorheology. *Review of scientific instruments*, 73(6):2292–2297, 2002.

[20] Samuel Leroy and Elisabeth Charlaix. Hydrodynamic interactions for the measurement of thin film elastic properties. *Journal of Fluid Mechanics*, 674:389, 2011.

[21] Samuel Leroy, Audrey Steinberger, Cécile Cottin-Bizonne, Frédéric Restagno, Liliane Léger, and Élisabeth Charlaix. Hydrodynamic interaction between a spherical particle and an elastic surface: a gentle probe for soft thin films. *Physical review letters*, 108(26):264501, 2012.

[22] Farzaneh Kaveh, Javed Ally, Michael Kappl, and Hans-Jurgen Butt. Hydrodynamic force between a sphere and a soft, elastic surface. *Langmuir*, 30(39):11619–11624, 2014.

[23] Léo Garcia, Chloé Barraud, Cyril Picard, Jérôme Giraud, Elisabeth Charlaix, and Benjamin Cross. A micro-nano-rheometer for the mechanics of soft matter at interfaces. *Review of Scientific Instruments*, 87(11):113906, 2016.

[24] Pratyaksh Karan, Jeevanjyoti Chakraborty, and Suman Chakraborty. Small-scale flow with deformable boundaries. *Journal of the Indian Institute of Science*, 98(2):159–183, 2018.

[25] ZM Jin and D Dowson. Elastohydrodynamic lubrication in biological systems. *Proceedings of the Institution of Mechanical Engineers, Part J: Journal of Engineering Tribology*, 219(5):367–380, 2005.

[26] Yumo Wang, Georgia A Pilkington, Charles Dhong, and Joelle Frechette. Elastic deformation during dynamic force measurements in viscous fluids. *Current opinion in colloid & interface science*, 27:43–49, 2017.

[27] Thomas Salez and Lakshminarayanan Mahadevan. Elastohydrodynamics of a sliding, spinning and sedimenting cylinder near a soft wall. *Journal of Fluid Mechanics*, 779:181–196, 2015.

[28] Javier Urzay, Stefan G Llewellyn Smith, and Beverley J Glover. The elastohydrodynamic force on a sphere near a soft wall. *Physics of Fluids*, 19(10):103106, 2007.

[29] Zaicheng Zhang, Vincent Bertin, Muhammad Arshad, Elie Raphael, Thomas Salez, and Abdelhamid Maali. Direct measurement of the elastohydrodynamic lift force at the nanoscale. *Physical review letters*, 124(5):054502, 2020.

[30] Randy H Ewoldt, AE Hosoi, and Gareth H McKinley. New measures for characterizing nonlinear viscoelasticity in large amplitude oscillatory shear. *Journal of Rheology*, 52(6):1427–1458, 2008.

[31] JF Vega, A Santamaria, A Munoz-Escalona, and P Lafuente. Small-amplitude oscillatory shear flow measurements as a tool to detect very low amounts of long chain branching in polyethylenes. *Macromolecules*, 31(11):3639–3647, 1998.

[32] Menghua Zhao, Julien Dervaux, Tetsuharu Narita, François Lequeux, Laurent Limat, and Matthieu Roché. Geometrical control of dissipation during the spreading of liquids on soft solids. *Proceedings of the National Academy of Sciences*, 115(8):1748–1753, 2018.

[33] Prathima C Nalam, Nitya N Gosvami, Matthew A Caporizzo, Russell J Composto, and Robert W Carpick. Nano-rheology of hydrogels using direct drive force modulation atomic force microscopy. *Soft Matter*, 11(41):8165–8178, 2015.

[34] Yuri M Efremov, Takaharu Okajima, and Arvind Raman. Measuring viscoelasticity of soft biological samples using atomic force microscopy. *Soft matter*, 16(1):64–81, 2020.

[35] Enrique A López-Guerra and Santiago D Solares. On the frequency dependence of viscoelastic material characterization with intermittent-contact dynamic atomic force microscopy: avoiding mischaracterization across large frequency ranges. *Beilstein Journal of Nanotechnology*, 11(1):1409–1418, 2020.

[36] F. P. Dowson and D. Tabor. *The Frictions and Lubrication of Solids.* Oxford University Press, 1950.

[37] F.P Bowden and D. Tabor. Mechanism of Metallic Friction. *Nature*, 150(3798):197–199, 1942.

[38] Yifei Mo, Kevin T Turner, and Izabela Szlufarska. Friction laws at the nanoscale. *Nature*, 457(7233):1116–1119, 2009.

[39] James L Bosse, Sungjun Lee, Andreas Sø Andersen, Duncan S Sutherland, and Bryan D Huey. High speed friction microscopy and nanoscale friction coefficient mapping. *Measurement Science and Technology*, 25(11):115401, 2014.

[40] C Mathew Mate, Gary M McClelland, Ragnar Erlandsson, and Shirley Chiang. Atomic-scale friction of a tungsten tip on a graphite surface. pages 226–229, 1987.

[41] K.L. Johnson, K. Kendall, and A.D. Roberts. Surface energy and the contact of elastic solids. *Proceedings of the Royal Society of London Series A*, 324(1558):301–313, 1971.

[42] Victor Brizmer, Yuri Kligerman, and I. Etsion. Elastic–plastic spherical contact under combined normal and tangential loading in full stick. *Tribology Letters*, 25:61–70, 01 2007.

[43] V Brizmer, Y Kligerman, and I Etsion. The effect of contact conditions and material properties on the elasticity terminus of a spherical contact. *International journal of solids and structures*, 43(18-19):5736–5749, 2006.

[44] Stany Gallier, Elisabeth Lemaire, François Peters, and Laurent Lobry. Rheology of sheared suspensions of rough frictional particles. *Journal of Fluid Mechanics*, 757:514–549, 2014.

[45] Francois Peters, Giovanni Ghigliotti, Stany Gallier, Frederic Blanc, Elisabeth Lemaire, and Laurent Lobry. Rheology of non-brownian suspensions of rough frictional particles under shear reversal: A numerical study. *Journal of rheology*, 60(4):715–732, 2016.

[46] William Chèvremont, Bruno Chareyre, and Hugues Bodiguel. Quantitative study of the rheology of frictional suspensions: Influence of friction coefficient in a large range of viscous numbers. *Physical Review Fluids*, 4(6):064302, 2019.

[47] M. Wyart and M. E. Cates. Discontinuous shear thickening without inertia in dense non-brownian suspensions. *Physical Review Letter*, 112:098302, 2014.

[48] Jean Comtet, Guillaume Chatté, Antoine Niguès, Lydéric Bocquet, Alessandro Siria, and Annie Colin. Pairwise frictional profile between particles determines discontinuous shear thickening transition in non-colloidal suspensions. *Nature Communications*, 8:15633, 2017.

[49] Guillaume Chatté, Jean Comtet, Antoine Niguès, Lydéric Bocquet, Alessandro Siria, Guylaine Ducouret, François Lequeux, Nicolas Lenoir, Guillaume Ovarlez, and Annie Colin. Shear thinning in non-brownian suspensions. *Soft matter*, 14(6):879–893, 2018.

[50] Ryohei Seto, Romain Mari, Jeffrey F. Morris, and Morton M. Denn. Discontinuous shear thickening of frictional hard-sphere suspensions. *Physical Review Letter*, 111:218301, 2013.

[51] Romain Mari, Ryohei Seto, Jeffrey Morris, and Morton Denn. Shear thickening, frictionless and frictional rheologies in non-brownian suspensions. *Journal of Rheology*, 58:1693–1724, 09 2014.

[52] Laurent Lobry, Elisabeth Lemaire, Frédéric Blanc, Stany Gallier, and François Peters. Shear thinning in non-brownian suspensions explained by variable friction between particles. *Journal of Fluid Mechanics*, 860:682–710, 2019.

[53] Gerd Binnig, Heinrich Rohrer, Ch Gerber, and Edmund Weibel. Surface studies by scanning tunneling microscopy. *Physical review letters*, 49(1):57–61, 1982.

[54] Gerd Binnig, Heinrich Rohrer, Ch Gerber, and Eduard Weibel. 7× 7 reconstruction on si (111) resolved in real space. *Physical review letters*, 50(2):120, 1983.

[55] G. Binnig, C. F. Quate, and Ch. Gerber. Atomic force microscope. *Phys. Rev. Lett.*, 56:930–933, 1986.

[56] DY Abramovitch, SB Andersson, LY Pao, and G Schitter. A tutorial on the mechanisms, dynamics, and control of atomic force microscopes, in ‘american control conference. *New York City, USA*, 2007.

[57] Kristina Haase and Andrew E Pelling. Investigating cell mechanics with atomic force microscopy. *Journal of The Royal Society Interface*, 12(104):20140970, 2015.

[58] Daniel J Müller and Yves F Dufrêne. Atomic force microscopy: a nanoscopic window on the cell surface. *Trends in cell biology*, 21(8):461–469, 2011.

[59] Gerhard Meyer and Nabil M Amer. Novel optical approach to atomic force microscopy. *Applied physics letters*, 53(12):1045–1047, 1988.

[60] Yves F Dufrêne, Toshio Ando, Ricardo Garcia, David Alsteens, David Martinez-Martin, Andreas Engel, Christoph Gerber, and Daniel J Müller. Imaging modes of atomic force microscopy for application in molecular and cell biology. *Nature nanotechnology*, 12(4):295–307, 2017.

[61] Robert W Stark, Georg Schitter, Martin Stark, Reinhard Guckenberger, and Andreas Stemmer. State-space model of freely vibrating and surface-coupled cantilever dynamics in atomic force microscopy. *Physical Review B*, 69(8):085412, 2004.

[62] Nader Jalili and Karthik Laxminarayana. A review of atomic force microscopy imaging systems: application to molecular metrology and biological sciences. *Mechatronics*, 14(8):907–945, 2004.

[63] TR Albrecht, Pr Grütter, D Horne, and Do Rugar. Frequency modulation detection using high-q cantilevers for enhanced force microscope sensitivity. *Journal of applied physics*, 69(2):668–673, 1991.

[64] Ricardo Garcıa and Ruben Perez. Dynamic atomic force microscopy methods. *Surface science reports*, 47(6-8):197–301, 2002.

[65] S. Morita, F.J. Giessibl, and R. Wiesendanger. *Noncontact Atomic Force Microscopy: Volume 2*. Springer Berlin Heidelberg, 2009.

[66] Jean Comtet. *Rheology and tribology at the nanoscale*. PhD thesis, 2019.

[67] Toshio Ando, Takayuki Uchihashi, and Noriyuki Kodera. High-speed afm and applications to biomolecular systems. *Annual Review of Biophysics*, 42(1):393–414, 2013.

[68] Takayuki Uchihashi, Hiroki Watanabe, Shingo Fukuda, Mikihiro Shibata, and Toshio Ando. Functional extension of high-speed afm for wider biological applications. *Ultramicroscopy*, 160:182–196, 2016.

[69] Michal Hrouzek. *Modélisation, estimation et contrôle de Microscope á Force Atomique*. PhD thesis, 2007.

[70] Brunero Cappella. *Physical Principles of Force–Distance Curves by Atomic Force Microscopy*, pages 3–66. Springer International Publishing, Cham, 2016.

[71] M Tortonese, RC Barrett, and CF Quate. Atomic resolution with an atomic force microscope using piezoresistive detection. *Applied physics letters*, 62(8):834–836, 1993.

[72] S Akamine, RC Barrett, and CF Quate. Improved atomic force microscope images using microcantilevers with sharp tips. *Applied Physics Letters*, 57(3):316–318, 1990.

[73] O Wolter, Th Bayer, and J Greschner. Micromachined silicon sensors for scanning force microscopy. *Journal of Vacuum Science & Technology B: Microelectronics and Nanometer Structures Processing, Measurement, and Phenomena*, 9(2):1353–1357, 1991.

[74] H. J. Butt. Measuring electrostatic, van der waals, and hydration forces in electrolyte solutions with an atomic force microscope. *Biophysical journal*, 60(6):1438–1444, 1991.

[75] Bärbel Lorenz, Rabea Keller, Eva Sunnick, Burkhard Geil, and Andreas Janshoff. Colloidal probe microscopy of membrane–membrane interactions: From ligand–receptor recognition to fusion events. *Biophysical chemistry*, 150(1-3):54–63, 2010.

[76] Koo-Hyun Chung, Gordon A Shaw, and Jon R Pratt. Accurate noncontact calibration of colloidal probe sensitivities in atomic force microscopy. *Review of Scientific Instruments*, 80(6):065107, 2009.

[77] H Li, Y Xu, M Shao, L Guo, and D An. Analysis for hysteresis of piezoelectric actuator based on microscopic mechanism. In *IOP Conference Series: Materials Science and Engineering*, volume 399, page 012031. IOP Publishing, 2018.

[78] Martin Munz. Force calibration in lateral force microscopy: a review of the experimental methods. *Journal of Physics D: Applied Physics*, 43(6):063001, 2010.

[79] Manuel LB Palacio and Bharat Bhushan. Normal and lateral force calibration techniques for afm cantilevers. *Critical Reviews in Solid State and Materials Sciences*, 35(2):73–104, 2010.

[80] TH Stievater, WS Rabinovich, HS Newman, R Mahon, PG Goetz, JL Ebel, and DJ McGee. Measurement of thermal-mechanical noise in microelectromechanical systems. *Applied physics letters*, 81(10):1779–1781, 2002.

[81] MV Salapaka, HS Bergh, J Lai, A Majumdar, and E McFarland. Multi-mode noise analysis of cantilevers for scanning probe microscopy. *Journal of Applied Physics*, 81(6):2480–2487, 1997.

[82] Mircea Rades. Mechanical vibrations. *Publishing Printech Bucharest*, 2008.

[83] John Elie Sader. Frequency response of cantilever beams immersed in viscous fluids with applications to the atomic force microscope. *Journal of Applied Physics*, 84(1):64–76, 1998.

[84] Abdelhamid Maali, Cedric Hurth, Rodolphe Boisgard, Cédric Jai, Touria Cohen-Bouhacina, and Jean-Pierre Aimé. Hydrodynamics of oscillating atomic force microscopy cantilevers in viscous fluids. *Journal of Applied Physics*, 97(7):074907, 2005.

[85] A Maali, T Cohen-Bouhacina, C Jai, C Hurth, R Boisgard, JP Aimé, D Mariolle, and F Bertin. Reduction of the cantilever hydrodynamic damping near a surface by ion-beam milling. *Journal of applied physics*, 99(2):024908, 2006.

[86] Christopher P. Green, Hadi Lioe, Jason P. Cleveland, Roger Proksch, Paul Mulvaney, and John E. Sader. Normal and torsional spring constants of atomic force microscope cantilevers. *Review of Scientific Instruments*, 75(6):1988–1996, 2004.

[87] H. J. Butt and M. Jaschke. Calculation of thermal noise in atomic force microscopy. *Nanotechnology*, 6(1):1–7, 1995.

[88] B.D. Hauer, C. Doolin, K.S.D. Beach, and J.P. Davis. A general procedure for thermomechanical calibration of nano/micro-mechanical resonators. *Annals of Physics*, 339:181–207, 2013.

[89] U. Rabe and W. Arnold. Acoustic microscopy by atomic force microscopy. *Applied Physics Letters*, 64(12):1493–1495, 1994.

[90] John E. Sader, Ian Larson, Paul Mulvaney, and Lee R. White. Method for the calibration of atomic force microscope cantilevers. *Review of Scientific Instruments*, 66(7):3789–3798, 1995.

[91] Charles A Clifford and Martin P Seah. The determination of atomic force microscope cantilever spring constants via dimensional methods for nanomechanical analysis. *Nanotechnology*, 16(9):1666–1680, 2005.

[92] H.-J. Butt, P. Siedle, K. Seifert, K. Fendler, T. Seeger, E. Bamberg, A. L. Weisenhorn, K. Goldie, and A. Engel. Scan speed limit in atomic force microscopy. *Journal of Microscopy*, 169(1):75–84, 1993.

[93] John Elie Sader and Lee White. Theoretical analysis of the static deflection of plates for atomic force microscope applications. *Journal of Applied Physics*, 74(1):1–9, 1993.

[94] J. P. Cleveland, S. Manne, D. Bocek, and P. K. Hansma. A nondestructive method for determining the spring constant of cantilevers for scanning force microscopy. *Review of Scientific Instruments*, 64(2):403–405, 1993.

[95] Dmytro S. Golovko, Thomas Haschke, Wolfgang Wiechert, and Elmar Bonaccurso. Nondestructive and noncontact method for determining the spring constant of rectangular cantilevers. *Review of Scientific Instruments*, 78(4):043705, 2007.

[96] Jeffrey L. Hutter. Calibration of afm cantilever. 2005.

[97] John E. Sader, James W. M. Chon, and Paul Mulvaney. Calibration of rectangular atomic force microscope cantilevers. *Review of Scientific Instruments*, 70(10):3967–3969, 1999.

[98] Sudipta Basak, Arvind Raman, and Suresh V Garimella. Hydrodynamic loading of microcantilevers vibrating in viscous fluids. *Journal of Applied Physics*, 99(11):114906, 2006.

[99] EO Tuck. Calculation of unsteady flows due to small motions of cylinders in a viscous fluid. *Journal of Engineering Mathematics*, 3(1):29–44, 1969.

[100] S Rast, C Wattinger, U Gysin, and E Meyer. The noise of cantilevers. *Nanotechnology*, 11(3):169, 2000.

[101] Jannis Lübbe, Matthias Temmen, Philipp Rahe, Angelika Kühnle, and Michael Reichling. Determining cantilever stiffness from thermal noise. *Beilstein journal of nanotechnology*, 4(1):227–233, 2013.

[102] Vincent SJ Craig and Chiara Neto. In situ calibration of colloid probe cantilevers in force microscopy: hydrodynamic drag on a sphere approaching a wall. *Langmuir*, 17(19):6018–6022, 2001.

[103] Olga I Vinogradova. Drainage of a thin liquid film confined between hydrophobic surfaces. *Langmuir*, 11(6):2213–2220, 1995.

[104] Howard Brenner. The slow motion of a sphere through a viscous fluid towards a plane surface. *Chemical engineering science*, 16(3-4):242–251, 1961.

[105] Christopher DF Honig and William A Ducker. No-slip hydrodynamic boundary condition for hydrophilic particles. *Physical review letters*, 98(2):028305, 2007.

[106] Martin Munz. Force calibration in lateral force microscopy: a review of the experimental methods. *Journal of Physics D: Applied Physics*, 43(6):063001, 2010.

[107] Roderic Lakes. Advances in negative poisson's ratio materials. *Advanced Materials*, 5(4):293–296, 1993.

[108] Christopher P Green and John E Sader. Torsional frequency response of cantilever beams immersed in viscous fluids with applications to the atomic force microscope. *Journal of applied physics*, 92(10):6262–6274, 2002.

[109] K. Gieck and R. Gieck. *Engineering Formulas*. McGraw-Hill New York, 1997.

[110] Nic Mullin and Jamie K Hobbs. A non-contact, thermal noise based method for the calibration of lateral deflection sensitivity in atomic force microscopy. *Review of Scientific Instruments*, 85(11):113703, 2014.

[111] Sangjin Ryu and Christian Franck. In situ hydrodynamic lateral force calibration of afm colloidal probes. *Langmuir*, 27(21):13390–13399, 2011.

[112] Arthur Joseph Goldman, Raymond G Cox, and Howard Brenner. Slow viscous motion of a sphere parallel to a plane wall—i motion through a quiescent fluid. *Chemical engineering science*, 22(4):637–651, 1967.

[113] Arthur Joseph Goldman, Raymond G Cox, and Howard Brenner. Slow viscous motion of a sphere parallel to a plane wall-ii couette flow. *Chemical engineering science*, 22(4):653–660, 1967.

[114] Ivan U Vakarelski, Raymond R Dagastine, Derek YC Chan, Geoffrey W Stevens, Ko Higashitani, and Franz Grieser. Lateral hydrodynamic interactions between an emulsion droplet and a flat surface evaluated by frictional force microscopy. *Langmuir*, 26(11):8002–8007, 2010.

[115] ID Johnston, DK McCluskey, CKL Tan, and MC Tracey. Mechanical characterization of bulk sylgard 184 for microfluidics and microengineering. *Journal of Micromechanics and Microengineering*, 24(3):035017, 2014.

[116] Jessamine Ng Lee, Cheolmin Park, and George M Whitesides. Solvent compatibility of poly (dimethylsiloxane)-based microfluidic devices. *Analytical chemistry*, 75(23):6544–6554, 2003.

[117] M Heuberger. The extended surface forces apparatus. part i. fast spectral correlation interferometry. *Review of Scientific Instruments*, 72(3):1700–1707, 2001.

[118] Manoj K Chaudhury and George M Whitesides. Correlation between surface free energy and surface constitution. *Science*, 255(5049):1230–1232, 1992.

[119] Daniele Passeri, Marco Rossi, Emanuela Tamburri, and Maria Letizia Terranova. Mechanical characterization of polymeric thin films by atomic force microscopy based techniques. *Analytical and bioanalytical chemistry*, 405(5):1463–1478, 2013.

[120] Dong Wang and Thomas P Russell. Advances in atomic force microscopy for probing polymer structure and properties. *Macromolecules*, 51(1):3–24, 2018.

[121] Jonathan T Pham, Frank Schellenberger, Michael Kappl, and Hans-Jürgen Butt. From elasticity to capillarity in soft materials indentation. *Physical Review Materials*, 1(1):015602, 2017.

[122] Emilios K Dimitriadis, Ferenc Horkay, Julia Maresca, Bechara Kachar, and Richard S Chadwick. Determination of elastic moduli of thin layers of soft material using the atomic force microscope. *Biophysical journal*, 82(5):2798–2810, 2002.

[123] Fedrico Gramazio. *Determination of nanomechanical properties of surfaces by atomic force microscopy using higher harmonics*. PhD thesis, Universitat Autonoma de Barcelona, 2018.

[124] Kenneth R. Shull. Contact mechanics and the adhesion of soft solids. *Materials Science and Engineering: R: Reports*, 36(1):1–45, 2002.

[125] Etienne Barthel and Antoine Perriot. Adhesive contact to a coated elastic substrate. *Journal of Physics D: applied physics*, 40(4):1059, 2007.

[126] Yeh-Shiu Chu, Sylvie Dufour, Jean Paul Thiery, Eric Perez, and Frederic Pincet. Johnson-kendall-roberts theory applied to living cells. *Physical review letters*, 94(2):028102, 2005.

[127] Richard Villey, Emmanuelle Martinot, Cécile Cottin-Bizonne, Magali Phaner-Goutorbe, Liliane Léger, Frédéric Restagno, and Elisabeth Charlaix. Effect of surface elasticity on the rheology of nanometric liquids. *Physical review letters*, 111(21):215701, 2013.

[128] Dongshi Guan, Chloe Barraud, Elisabeth Charlaix, and Penger Tong. Noncontact viscoelastic measurement of polymer thin films in a liquid medium using long-needle atomic force microscopy. *Langmuir*, 33(6):1385–1390, 2017.

[129] Dongshi Guan, Elisabeth Charlaix, Robert Z Qi, and Penger Tong. Noncontact viscoelastic imaging of living cells using a long-needle atomic force microscope with dual-frequency modulation. *Physical Review Applied*, 8(4):044010, 2017.

[130] M Lantz, YZ Liu, XD Cui, H Tokumoto, and SM Lindsay. Dynamic force microscopy in fluid. *Surface and Interface Analysis*, 27(5-6):354–360, 1999.

[131] Cédric Jai, Touria Cohen-Bouhacina, and Abdelhamid Maali. Analytical description of the motion of an acoustic-driven atomic force microscope cantilever in liquid. *Applied Physics Letters*, 90(4):113512, 2007.

[132] Abdelhamid Maali and Rodolphe Boisgard. Precise damping and stiffness extraction in acoustic driven cantilever in liquid. *Journal of Applied Physics*, 114(14):144302, 2013.

[133] Daniel Kiracofe and Arvind Raman. Quantitative force and dissipation measurements in liquids using piezo-excited atomic force microscopy: a unifying theory. *Nanotechnology*, 22(48):485502, 2011.

[134] Xin Xu and Arvind Raman. Comparative dynamics of magnetically, acoustically, and brownian motion driven microcantilevers in liquids. *Journal of Applied Physics*, 102(3):034303, 2007.

[135] K. L. Johnson. *Contact Mechanics*. Cambridge University Press, 1985.

[136] Leslie M Hocking. The effect of slip on the motion of a sphere close to a wall and of two adjacent spheres. *Journal of Engineering Mathematics*, 7(3):207–221, 1973.

[137] Gregory B McKenna and Richard J Gaylord. Relaxation of crosslinked networks: theoretical models and apparent power law behaviour. *Polymer*, 29(11):2027–2032, 1988.

[138] Stefan Karpitschka, S Das, Mathijs van Gorcum, Hugo Perrin, Bruno Andreotti, and Jacco H Snoeijer. Droplets move over viscoelastic substrates by surfing a ridge. *Nature communications*, 6(1):1–7, 2015.

[139] James C Scanlan and H Henning Winter. Composition dependence of the viscoelasticity of end-linked poly (dimethylsiloxane) at the gel point. *Macromolecules*, 24(1):47–54, 1991.

[140] Prerak Gupta, Gautham Hari Narayana SN, Uvanesh Kasiviswanathan, Tarun Agarwal, K Senthilguru, Devdeep Mukhopadhyay, Kunal Pal, Supratim Giri, Tapas K Maiti, and Indranil Banerjee. Substrate stiffness does affect the fate of human keratinocytes. *RSC advances*, 6(5):3539–3551, 2016.

[141] EM Darling. Force scanning: a rapid, high-resolution approach for spatial mechanical property mapping. *Nanotechnology*, 22(17):175707, 2011.

[142] Nicholas E Kurland, Zouheir Drira, and Vamsi K Yadavalli. Measurement of nanomechanical properties of biomolecules using atomic force microscopy. *Micron*, 43(2-3):116–128, 2012.

[143] Hans-Jürgen Butt, Jonathan T Pham, and Michael Kappl. Forces between a stiff and a soft surface. *Current Opinion in Colloid & Interface Science*, 27:82–90, 2017.

[144] Anastasia Papadopoulou, Jurriaan J Gillissen, Helen J Wilson, Manish K Tiwari, and Stavroula Balabani. On the shear thinning of non-brownian suspensions: Friction or adhesion? *Journal of Non-Newtonian Fluid Mechanics*, 281:104298, 2020.

[145] Phong Pham, Bloen Metzger, and Jason E. Butler. Particle dispersion in sheared suspensions: Crucial role of solid-solid contacts. *Physics of Fluids*, 27(5):051701, 2015.

[146] F. Gadala-Maria and A. Acrivos. Shear-induced structure in a concentrated suspension of solid spheres. *Journal of Rheology*, 24:799–814, 1980.

[147] Frédéric Blanc, François Peters, and Elisabeth Lemaire. Experimental signature of the pair trajectories of rough spheres in the shear-induced microstructure in noncolloidal suspensions. *Physical Review Letter*, 107:208302, 2011.

[148] R. V. More and A. M. Ardekani. Roughness induced shear thickening in frictional non-brownian suspensions: A numerical study. *Journal of Rheology*, 64(2):283–297, 2020.

[149] Sümer M. Peker, Şerife Ş. Helvacı, H. Banu Yener, Berrin İkizler, and Alp Alparslan, editors. *Solid-Liquid Two Phase Flow.* Elsevier, Amsterdam, 2008.

[150] B. M. Guy, M. Hermes, and W. C. K. Poon. Towards a unified description of the rheology of hard-particle suspensions. *Phys. Rev. Lett.*, 115:088304, Aug 2015.

[151] Cécile Clavaud, Antoine Bérut, Bloen Metzger, and Yoël Forterre. Revealing the frictional transition in shear-thickening suspensions. *Proceedings of the National Academy of Sciences*, 114(20):5147–5152, 2017.

[152] Chiao-Peng Hsu, Shivaprakash N. Ramakrishna, Michele Zanini, Nicholas D. Spencer, and Lucio Isa. Roughness-dependent tribology effects on discontinuous shear thickening. *Proceedings of the National Academy of Sciences*, 115(20):5117–5122, 2018.

[153] Andreas Acrivos, Xiaoxing Fan, and Roberto Mauri. On the measurement of the relative viscosity of suspensions. *Journal of Rheology*, 38(5):1285–1296, 1994.

[154] Roger Tanner, Christopher Ness, Arif Mahmud, Shaocong Dai, and Jiyoung Moon. A bootstrap mechanism for non-colloidal suspension viscosity. *Rheologica Acta*, 57, 10 2018.

[155] J A Greenwood and D Tabor. The friction of hard sliders on lubricated rubber: The importance of deformation losses. *Proceedings of the Physical Society*, 71(6):989–1001, jun 1958.

[156] K. L.. Johnson. *Contact Mechanics*. Cambridge University Press; New York, 1985.

[157] R. D. Mindlin. Compliance of elastic bodies in contact. *J. Appl. Mech.*, 16:259–268, 1949.

[158] R.D. Mindlin and H. Deresiewicz. Elastic spheres in contact under varying oblique force. *J. Appl. Mech.*, 20:327–344, 1953.

[159] R v Mises. Mechanik der festen körper im plastisch-deformablen zustand. *Nachrichten von der Gesellschaft der Wissenschaften zu Göttingen, Mathematisch-Physikalische Klasse*, 1913:582–592, 1913.

[160] Anthony C Fischer-Cripps. Factors affecting nanoindentation test data. *Introduction to contact mechanics*, pages 61–82, 2000.

[161] AC Fischer-Cripps. Predicting hertzian fracture. *Journal of materials science*, 32(5):1277–1285, 1997.

[162] Peter A Cundall and Otto DL Strack. A discrete numerical model for granular assemblies. *geotechnique*, 29(1):47–65, 1979.

[163] J Shafer, S Dippel, and DE Wolf. Force schemes in simulations of granular materials. *Journal de physique I*, 6(1):5–20, 1996.

[164] David Schrader. Physical constants of poly (styrene). *The Wiley Database of Polymer Properties*, 2003.

[165] Nicolas Fernandez, Juliette Cayer-Barrioz, Lucio Isa, and Nicholas D Spencer. Direct, robust technique for the measurement of friction between microspheres. *Langmuir*, 31(32):8809–8817, 2015.

[166] Muhammad Arshad, Abdelhamid Maali, Cyrille Claudet, Laurent Lobry, François Peters, and Elisabeth Lemaire. An experimental study on the role of inter-particle friction in the shear-thinning behavior of non-brownian suspensions. *Soft Matter*, 2021.

[167] Stany Gallier, Elisabeth Lemaire, Laurent Lobry, and Francois Peters. Effect of confinement in wall-bounded non-colloidal suspensions. *Journal of Fluid Mechanics*, 799:100–127, 2016.

[168] Andrea W Chow, Steven W Sinton, Joseph H Iwamiya, and Thomas S Stephens. Shear-induced particle migration in couette and parallel-plate viscometers: Nmr imaging and stress measurements. *Physics of Fluids*, 6(8):2561–2576, 1994.

[169] Kenneth Langstreth Johnson, Kevin Kendall, and aAD Roberts. Surface energy and the contact of elastic solids. *Proceedings of the royal society of London. A. mathematical and physical sciences*, 324(1558):301–313, 1971.